Astronomy Reports, Vol. 47, No. 4, 2003, pp. 263–275. Translated from Astronomicheskiĭ Zhurnal, Vol. 80, No. 4, 2003, pp. 291–303.

The Subsystem of Open Clusters in the Post-Hipparcos Era: Cluster Structural Parameters and Proper Motions

N. V. Kharchenko[1], L. K. Pakulyak[1], and A. E. Piskunov[2]

[1] *Main Astronomical Observatory, ul. Akademika Zabolotnogo 27, Kiev, 03680 Ukraine*

[2] *Institute of Astronomy, Russian Academy of Sciences, ul. Pyatnitskaya 48, Moscow, 109017 Russia*

Received August 23, 2002; in final form, October 10, 2002

Abstract—The wide neighborhoods of 401 open clusters are analyzed using the modern, high-precision, homogeneous ASCC-2.5 all-sky catalog. More than 28 000 possible cluster members (including about 12 500 most probable members) are identified using kinematic and photometric criteria. Star counts with the ASCC-2.5 and USNO-A2.0 catalogs are used to determine the angular and linear radii of the cluster cores and coronas, which exceed the previously published values by factors of two to three. The segregation (differing central concentration) of member stars by magnitude is observed. The mean proper motions are determined directly in the Hipparcos system for 401 clusters, for 183 of them for the first time. The heliocentric distances of 118 clusters are determined for the first time based on color–magnitude diagrams for their identified members. © *2003 MAIK "Nauka/Interperiodica"*.

1. INTRODUCTION

Open star clusters are typical Galactic disk-population objects. At the same time, the spatial coordinates, velocities, and ages of open clusters can be determined much more accurately than for other Population-I objects. The reason is that, usually, up to several hundred stars can be observed in each cluster, and the spatial–kinematic parameters of all the cluster stars are either virtually identical or obey certain relations (spectroscopic and photometric data). This makes it possible to select cluster members among all stars seen in the direction of a cluster, making these objects an especially valuable tool for analyzing the structure and evolution of stellar systems such as individual clusters or the Galactic disk as a whole.

The principal drawback of clusters as objects for such studies is the inhomogeneity, insufficient accuracy, and incompleteness of stellar data. This is due to the fact that the available stellar data—proper motions and photometric parameters being the most abundant among them—have been obtained in cluster neighborhoods by various authors using different instruments and different instrumental systems with different degrees of completeness and accuracy. Furthermore, the apparent surface distribution of cluster members can be distorted by interstellar clouds along the line of sight and/or inside young open clusters. All this makes the correct identification of cluster member stars rather difficult, distorting the principal parameters of the cluster: its spatial structure, space velocity, color–magnitude diagram, stellar content, and age.

The last decade has witnessed sweeping qualitative and quantitative developments in the creation of all-sky catalogs of positional, kinematic, and photometric stellar data. The results of the Hipparcos space mission formed the basis for several catalogs (Hipparcos, Tycho-1 [1], and Tycho-2 [2]), which contain high-precision stellar data and establish an inertial reference frame and two-color photometric system over the entire sky. Many ground-based catalogs have already been reduced to these systems, including the currently most massive and deepest catalog, containing more than 500 million stars down to a limiting magnitude of $B \simeq 22^m$—the USNO-A2.0 catalog [3] (hereafter, the USNO catalog). Recently, Kharchenko [4] combined all the data from modern, high-precision, astrometric catalogs containing stars down to $V = 12 - 14^m$ into the "All-Sky Combined Catalog of Astrometric Data for 2.5 Million Stars" (hereafter, the ASCC).

About 1500 open clusters have been discovered in the Galaxy so far; however, only after the Hipparcos mission had been successfully completed and its results implemented in practice did it become possible to create catalogs of open-cluster parameters determined in systems that are uniform over the entire sky in terms of the observational material and/or methods used.

The most complete source of geometrical and astrophysical parameters of open clusters is the Lund Catalog of Open Cluster data (LCOC), compiled by

1063-7729/03/4704-0263$24.00

Lyngå [5] and containing a total of 1150 objects. These data are the result of compiling an extensive bibliography and contain, among other things, the distances and ages of 420 open clusters. The distances, color excesses, and ages of 340 open clusters, recently expanded to include a total of 425 open clusters, can be found in [6–8].

The study of the nearest clusters was among the primary tasks of the Hipparcos [1] mission. Robichon *et al.* [10], Baumgardt *et al.* [11], and Loktin and Beshenov [12] determined the trigonometric parallaxes of 50, 205, and 45 open clusters based on preselected lists of 550, 715, and 638 members, respectively. Robichon *et al.* [10] and Baumgardt *et al.* [11] obtained the proper motions of the open clusters in the Hipparcos reference frame. Dias *et al.* [13, 14] determined these parameters for 205 clusters using data for about 5900 Tycho-2 [2] stars identified as cluster members using the Sanders statistical method. As a result, open-cluster proper motions were first determined directly in an inertial reference frame. Glushkova *et al.* [15] determined the proper motions of 331 open clusters using 2980 photometrically identified cluster members selected from the "Catalog of About Four Million Stars" [16] created at the Sternberg Astronomical Institute and then reduced the resulting proper motions to the Hipparcos reference frame. In all these studies, the authors have adopted previously published structural parameters for the open clusters (the central coordinates and sizes) without redetermining them.

The size of a cluster is one of its main parameters, which is related to the dynamical states of the cluster and the Galactic disk and plays a key role in determining whether particular stars belong to the cluster or not. Often, however, only the size of the central region of the cluster has been considered, although many studies (see Kholopov's [17] monograph for references) have found that clusters possess extended coronas whose identification is made difficult by superposed rich stellar fields. It is the size of the core—even if the cluster was known to possess a corona—that Lyngå tended to include in the LCOC, and many authors mistook these sizes for those of the entire clusters. Researchers have rarely redetermined cluster sizes, and very few of them have done this on a massive scale using a homogeneous technique. Danilov and Seleznev [18] (hereafter DS) created the most homogeneous catalog of structural characteristics of 103 Northern clusters based on star counts down to $B \simeq 16^m$ performed on wide-angle plates obtained with a single instrument—the SBG camera of the Kourovka Observatory.

Our aim is to determine the structural and kinematic parameters of all open clusters whose members can be found in large modern catalogs of high-precision stellar data obtained in all-sky, homogeneous, astrometric and photometric systems, having in view the subsequent use of these parameters for analyzing individual open clusters and the Galactic disk as a system of such clusters. We address some of these tasks in this paper. Section 2 describes the sources of the observational data, and Section 3, the open-cluster sample used and the technique employed. Section 4 summarizes the underlying principles of identifying probable cluster members based on proper-motion data and BV spaceborne photometry and the results of applying these principles. Section 5 analyzes the structural parameters of the open clusters obtained, and Section 6, specific features of the distributions of stars of various masses inside these open clusters. Section 7 reports the open-cluster proper motions in the Hipparcos frame determined in this paper.

2. CATALOGS OF STELLAR DATA

Our principal tools for determining the parameters of the open clusters were the ASCC and USNO star catalogs.

The ASCC, which is based on large, modern, high-precision catalogs and covers the magnitude interval $V = 12 - 14^m$, is most complete in terms of its list of stars and the composition of the stellar data reduced to homogeneous, all-sky, standard systems. The input data for the ASCC include both catalogs based directly on data from the Hipparcos and Tycho [1] projects (the files hip_main.dat and h_dm_com.dat, with multiple-star components, and tyc_main.dat), and catalogs based on earlier data from the Astrographic Catalog: ACT RC [19], TRC [20], and Tycho-2 [2]. The list of Hipparcos stars is incomplete, especially in crowded fields, where some of the clusters are located. The same drawback is also characteristic of catalogs based on much more complete observations performed in the Tycho project, due to the specifics of the TUC 1/2 input star lists, which were based primarily on the Guide Star Catalog [21]. Therefore, an appreciable fraction of stars in such areas of the sky is provided by the ground-based CMC11 [22] and PPM [23–25] catalogs, which we also used in compiling the ASCC.

The ASCC includes 2 501 968 stars with J2000 equatorial coordinates for the observing epoch of 1991.25 and compiled proper motions in the Hipparcos system. The trigonometric parallaxes are computed as weighted averages over the catalogs [1]. With few exceptions, the magnitudes are adopted from the Tycho catalogs and reduced to the Johnson B,V system using a photometric reference system defined by 20 000 stars never suspected to be variable. The final catalog gives the standard errors for all these

quantities. The MK and/or HD spectral types; multiplicity and variability flags; and the Hipparcos, HD, and DM numbers were taken from the corresponding source catalogs. Its completeness and the accuracy of its data makes the ASCC a unique tool for selecting cluster members and analyzing star clusters.

The USNO catalog is currently the deepest all-sky catalog, containing J2000 equatorial coordinates and magnitudes in systems close to the B and R bands for a total of 526.3 million stars down to a limiting magnitude of $B \simeq 22^m$. These data are based on Schmidt plate scans taken from 1950 to the 1980s at the Palomar and European Southern Observatories. The USNO positions were computed using the ACT RC [19] catalog, whose positions and proper motions are, in turn, tied to the Hipparcos system. The magnitudes of bright stars are tied to the Tycho-1 [1] data, while those of faint stars were calibrated using CCD observations. The use of the USNO catalog for analyzing star clusters is hindered by the fact that it contains no objects in the vicinity of bright stars and in crowded areas of the sky. However, for sufficiently compact open clusters, the USNO catalog can be used to determine the structural cluster parameters unbiased by detector-size limitations.

In addition, we made extensive use of the "Millennium Star Atlas" [26], which contains more than one million stars of the Tycho-1 catalog [1] and gives some idea about how clusters appear against field stars and about the appearance of specific features due to the presence and distribution of neighboring clusters, field stars, interstellar gas, and dusty material.

3. LIST OF OPEN CLUSTERS AND TECHNIQUE EMPLOYED

We compiled a preliminary list of about 500 open clusters by identifying all the LCOC clusters in the ASCC and the "Millennium Star Atlas" [26], provided that at least ten ASCC stars were located within an area of sky with a diameter three times the value given in the LCOC. We did not consider the Hyades and similar open clusters, which span very large areas, in order to preserve the homogeneity of the methods used to determine the cluster parameters. We discarded some clusters in the process of our work, and our final list contains a total of 401 open clusters, each represented in the ASCC by at least five probable members.

We used a multifaceted approach to determine and/or refine the structural and kinematic parameters of the open clusters—the central equatorial coordinates $(\alpha, \delta)_{\mathrm{J2000}}$, radii r_1 of the core and r_2 of the corona (which corresponds to the radius of the entire cluster), proper-motion components ($\mu_x \equiv \mu_\alpha \cos\delta$ and $\mu_y \equiv \mu_\delta$), list of cluster members, distance d, and color excess $E(B-V)$. We carried out several iterations for each cluster and in each performed a joint analysis of the corresponding sky chart, vector diagram of the proper motions, magnitude dependence of the proper-motion components, V vs. $(B-V)$ color–magnitude diagrams, the location of the zero-age main sequence (ZAMS) in the color–magnitude diagram, and the radial distribution $F(r)$ of the stellar density.

As a zeroth approximation, we used the area with the LCOC coordinates and a diameter equal to three times the LCOC value (but not greater than 1°). We then searched this area for cluster members using the technique described in Section 4. We adopted the point of maximum surface density of cluster members as the cluster center, which we subsequently used to compute the function $F(r)$ to determine the radius of the region of sky onto which the members are projected. We then used the resulting spatial parameters as input data for the next approximation. As a rule, two approximations were sufficient to identify the cluster members and determine the structural and kinematic parameters; however, some clusters with sparse structure or erroneous initial central coordinates required three and more approximations.

As a rule, the differences between the refined open-cluster coordinates and those listed in [5] are small and can be explained by the consideration of different distributions of stars with different magnitudes. These discrepancies exceed 0.°3 for only ten clusters, due to errors in the open-cluster coordinates in the old catalogs or to problems with identifying the centers of large open clusters, such as Mel 20 (α Per), Mel 111 (Coma), and NGC 2632 (Praesepe).

We adopted the functional form of the ZAMS specified by Schmidt-Kaler [27] and determined its position on the color–magnitude diagram based on the distance d, color excess $E(B-V)$, and extinction $A_V = 3.1\,E(B-V)$. We adopted the d and $E(B-V)$ values for 231, 17, 22, and 13 open clusters from Loktin *et al.* [7, 8], with allowance for the corrections therein; Robichon *et al.* [10]; the LCOC; and the WEBDA open cluster database [28], in order of decreasing priority. For some clusters, primarily those with variable extinction, we corrected the $E(B-V)$ values in accordance with the shape of the color–magnitude diagram. For 118 clusters with unknown d and $E(B-V)$ values, we determined these parameters by ZAMS fitting, taking into account the appearance of the cluster color–magnitude diagram and the absolute magnitudes of stars with known spectral types.

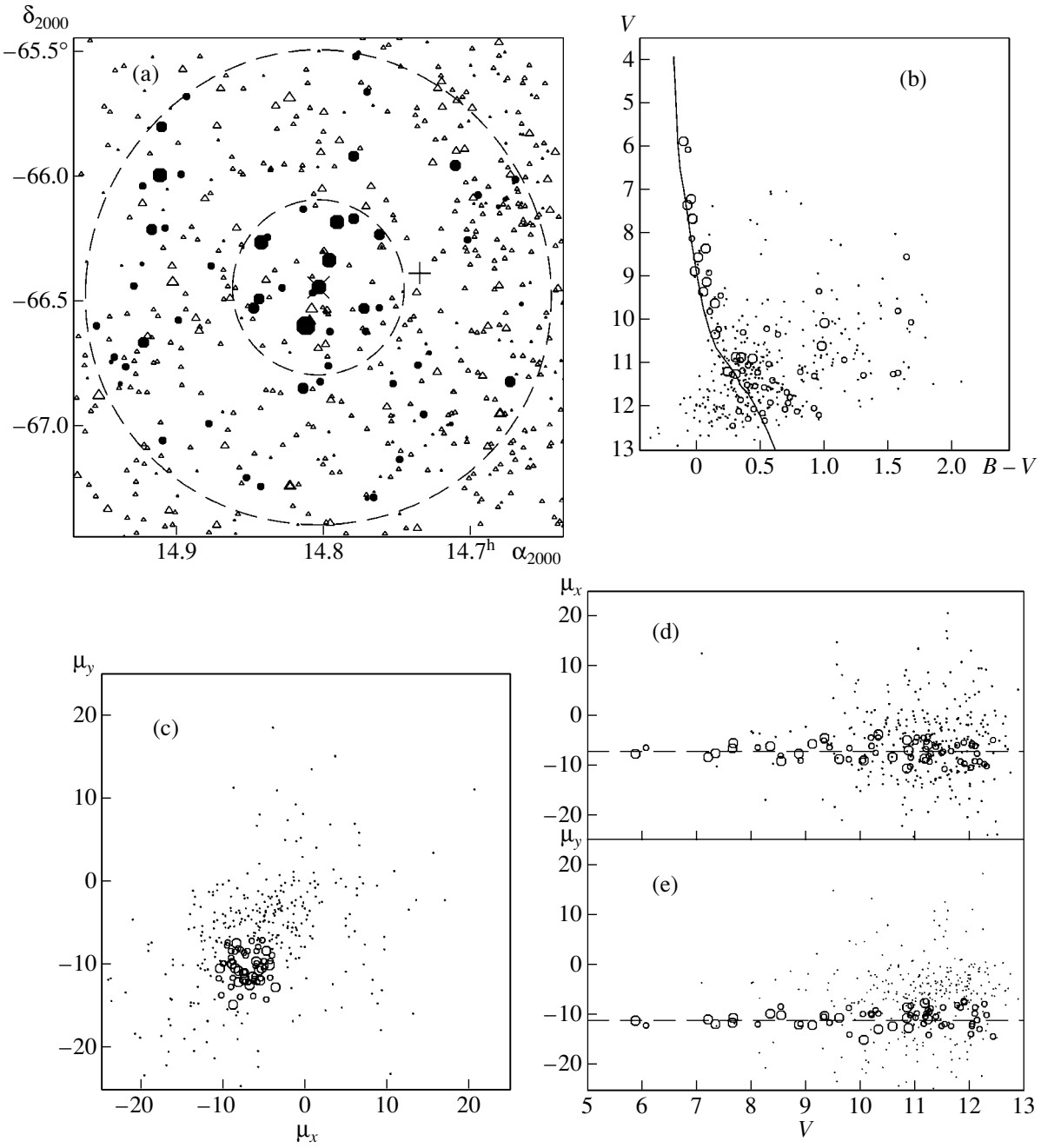

Fig. 1. The cluster C1439-661 (vdB-Hagen 164) according to the ASCC data. The circles on the equatorial-coordinates map (a) show the most probable cluster members and the triangles all remaining stars. The size of each symbol corresponds to the magnitude of the corresponding star. The pluses and crosses indicate the positions of the cluster center according to the LCOC and our analysis, respectively. The dashed circles with radii of 0.°35 and 0.°95 bound the core and corona regions, respectively. The large and small circles in plots (b)–(e) indicate probable cluster members located in the core and corona, respectively, while the points show all remaining stars. The proper motions are in units of 0.001″/yr. The position of the ZAMS on the color–magnitude diagram (b) corresponds to $d = 541$ pc and $E(B-V) = 0^m.15$. The dashed lines in (d) and (e) indicate the average motion of the cluster: $(\mu_x, \mu_y) = (-7.1 \pm 0.4, -10.9 \pm 0.4) \times 0.001''$/yr.

Figure 1 shows the result of our iterative procedure for identifying the members of the cluster C1439-661 (vdB-Hagen 164) and determining its previously unknown distance and $E(B-V)$.

4. IDENTIFICATION OF CLUSTER MEMBERS

Unbiased determinations of cluster parameters are possible only if the cluster members are correctly

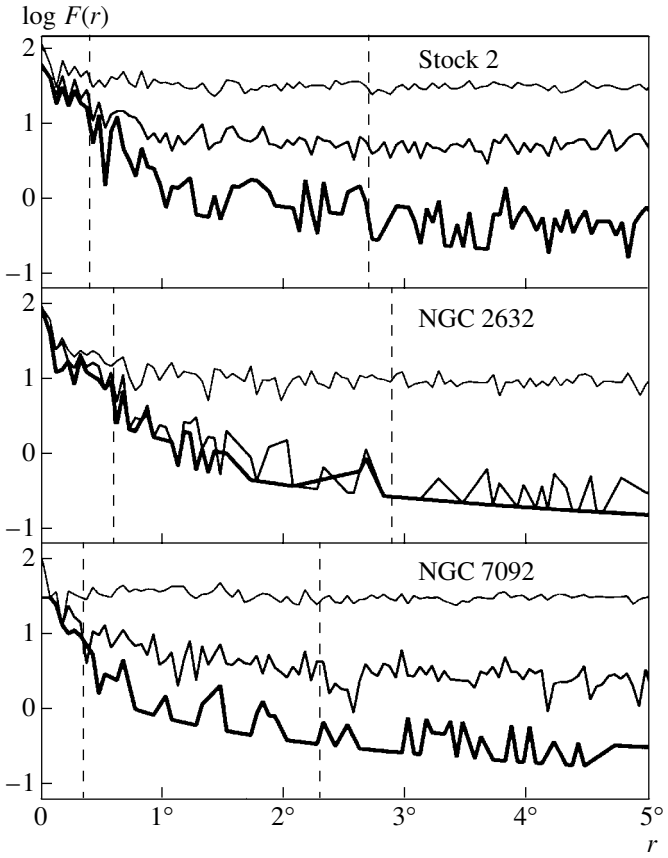

Fig. 2. Distribution of the surface density $F(r)$ of ASCC stars with $V \leq 11^m.5$ as a function of the angular distance from the cluster center in areas of sky with three selected open clusters. The vertical axis has a logarithmic scale and $F(r)$ is in units of square degree. The thin, medium, and bold lines show $F(r)$ computed for all stars, possible cluster members ($P \geq 1\%$), and most probable cluster members ($P \geq 61\%$), respectively. The dashed lines show the radii of the cluster cores (r_1) and coronas (r_2).

identified. The most objective methods for identifying members are based on kinematic parameters, first and foremost, proper motions. However, because the proper motions of clusters and of the disk stars against which the open clusters are observed are usually comparable to each other and to their standard errors, we used photometric data as a supplementary criterion.

We used the following iterative procedure to identify cluster members in each of the approximations described above. For all stars located within a circular region of a given radius, we computed the probability P of cluster membership for the ith star:

$$P^i = C^i \times \exp\left\{ -\frac{0.5}{2}\left[\left(\frac{\mu_x^i - \overline{\mu}_x}{\varepsilon_{\mu_x}^i} \right)^2 + \left(\frac{\mu_y^i - \overline{\mu}_y}{\varepsilon_{\mu_y}^i} \right)^2 \right] \right\} \times 100\%, \quad (1)$$

where $\mu_{x,y}^i$ and $\varepsilon_{\mu_{x,y}}^i$ are the components of the proper motion of the ith star and their standard errors (1σ) and $\overline{\mu}_{x,y}$ are the components of the mean proper motion of the cluster. The factor C^i is equal to 1 or 0 depending on whether the star satisfies the photometric criterion for cluster membership. We adopted

Table 1. Statistical data for ASCC stars projected onto 401 clusters

Sample	Cluster areas		
	$0 \ldots r_1$	$r_1 \ldots r_2$	$0 \ldots r_2$
All stars	9497	53372	62869
$P \geq 61\%$	4513	7910	12423
$14\% \leq P < 61\%$	1861	8464	10325
$1\% \leq P < 14\%$	586	4775	5361
$P < 1\%$	6960	21149	28109

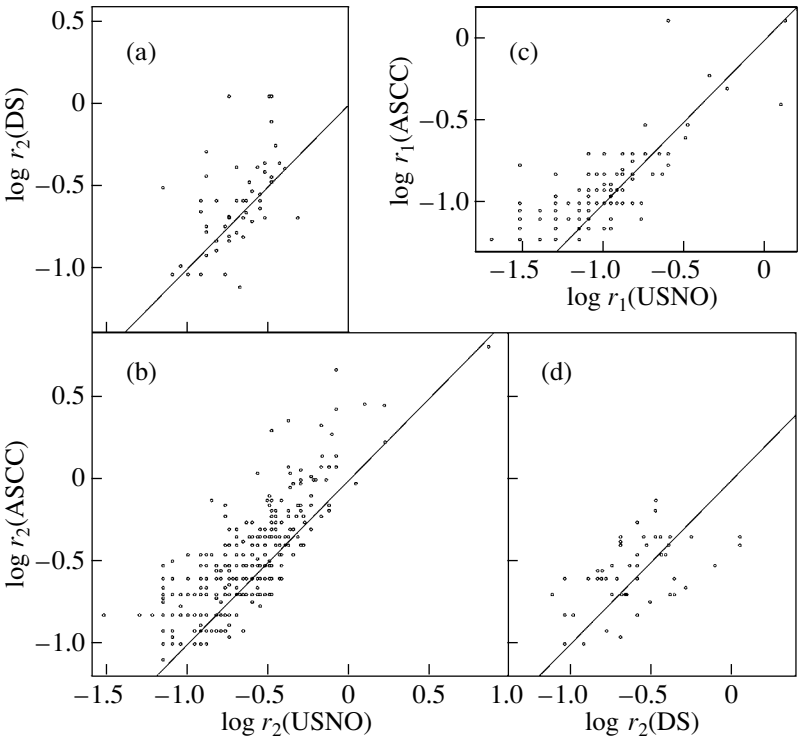

Fig. 3. Comparison of angular radii of open-cluster coronas r_2 (a–c) and cores r_1 (d) determined from star counts using the ASCC, USNO catalog, and DS. The scales are logarithmic and radii are in degrees. The straight lines correspond to loci of equal radii.

$C^i = 1$ if the star's position in the color–magnitude diagram is no more than 1σ of the color index $\varepsilon^i_{(B-V)}$ to the left of the ZAMS.

Stars with $C^i = 1$ and proper motions deviating from the cluster proper motion by less than one, two, or three σ have cluster membership probabilities greater than 61%, 14%, and 1%, and we therefore considered them to be most probable, probable, and possible cluster members, respectively. We computed the components $\overline{\mu}_{x,y}$ based on stars with $P \geq 61\%$ within the core, then computed refined probabilities in accordance with (1). We stopped this iterative procedure when two consecutive steps yielded identical lists of cluster members.

Table 1 lists the total numbers of ASCC stars projected onto the core and corona regions of 401 clusters, bounded by circles with radii r_1 and r_2. We identified a total of 12 500 most probable members with $P \geq 61\%$, which, on average, corresponds to 31 stars per cluster. Robichon *et al.* [10] and Baumgardt *et al.* [11] identified 11 and 3.5 stars per cluster, respectively. However, they used the obviously incomplete Hipparcos [1] catalog. Dias *et al.* [13, 14] considered, on average, 28.7 Tycho-2 [2] stars per cluster with membership probabilities greater than 51%; this corresponds to 25 such stars for the criterion $P \geq 61\%$. Glushkova *et al.* [15] identified, on average, nine stars from catalog [16] per cluster. Thus, our multifaceted approach has enabled us to most completely identify open-cluster members using available high-precision stellar data.

We did not apply the identification procedure to the USNO stars, due to the lack of proper motions, uncertainty of the photometric system, and the large errors of the R magnitudes, whose systematic errors were 1^m and standard errors were $0^m.5$, strongly distorting the B vs. $(B - R)$ color–magnitude diagram.

5. STRUCTURAL PARAMETERS OF THE CLUSTERS

The measured size of a cluster depends on many factors: the method and quality of member identification, the limiting magnitude and density of the data used, and the presence and distribution of absorbing matter.

We determined the structural parameters of the open clusters from star counts using the ASCC and USNO catalog, assuming that the distribution of the cluster members is centrally symmetric and consists of two components with radii r_1 and r_2—the core and corona. These radii correspond to the cluster-centric distances where the absolute value of the stellar surface density gradient decreases abruptly (r_1)

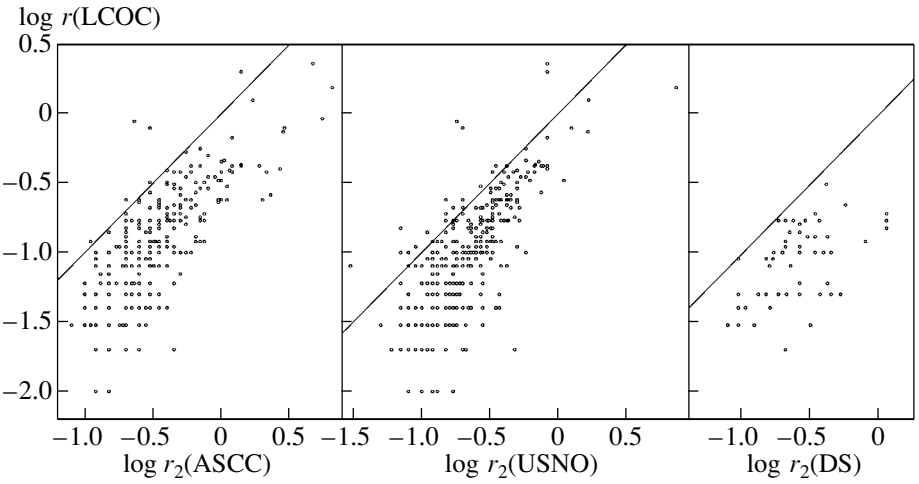

Fig. 4. Comparison of the corona angular radii r_2 determined from star counts using the ASCC, USNO catalog, and DS with the values given by Lyngå [5] in the LCOC. The scales are logarithmic and the radii are in degrees. The straight lines show loci of equal radii.

and ceases to change (r_2). Our method is less formal than determining the structural parameters in the context of a specific model (e.g., a King model [29]); however, it can be applied to poorer clusters, thereby considerably expanding the sample studied. This is why we preferred this method for our analysis.

We constructed the functions $F(r)$ corresponding to the radial density distributions of stars brighter than $V = 11\overset{m}{.}5$, where the catalog reaches its completeness limit, out to angular distances from the cluster center of 10° in annular zones with steps of $0\overset{\circ}{.}05$. We used three stellar samples: (i) all stars, and cluster members with probabilities (ii) $P \geq 1\%$ and (iii) $P \geq 61\%$. Figure 2 illustrates the degree of variation of $F(r)$ with radial distance for various groups of stars using three clusters (Stock 2, NGC 2632 (Praesepe), and NGC 7092) as examples.

In addition to the ASCC, we used the USNO catalog when possible. We determined the structural parameters of the selected open clusters based on the USNO catalog data, using the central coordinates and corona sizes determined from the ASCC data. To this end, we selected from the USNO catalog all stars within a radius $\rho = 3r_2^{\mathrm{ASCC}}$. The USNO catalog cannot be used to determine the sizes of some nearby open clusters with large angular diameters and low surface densities for their member stars, which do not substantially exceed the overall stellar density in a crowded field. Certain problems also arise in regions with high stellar surface densities located in the vicinity of bright stars and nebulae where there are no stars in the USNO catalog and in some areas where the limiting magnitude of the USNO catalog is several magnitudes brighter than the average value for the catalog.

We tried to overcome these problems in two ways. First, in the region of each cluster, we computed $F(r)$ for stars brighter than the limiting completeness magnitude B_c of the catalog, which we determined by analyzing the integrated magnitude function $N(B)$. For clusters with dense cores, we estimated the sizes of the possible drop in the surface distribution of stars and analyzed the surface distribution taking into account the presence or absence of such a drop. Second, we constructed $F(r)$ both for the entire ring and separately for the four quadrants. This enabled us to take into account possible errors in the coordinates of the cluster center or asymmetry of the stellar distribution due to the origins above. We determined the corona sizes for 363 and the core radii for 140 open clusters by carrying out a joint analysis of all five $F(r)$ functions, which we computed over the distance interval $r \leq \rho$ in annular zones with steps of $0\overset{\prime}{.}5$.

Figure 3 compares the angular radii of cluster cores and coronas determined directly from star counts in this paper and by DS. It is clear that the radii of small cores ($r_1^{\mathrm{ASCC}} < 0\overset{\circ}{.}1$) are overestimated due to the insufficient angular resolution of the star

Table 2. Characteristic linear radii (in pc) of the cluster cores and coronas in the Galaxy

Source	$R_1^{\min}$	$R_2^{\min}$	$R_1^{\max}$	$R_2^{\max}$	$\overline{R}_1$	$\overline{R}_2$
ACSS	0.6	1.5	7.1	19.2	1.7	5.0
USNO	0.5	0.9	4.8	15.9	1.5	3.5
DS	0.5	3.0	4.5	17.2	2.7	7.6
LCOC	0.2	–	10.0	–	2.0	–

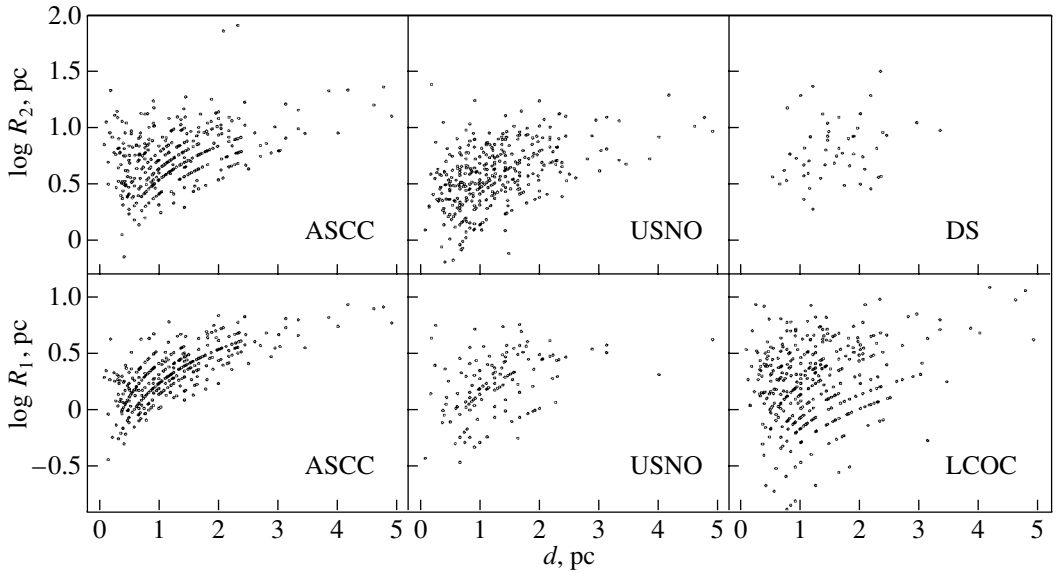

Fig. 5. Linear sizes of the cluster cores (R_1) and coronas (R_2) determined from star counts using the ASCC, USNO catalog, and DS and adopted from the LCOC as a function of the distances d of the clusters.

counts using the ASCC. The corona sizes $r_2^{\rm ASCC}$ are larger than those determined from the USNO data ($r_2^{\rm ASCC} = (1.4 \pm 0.1) \times r_2^{\rm USNO}$) throughout the entire radius interval, despite the significantly deeper limiting magnitude of the USNO star counts. The excess over the results of DS is not statistically significant, $r_2^{\rm ASCC} = (1.1 \pm 0.1) \times r_2^{\rm DS}$, and is due to the fact that identification of cluster members is not carried out in either the USNO catalog or DS, and the outer regions of the clusters were lost against the rich surrounding stellar fields. Figure 2, which shows the $F(r)$ curves based on the ASCC data computed for all stars, stars with $P \geq 1\%$, and stars with $P \geq 61\%$, demonstrates how the degree of selection affects the form of $F(r)$ and thereby the cluster sizes. Thus, the selection of cluster members in the ASCC enabled us to derive the most reliable cluster sizes, which exceed those determined using the deepest catalogs but without selection of cluster members by several tens of percent.

Figure 4 compares our radii with the extensive compilation of cluster sizes given in the LCOC. For comparison, we also give data adopted from the homogeneous sample of DS. Figure 4 shows how biased (mostly underestimated) are the cluster sizes used by many authors, who adopt them from the LCOC and forget that Lyngå [5] himself aimed to include in his catalog only the sizes of the cluster cores.

These data are, on average, underestimated by factors of 3.0 ± 0.1, 2.2 ± 0.1, and 2.9 ± 0.2 compared to the sizes of the cluster coronas (and, consequently, the sizes of the clusters themselves) determined from star counts using the ASCC, USNO catalog, and DS, respectively. To prevent further selection effects, we used only those LCOC and DS clusters that are included in our list.

The fact that our cluster list overlaps that of DS and that there is a satisfactory agreement of results makes it possible to establish a relation between the "empirical" sizes inferred from star counts and the sizes obtained by DS by fitting the results of star counts to model King curves. We used the core radius r_c computed by DS using the King formula as $r_1^{\rm DS}$ (we transformed these values into angular units using distances taken from DS).

The relation between the sizes of the cluster coronas and cores is more or less the same whether they are determined using the ASCC or USNO catalog: $r_2^{\rm ASCC} = (2.4 \pm 0.2) \times r_1^{\rm ASCC}$ and $r_2^{\rm USNO} = (2.6 \pm 0.1) \times r_1^{\rm USNO}$. Because the King radius refers to the most central region of the cluster, whereas $r_2^{\rm DS}$ approximately corresponds to our definition of the cluster radius, the correlation between the data of DS has a different form: $r_2^{\rm DS} = (4.5 \pm 0.4) \times r_1^{\rm DS}$. A comparison of these relations yields a relation between the King parameter and the empirical core radius $r_1^{\rm DS} = (0.5 \pm 0.1) \times r_1^{\rm ASCC} = (0.6 \pm 0.1) \times r_1^{\rm USNO}$.

DS also computed the tidal radii r_t of open clusters, which we transformed into angular units in the same way as for $r_1^{\rm DS}$ and compared with the empirical cluster radii r_2. As expected, the tidal radii are upper limits for r_2 and, on average, exceed the latter by a factor of 1.5 ± 0.1, 2.1 ± 0.1, and 1.6 ± 0.1 for the ASCC, USNO catalog, and DS, respectively.

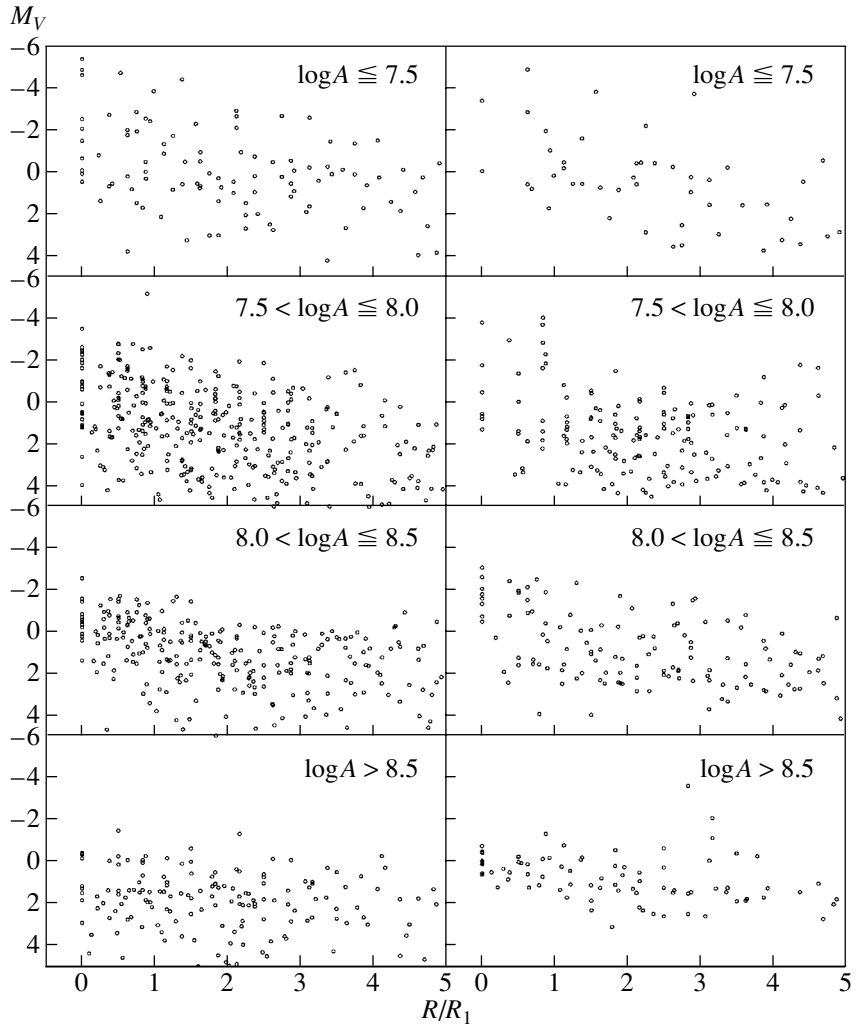

Fig. 6. Absolute magnitude M_V of the brightest cluster member ($P \geq 61\%$) within a ring of a given radius as a function of the relative radius R/R_1 for clusters in four age intervals. The left and right plots show stars that are still on the main sequence and those that have left it.

As pointed out above, distance estimates d are available for all the open clusters, enabling us to determine the linear radii of the cores (R_1) and coronas (R_2). Figure 5 shows the dependence of these radii on d. These distributions are characterized by strong selection effects near the lower boundary for the radii, due to the fact that, as the distance increases, small open clusters become increasingly inconspicuous against the background stellar field. This selection effect is evident for both R_1 and R_2. All the samples suffer from this effect, even the homogeneous DS sample, whose objects are located at characteristic distances $d = 1$–2 kpc.

The upper boundary of the distribution of linear radii is less subject to selection effects. The systematic effect in R_1^{ASCC} may be due to the overestimation of small values of r_1^{ASCC} discussed above, i.e., to problems in resolving the cores of distant clusters. For the USNO sample, on the contrary, it becomes systematically more difficult to identify nearby open clusters against the rich background stellar field. The trends in the upper boundaries of the linear radii with increasing d are much weaker for the other samples.

We computed the lower and upper boundaries $R^{\min}$ and $R^{\max}$ for the linear sizes of the structural components by averaging over the ten clusters with the smallest and largest radii in each sample (except h and χ Per, which have $R_2^{\mathrm{ASCC}} \approx 80$ pc; they correspond to the two uppermost points in the top left graph in Fig. 5). The mean linear radii $\overline{R}$ are determined from clusters located at distances smaller than 1 kpc, where selection effects are comparatively weak. These data are summarized in Table 2, and, although they suffer from various selection effects, they give some idea of the characteristic sizes of Galactic open clusters.

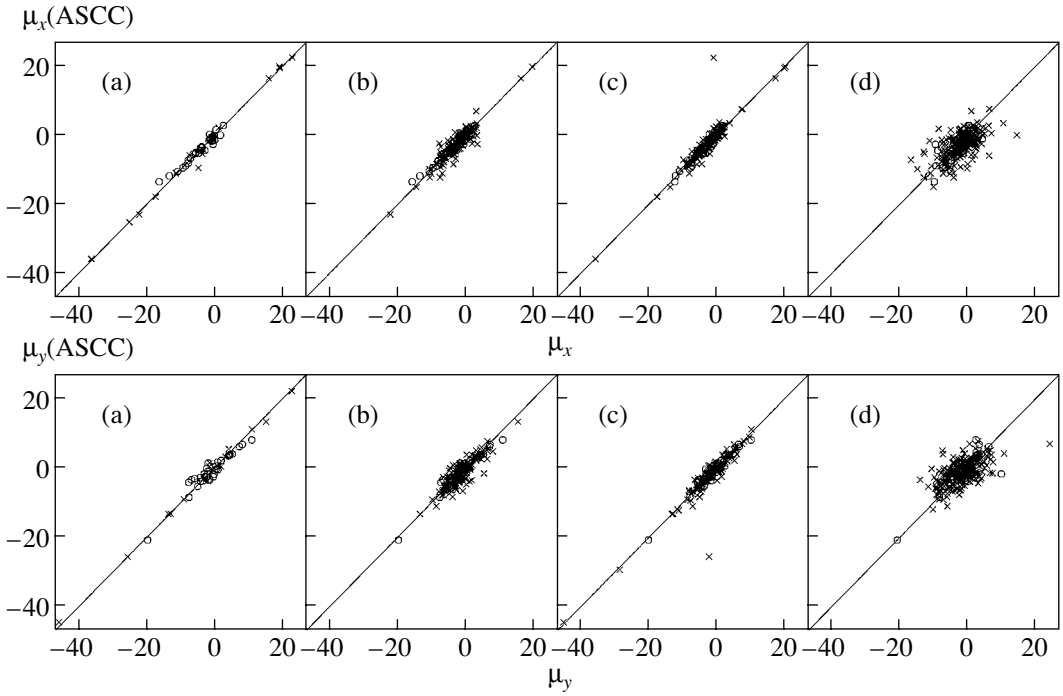

Fig. 7. Comparison of cluster proper motions (in $0.001''$/yr) derived here with those of (a) Robichon *et al.* [10], (b) Baumgardt *et al.* [11], (c) Dias *et al.* [13, 14], and (d) Glushkova *et al.* [15]. The straight lines are the loci of equal mu components in the two catalogs compared. The circles show the data for clusters included in all five catalogs.

6. SPATIAL SEGREGATION OF STARS IN CLUSTERS

Our data can be used to analyze differences between the spatial distributions of stars of different masses in clusters, i.e., the mass segregation, for which we have used the absolute magnitude M_V as an analog. We selected two of the brightest most probable cluster members ($P \geq 61\%$) in each annular zone around the cluster centers used to compute $F(r)$: one located in the main-sequence band in the color–magnitude diagram, which deviates to the left and right of the ZAMS by no more than $\varepsilon_{(B-V)}$ and $0\overset{m}{.}2 + \varepsilon_{(B-V)}$, and the second located to the right of this band, in the red part of the color–magnitude diagram corresponding to late evolutionary stages. We determined the absolute magnitudes M_V of these stars from their known V and d values. To ensure the homogeneity of the sample, we selected clusters with $d < 1$ kpc and mean ratios $\overline{R_2/R_1} \approx 4.5$ whose members span a magnitude interval of no less than 4^m. We subdivided the sample into four groups in age A $\log A \leq 7.5$, $7.5 < \log A \leq 8.0$, $8.0 < \log A \leq 8.5$, $\log A > 8.5$ consisting of 10, 27, 14, and 9 clusters, respectively.

Figure 6 shows the dependence of M_V for these brightest stars on the relative distance R/R_1 for a number of selected open clusters. The left-hand and right-hand graphs show the distributions of the main-sequence stars and of the stars that have left the main sequence. We can see that the area occupied by stars expands substantially with decreasing brightness: bright stars are observed exclusively in central cluster regions, whereas fainter, i.e., less massive, stars are distributed over the entire cluster volume. The observed distributions were constructed using many clusters with reliable and mutually independent data. This suggests that the observed trends are statistically significant. We eliminated the potential danger of systematic effects arising as a result of the mutual normalization of the cluster sizes by compiling a homogeneous sample of clusters and choosing the core radius R_1 as the normalizing coefficient, which is less subject to selection effects than R_2. The reality of the observed effect is also supported by the absence of segregation in the group of old clusters.

The data in Fig. 6 can also be interpreted in a different way: stars from the entire mass interval, from lowest to highest, are observed at the center of the cluster, whereas only those with masses not exceeding a certain threshold can be seen at the periphery. It is this effect that we call mass segregation. The younger the cluster, the stronger the segregation. A comparison of results for clusters of different ages shows that the form of the initial distribution of stars with radial distance does not change with time, and the observed flattening of this distribution is due to the burning out of massive stars at the cluster center.

Table 3. Parameters of 401 open clusters

Parameter	Number of clusters	Identifier	Unit of measure	Comment
IAU number	401			LCOC
Name	401			LCOC
J2000 right ascension	401	α	h	ASCC
J2000 declination	401	δ	deg	ASCC
Core radius (ASCC)	401	r_1^{ASCC}	deg	ASCC
Corona radius (ASCC)	401	r_2^{ASCC}	deg	ASCC
Core radius (USNO)[1]	140	r_1^{USNO}	deg	USNO
Corona radius (USNO)[1]	363	r_2^{USNO}	deg	USNO
Completeness B mag. limit of the catalog[1]	363	B_c	mag.	USNO
Number of most probable members	401	$N(P \geq 61\%)$		ASCC
Number of stars used to determine the mean proper motion	401	N_μ		ASCC
Proper motion in x	401	μ_x	0.001″/yr	ASCC
Standard error of proper motion in x	401	ε_{μ_x}	0.001″/yr	ASCC
Proper motion in y	401	μ_y	0.001″/yr	ASCC
Standard error of proper motion in y	401	ε_{μ_y}	0.001″/yr	ASCC
Distance	401	d	pc	
Color excess	401	$E(B-V)$	mag.	
Ref. for distance and color excess [2]	401	Ref.		

[1] In the absence of data the value is equal to zero.

[2] 1—[6–8], 2—[10], 3—LCOC, 4—[28], 5—this work.

This picture agrees with the distribution of evolved stars, which repeats that of the main-sequence stars.

The presence of segregation effects leads to important conclusions. It is evident from Fig. 6 that mass segregation is one of the factors leading to underestimation of cluster sizes (the brighter the limiting magnitude of the survey used to determine the size of a cluster and the farther the cluster from the Sun, the stronger the underestimation of the cluster radius). It is also very important to allow for segregation when constructing distributions of cluster stars such as the luminosity function or mass spectrum. Analyses of the central regions, to which most studies have been restricted, yield systematically underestimated contributions of faint stars, resulting in an apparent flattening of the cluster luminosity functions and mass spectra.

7. MEAN PROPER MOTIONS OF CLUSTERS

We computed the mean proper-motion components $\overline{\mu}_{x,y}$ of open clusters using at least five most probable members ($P \geq 61\%$) projected onto a region with the size of the cluster core and with $\varepsilon_{\mu_{x,y}} \leq 0.01''$/yr. The number of such stars reaches 60 for some clusters, with an average of 11.3 stars per cluster; the proper-motion components $\overline{\mu}_{x,y}$ of 85% of the clusters are determined with standard errors of less than 0.001″/yr. We have determined the proper motions of 183 clusters directly in the Hipparcos system for the first time.

Figure 7 compares the proper motions of open clusters determined in this paper and in [10, 11, 13, 15], based on the data from the Hipparcos [1] and Tycho-2 [2] catalog, and the "Catalog of about Four Million Stars" [16]. The proper motions determined in different studies using different techniques agree quite satisfactorily within several milliarcseconds per

year throughout the entire interval of μ values, including for clusters with small proper motions, which are difficult to distinguish from those of superimposed field stars. The few cases of large discrepancies, e.g., for α Per in [13], are due to typographical rather than real errors. The comparatively large scatter of the differences between our proper motions and those determined by Glushkova *et al.* [15] can be explained by the fact that the data of the catalog [15] have lower average accuracy compared to the ASCC, and their reduction to the Hipparcos system was performed indirectly via field stars, introducing additional errors.

8. CONCLUSIONS

This work is part of a project aimed at studies of open clusters based on the high-precision data typical of the post-Hipparcos era: the ASCC homogeneous all-sky catalog of astronomical data and the USNO catalog, which is currently the deepest available. This approach makes it possible to construct an all-sky system of self-consistent cluster parameters based on a homogeneous technique. One of the outputs of our project is a list of kinematic members of 401 clusters with various membership probabilities, including more than 28 000 stars (or 70 stars/cluster), which formed the basis of this study.

We have constructed a homogeneous system of structural parameters of the open clusters: their central coordinates and core and corona radii. The derived cluster sizes depend significantly on the selection of cluster members: our cluster sizes exceed those compiled in the most widely used source of open-cluster data—the Lyngå [5] catalog—by on average a factor of two to three. We were able to tie our radii to the standard system via comparison with the structural parameters of King models. Our core and coronal radii are equal to about $2r_c$ and $0.7r_t$, respectively. The computed linear cluster radii lie in the interval 2–20 pc. The parameters of the largest clusters resemble those of associations; for example, according to [30], the radius of one of the nearest OB associations, Per OB2, is 20–25 pc, whereas the R_2 values for α Per, NGC 2354, NGC 2439, NGC 2244, and NGC 2360 lie in the range 18–22 pc, and the radii of the clusters h and χPer are ≈ 80 pc, again emphasizing the lack of a clear boundary between open clusters and associations.

The available data suggest that appreciable segregation effects are typical of all clusters. It appears that the central concentration of stars of different masses does not change with time, and the apparent flattening of the radial distributions of stars of different masses is due to the burning out of massive stars in the central regions. Segregation is an important systematic effect capable of distorting the observed sizes of clusters and the slopes of the luminosity and mass functions of their constituent stars.

The mean proper motions of open clusters derived using our data extend the Hipparcos system by 183 new clusters whose proper motions had previously been unknown. The relatively large number of *bona fide* members with high-precision data enabled us to obtain proper motions comparable in quality with the original Hipparcos estimates. We have determined the distances and extinctions for 118 clusters for the first time by analyzing the color–magnitude diagrams for the selected cluster members.

The open-cluster parameters (both structural and kinematic) obtained in this paper are listed in the "Catalog of Structural and Kinematic Parameters of 401 Open Clusters." Table 3 gives a description of this catalog, which is available from the Strasbourg Astronomical Data Center.

9. ACKNOWLEDGMENTS

This work was partially supported by the Russian Foundation for Basic Research (project no. 01-02-1630).

REFERENCES

1. *The Hipparcos and Tycho Catalogues. Astrometric and Photometric Star Catalogues Derived from the ESA Hipparcos Space Astrometry* (ESA Publications Division, Noordwijk, Netherlands, 1997), ESA SP 1200, Vol. 17.
2. E. Høg, C. Fabricius, V. V. Makarov, *et al.*, *The Tycho-2 Catalogue: Positions, Proper Motions and Two-Color Photometry of the 2.5 Million Brightest Stars* (CD-ROM distribution) (Copenhagen Univ. Obs., 2000).
3. D. Monet, A. Bird, B. Canzian, *et al.*, *USNO-A 2.0: A Catalog of Astrometric Standards* (CD-ROM distribution) (US Naval Obs., Washington, 1998).
4. N. V. Kharchenko, Kinemat. Fiz. Neb. Tel **17**, 409 (2001); ftp://cdsarc.u-strasbg.fr/pub/cats/I/280 (2001).
5. G. Lyngå, *Catalogue of Open Clusters Data*, 5th ed. (CDS, Strasbourg, 1987).
6. A. V. Loktin, N. V. Matkin, and T. P. Gerasimenko, Astron. Astrophys. Trans. **4**, 165 (1994).
7. A. V. Loktin, T. P. Gerasimenko, and L. K. Malysheva, Astron. Astrophys. Trans. **20**, 607 (2001).
8. A. V. Loktin, T. P. Gerasimenko, and L. K. Malysheva, *Catalog of Open Cluster Parameters. Version 2.2*, private communication (2001).
9. J.-C. Mermilliod and C. Turon, in *The Hipparcos Mission* (European Space Agency, Paris, 1989), ESA SP 1111, Vol. 2, p. 177.
10. N. Robichon, F. Arenou, J.-C. Mermilliod, and C. Turon, Astron. Astrophys. **345**, 471 (1999).
11. H. Baumgardt, C. Dettbarn, and R. Wielen, Astron. Astrophys., Suppl. Ser. **146**, 251 (2000).

12. A. V. Loktin and G. V. Beshenov, Pis'ma Astron. Zh. **27**, 450 (2001) [Astron. Lett. **27**, 386 (2001)].
13. W. S. Dias, J. R. D. Lépine, and B. S. Alessi, Astron. Astrophys. **376**, 441 (2001).
14. W. S. Dias, J. R. D. Lépine, and B. S. Alessi, Astron. Astrophys. **388**, 168 (2002).
15. E. V. Glushkova, M. V. Zabolotskikh, A. S. Rastorguev, *et al.*, *Absolute Proper Motions of 331 Open Clusters* (http://www.sai.msu.su/groups/cluster/cl/ pm/, 1998).
16. A. P. Gulyaev and V. V. Nesterov, *Catalog of about Four Million Stars* [in Russian] (Mosk. Gos. Univ., Moscow, 1992).
17. P. N. Kholopov, *Star Clusters* [in Russian] (Nauka, Moscow, 1981).
18. V. M. Danilov and A. F. Seleznev, Astron. Astrophys. Trans. **6**, 293 (1993).
19. S. E. Urban, T. E. Corbin, and G. L. Wycoff, Astron. J. **115**, 2161 (1998).
20. E. Høg, A. Kuzmin, U. Bastian, *et al.*, Astron. Astrophys. **335**, L65 (1998).
21. B. M. Lasker, C. S. Sturch, B. J. McLean, *et al.*, Astron. J. **99**, 2019 (1990).
22. *Carlsberg Meridian Catalogue La Palma. No. 1–11. Observations of Positions of Stars and Planets: May 1984 to May 1998* (CD-ROM distribution) (Copenhagen Univ. Obs., Royal Greenwich Obs., and Real Instituto y Observatorio de la Armada en San Fernando, 1999).
23. S. Röser and U. Bastian, *PPM Star Catalogue. Positions and Proper Motions of 181 731 Stars North of −2.5° Declination for Equinox and Epoch J2000.0* (Spectrum Akademischer Verlag, Heidelberg, 1991), Vols. 1, 2.
24. U. Bastian, S. Röser, L. Yagudin, *et al.*, *PPM Star Catalogue. Positions and Proper Motions of 197 179 Stars South of −2.5° Declination for Equinox and Epoch J2000.0 (Spectrum Akademischer Verlag, Heidelberg, 1993)*, Vols. 3, 4.
25. S. Röser, U. Bastian, and A. Kuzmin, Astron. Astrophys., Suppl. Ser. **105**, 301 (1994).
26. *The Hipparcos and Tycho Catalogues. Astrometric and Photometric Star Catalogues Derived from the ESA Hipparcos Space Astrometry* (ESA Publications Division, Noordwijk, Netherlands, 1997), ESA SP 1200, Vols. 14–16.
27. Th. Schmidt-Kaler, *Landolt-Börnstein Numerical Data and Functional Relationships in Science and Technology. New Series. Group IV. Berlin-Heidelberg* (Springer-Verlag, New York, 1982).
28. J.-C. Mermilliod, *The Data Base for Stars in Open Clusters* (the Web version of BDA) (http://obswww.unige.ch/webda/, 1995).
29. I. King, Astron. J. **67**, 471 (1962).
30. A. N. Belikov, N. V. Kharchenko, A. E. Piskunov, *et al.*, Astron. Astrophys. **387**, 117 (2002).

Translated by A. Dambis

Astronomy Reports, Vol. 47, No. 4, 2003, pp. 276–287. Translated from Astronomicheskiĭ Zhurnal, Vol. 80, No. 4, 2003, pp. 304–316.

Study of the Star-Forming Region L379 IRS3 in CH_3OH and CS

V. G. Promyslov, G. M. Larionov, and S. V. Kalenskiĭ

Astro Space Center, Lebedev Institute of Physics, Russian Academy of Sciences, Profsoyuznaya ul. 84/32, Moscow, 117997 Russia

Received June 4, 2002; in final form, August 21, 2002

Abstract—A molecular cloud and high-velocity outflow associated with the star-forming region L379 IRS3 have been mapped in the 6_{-1}–5_0E methanol and CS (3–2) lines using the 12-meter Kitt Peak telescope. The estimated CS column density and abundance in the molecular cloud are 8×10^{14} cm^{-2} and 4×10^{-9}, respectively. LVG modeling of the methanol emission constrains the gas density in the cloud to $(1–4) \times 10^5$ cm^{-3} and the gas kinetic temperature to 20–45 K. The upper limit on the density of the high-velocity gas is 10^5 cm^{-3}. © *2003 MAIK "Nauka/Interperiodica".*

1. INTRODUCTION

High-velocity bipolar outflows are observed at early stages of the evolution of stars of various masses. Interaction of the high-velocity outflows with surrounding "quiescent" gas leads to shock heating of the medium and, consequently, to the evaporation of the molecular mantles of dust particles. As a result of this evaporation, the gas-phase abundance of ammonia, formaldehyde, methanol, and some other molecules is considerably enhanced [1]. Bipolar outflows create broad line wings, which are prominent in carbon monoxide (CO) lines, less pronounced in CS, HCN, and HCO^+ lines, and almost never observed in lines of more complex molecules.

Bright maser features in methanol lines have been detected in many star-forming regions. According to the classification of Menten [2], methanol masers can be divided into two classes: I and II. Class I masers are pumped by collisions in the absence of strong radiation, whereas class II masers are pumped by strong external radiation. The strongest and most widespread class I masers radiate in the 7_0–6_1A^+ and 4_{-1}–3_0E transitions at 7 and 8 mm, respectively; weaker masers have been found in the 8_{-1}–7_0E, 6_{-1}–5_0E, 8_0–7_1A^+, and other transitions at 1, 2, 3 mm, etc. Class II masers radiate in the 5_1–6_0A^+, 2_0–$3_{-1}E$, J_0–$J_{-1}E$, and other transitions.

Plambeck and Menten [3] have suggested that there is a connection between bipolar outflows and methanol masers. According to [3], class I methanol masers can arise in regions where the methanol abundance is enhanced by shock heating of the medium. Though more than ten years have elapsed since the publication of [3], the problem of the connection between methanol masers and bipolar outflows remains open and requires further study. One source suitable for such studies is the region of formation of massive stars L379 IRS3. It hosts three IRAS sources, the brightest of which is IRAS 18265–1517 ($RA(1950) = 18^h26^m32.9^s$, $DEC(1950) = -15°17'51''$). Strong class I masers in the 7_0–6_1A^+, 6_{-1}–5_0E, 5_{-1}–4_0E, and 4_{-1}–3_0E lines have been detected toward this region [4–6]; in addition, Val'tts *et al.* [7] have found quasithermal emission in the class I 8_0–7_1A^+ line. Wilking and Blackwell [8] and Kelly and Macdonald [9] have mapped the bipolar outflow in the (2–1) CO line. The 6_{-1}–5_0E and 5_{-1}–4_0E line profiles contain weak broad features, which could be associated with a high-velocity outflow. To determine the parameters of the high-velocity and quiescent gas and establish whether the methanol masers are associated with the high-velocity outflow, we undertook a study of this source in the 6_{-1}–5_0E and other methanol lines. To obtain more information about the source, we also observed the L379 IRS3 region in CS lines.

2. OBSERVATIONS AND RESULTS

We have mapped the source in the 6_{-1}–5_0E methanol line and the (3–2) CS line. The observations were carried out on the 12-m NRAO[1] Kitt Peak antenna[2] in remote-observing mode from the Astro Space Center of the Lebedev Institute of Physics (Moscow). Beam switching with a beam offset of 20′ in azimuth was used for both lines. The pointing accuracy was checked using observations of planets, and was no worse than 5″ in azimuth and elevation.

[1] NRAO is operated by the Associated Universities, Inc., under contract to the National Science Foundation.

[2] Now operated by the University of Arizona.

1063-7729/03/4704-0276$24.00

Table 1. Parameters of the antennas and observed lines (KP: Kitt Peak; OSO: Onsala)

Molecule	Transition	Frequency, GHz	Line strength	Antenna	HPBW
CH_3OH	$5_{-1}-4_0E^*$	84.52121	1.485	OSO	44″
CH_3OH	$8_0-7_1A^+$	95.16944	3.483	OSO	39
CH_3OH	$2_{-1}-1_{-1}E$	96.73939	1.5	OSO	39
CH_3OH	$2_0-1_0A^+$	96.74142	2	OSO	39
CH_3OH	2_0-1_0E	96.74458	2	OSO	39
CH_3OH	2_1-1_1E	96.75551	1.5	OSO	39
CH_3OH	$6_{-1}-5_0E$	132.89079	1.776	KP	47
CH_3OH	$5_{-2}-6_{-1}E$	133.60550	0.766	KP	47
CH_3OH	$5_0-5_{-1}E^{**}$	157.17897	2.388	KP	40
CH_3OH	$4_0-4_{-1}E^{**}$	157.24610	2.009	KP	40
CH_3OH	$9_0-8_1A^+$	146.61882	4.017	KP	43
CS	$2-1^{***}$	97.980968	2	OSO	39
CS	3–2	146.969049	3	KP	43
$C^{34}S$	2–1	96.412982	2	OSO	39

* From Kalenskiĭ *et al.* [6].

** From Slysh *et al.* [18].

*** From Larionov *et al.* [11].

The beamwidths at both frequencies are given in Table 1. A dual-channel cooled SIS receiver was used to obtain simultaneous observations in two orthogonal polarizations. The data were calibrated using the vane method. A 1500-channel autocorrelator with 600-MHz bandwidth and 400-kHz resolution was used as the spectrometer.

Observations in the $6_{-1}-5_0E$ methanol line were carried out on January 27 and 28, 2000. The transition frequency 132.89079 GHz was taken from the catalog of Lovas [10]. The system noise temperature corrected for atmospheric absorption, spillover, and ohmic losses varied from 300 to 400 K depending on the weather conditions and source elevation. The source was mapped in 48 positions with a nonuniform sampling interval to decrease the required observation time. The mapped region covers an area of $\approx 3' \times 2'$ around IRAS 18265−1517. In regions where no emission was detected, we observed only reference points at intervals of 40″, whereas we mapped four to five points per beam in regions with a strong signal, yielding a sampling interval of $\approx 10''$.

Observations in the (3–2) CS and $9_0-8_1A^+$ methanol lines (at 146.969049 and 146.61882 GHz, respectively) were carried out in June 2000. The transition frequencies were taken from [10]. The system temperature varied from 250 to 800 K depending on the weather conditions and source elevation. Fifty-one positions in a $\approx 3' \times 3'$ area around IRAS 18265−1517 were observed. In regions where no emission was detected, we observed two points per beam with a sampling interval of 20″. In regions with strong emission, we observed three to four points per beam, yielding a sampling interval of $\approx 10''$.

In addition, we carried out observations in the $8_0-7_1A^+$ and 2_K-1_K methanol lines at 95.2 and 96.7 GHz and in the (2–1) $C^{34}S$ line at 96.4 GHz in May 2001 on the 20-m radio telescope in Onsala (Sweden). The antenna parameters and observational procedure were analogous to those described by Larionov *et al.* [11].

The spectra were processed using the UNIPOPS software package. The maps were constructed using the maximum entropy method (MEM) in the realization described by Promyslov [12].

The resulting maps are presented in Figs. 1–4. We used the integrated intensity in the corresponding radial-velocity interval as the "signal" when constructing the maps. The axes are the projected distances in arcseconds from IRAS 18265−1517. The observed positions are marked by dots. The lower left corner of each map shows the effective beam for strong features (see next section). A contour drawn

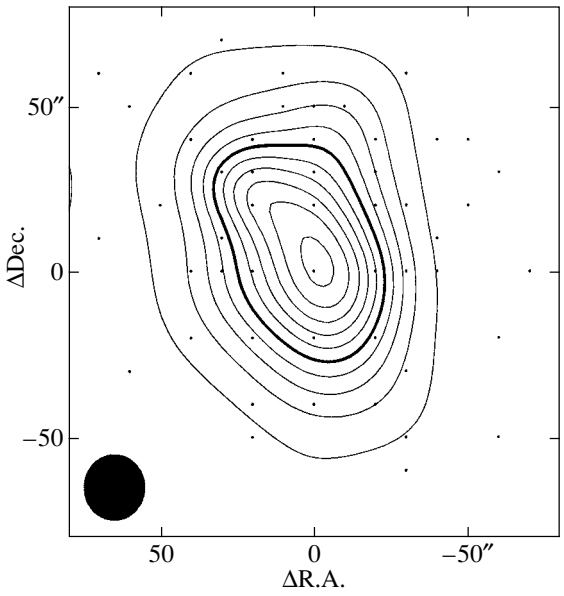

Fig. 1. Map of L379 IRS3 integrated over the (3–2) CS line profile in the radial-velocity interval 12–24 km/s. Contours are drawn at 10, 20, 30, 40, 50, 60, 70, 80, 90, and 95% of the peak (26 K km/s). The observed positions are marked by dots. The effective beam size is shown in the lower left-hand corner of the map. The bold contour delimits the area within 50% of the peak integrated intensity for this map.

in bold delimits the area within 50% of the maximum integrated intensity for the given map.

3. ESTIMATED RESOLUTION OF THE OBTAINED MAPS

The maximum-entropy method allows us to achieve "superresolution" in the images obtained. The effective resolution in MEM maps depends on the signal-to-noise ratio for a particular feature, the sampling step in declination and right ascension, and the structure present in the image. Therefore, it can vary from map to map and from feature to feature. To estimate the resolution of a MEM map and the relationship between the actual and effective beam, special modeling is required.

The effective beamwidth was determined using the method proposed in [13]. In accordance with this method, we synthesized series of model maps of a pointlike source convolved with the radio telescope beam, with fluxes equal to 20–100% of the flux of the most intense feature on the actual map. The filling of the image plane by "observational points" and the noise at each point were the same as in the actual map of the source. These synthesized maps were then processed using the same MEM algorithm. The sizes of the resulting images of pointlike sources at 50% of the intensity maximum were adopted as the effective beamwidth.

It turned out that the spatial resolution for the strongest features on our MEM maps was improved by a factor of approximately 2–2.5 compared to the original maps. For a joint analysis of the restored images, the resolution for the strongest features on all the maps was reduced to $\approx 25''$ by convolving the restored maps with appropriate Gaussians.

4. ANALYSIS AND DETERMINATION OF THE SOURCE PARAMETERS

The profile of the CS lines (Fig. 5) can tentatively be divided into three parts: radial velocities less than 12 km/s refer to the blue wing of the bipolar outflow, radial velocities from 12 to 24 km/s correspond to the emission of quiescent gas, and radial velocities higher than 24 km/s refer to the red wing. This division of the line profile into components is close to that done by Wilking *et al.* [8] for observations in the (2–1) ^{12}CO and ^{13}CO lines. The 5_{-1}–4_0E, 6_{-1}–5_0E, and 2_K–1_K methanol lines fall outside 12–24 km/s (Fig. 6), so that the bipolar-outflow wings are observed in these lines. However, the spectra of these lines display no clearcut boundary between the central part and the bipolar-outflow wings. Narrow maser features at velocities of 15–22 km/s are prominent in the spectra of the 5_{-1}–4_0E, 6_{-1}–5_0E, and 8_0–7_1A^+ lines.

4.1. The Molecular Cloud

The emission of quiescent gas (the molecular cloud) is observed at velocities of 12–24 km/s. Figure 1 shows the integrated map of the molecular cloud in the (3–2) CS line. This map essentially coincides with the map of the cloud in the (2–1) C^{18}O line but differs from the (2–1) CO map of Kelly and Macdonald [9]. The differences between the (3–2) CS and (2–1) CO maps are due to the fact that the CO line is optically thick, so that the contribution of the molecular cloud to the integrated CO (2–1) map is distorted by the contribution of the bipolar-outflow wings. The C^{18}O line is optically thin ($\tau = 0.2$–0.4) [9], and the main contribution to the integrated map is made by emission of the molecular cloud. The region of emission has a nearly circular shape and a diameter of about 55″ (at the half-maximum level). As in the C^{18}O line, the emission peak is close to the position of IRAS 18265–1517. However, there are also differences between the CS and C^{18}O maps. The main one is that the CS peak has a northeast extension that is absent from the C^{18}O map.

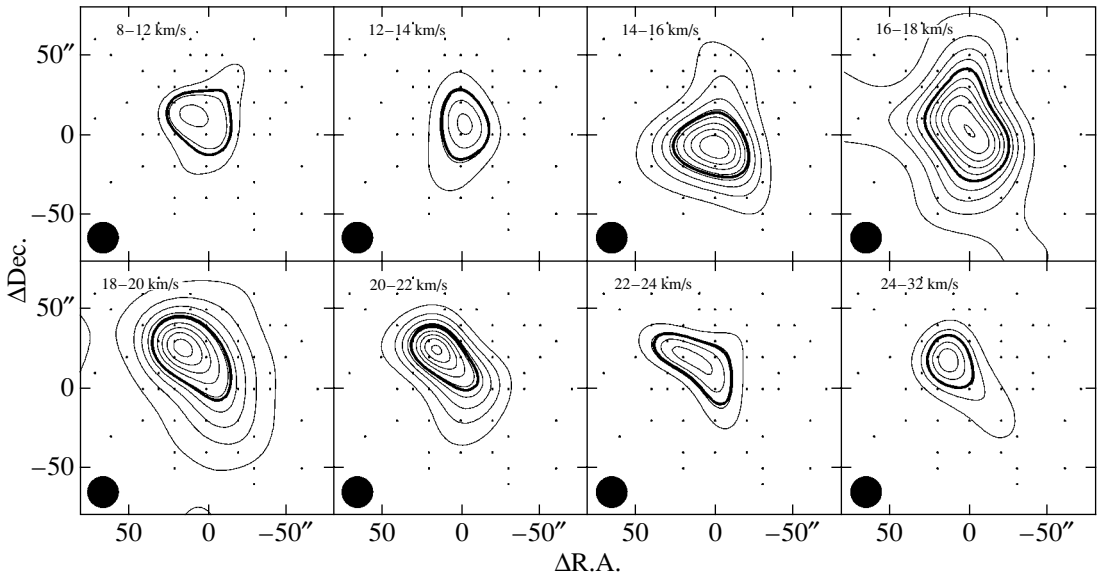

Fig. 2. Maps of L379 IRS3 in the (3–2) CS line. Contours are drawn at 10, 20, 30, 40, 50, 60, 70, 80, and 90% of the peak (7.9 K km/s), which occurs in the velocity interval 16–18 km/s. The observed positions are marked by dots. The effective beam size is shown in the lower left-hand corner of the map. The bold contour delimits the area within 50% of the peak.

The differences between the CS and $C^{18}O$ maps for various spectral intervals are more pronounced. In the CS line, appreciable emission is observed at velocities of 12–14 and 22–24 km/s, where $C^{18}O$ emission is virtually absent. The positions of the CS and $C^{18}O$ peaks in the velocity interval 18–20 km/s differ considerably: the $C^{18}O$ peak is shifted relative to IRAS 18265–1517 by about (−15″, 15″) in declination and right ascension, is shifted relative to the CS line by (15″, 25″), and virtually coincides with the peak of the red wing (Fig. 2). The positions of the CS and $C^{18}O$ peaks also differ in the interval 20–22 km/s; the CS peaks at 18–20 and 20–22 km/s coincide with the peak of the red wing in the $C^{18}O$ map. Therefore, we suggest that the peaks are due to the contribution of the bipolar-outflow gas, which either has already stopped its motion or is moving in the tangential direction. The offset of the CS emission at 18–20 and 20–22 km/s relative to IRAS 18265–1517 gives rise to the northeast extension in the integrated map. The wings are virtually absent in the $C^{18}O$ line (see [9, Figs. 3 and 4]), and it is reasonable to assume that the contribution of high-velocity gas to the $C^{18}O$ emission is negligible at 18–22 km/s, providing an explanation for the difference between the maps.

Figure 3 shows the maps of L379 IRS3 in the 6_{-1}–5_0E methanol line. The velocity intervals 12–14 and 22–24 km/s correspond to the molecular cloud. The region of methanol emission in these intervals lies to the north of IRAS 18265–1517 and is located in the same place as the region of CS emission in the corresponding radial-velocity intervals and the bipolar-outflow wings (Fig. 3). However, the details of these maps differ appreciably.

Since the methanol line emission comes from the

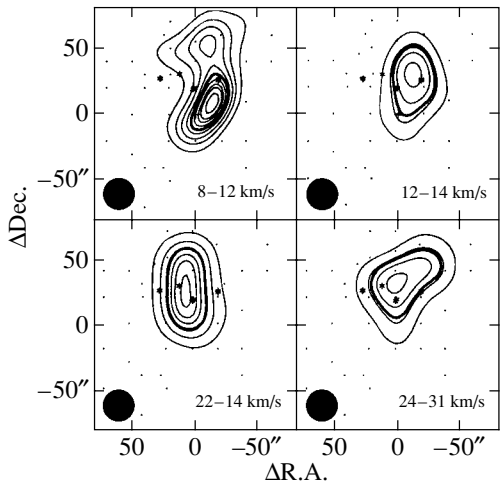

Fig. 3. Maps of L379 IRS3 in the 6_{-1}–5_0E CH_3OH line in the radial-velocity intervals 8–12, 12–14, 22–24, and 24–31 km/s. Contours are drawn at 10, 20, 30, 40, 50, 60, 70, 80, and 90% of the peak (1.34 K km/s), which occurs in the velocity interval 8–12 km/s. The observed positions are marked by dots. The effective beam size is shown in the lower left-hand corner of the map. The bold contour delimits the area within 50% of the peak.

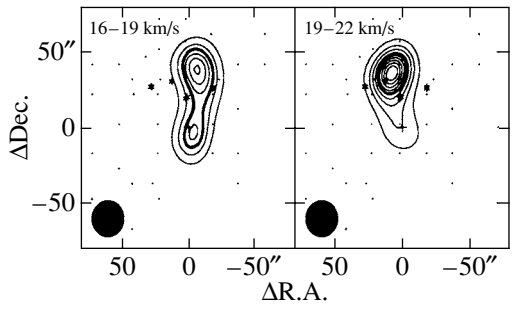

Fig. 4. Maps of L379 IRS3 in the 6_{-1}–5_0E CH_3OH line at radial velocities of 16–19 and 19–22 km/s. Contours are drawn at 10, 20, 30, 40, 50, 60, 70, 80, and 90% of the peak (11 K km/s), which occurs in the velocity interval 19–22 km/s. The observed positions are marked by dots. The effective beam is shown in the lower, left-hand corner of each map. The bold contour delimits the area within 50% of the peak.

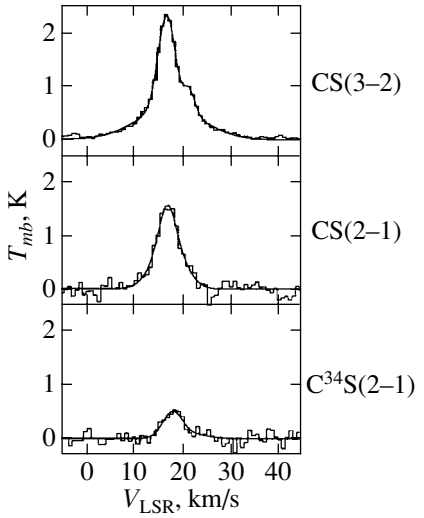

Fig. 5. Spectra of L379 IRS3 in the (3–2), (2–1) CS and (2–1) $C^{34}S$ lines toward IRAS 18265–1517. The vertical lines at +12 and +25 km/s show the boundaries between the high-velocity and quiescent gas.

same region as the bipolar-outflow wings, we suppose that, like the CS line in the intervals 18–20 and 20–22 km/s, the main contribution to the 133-GHz emission comes from the bipolar-outflow gas [14].

4.2. Column Density and Abundance of CS and CH_3OH in the Molecular Cloud

Analytical estimates

Observations of an optically thin molecular line enable us to determine the column density of molecules in the upper level, N_u:

$$\frac{N_u}{g_u} = \frac{3kW}{8\pi^3\nu_0\mu^2 S}. \quad (1)$$

Here, $W = \int T^*_{mb}(V_r)dV_r$ is the integrated line intensity, μ is the permanent electric dipole moment (1.96 D for the CS molecule), and $g_u = 2J_u + 1$ is the rotational statistical weight of the upper level. If the line is not optically thin, the value obtained from (1) must be multiplied by $\tau/(1 - \exp(-\tau))$, where τ is the line optical depth.

If the level populations are thermalized by collisions, the column density of molecules is related to N_u/g_u as

$$N = \frac{N_u}{g_u} Q \exp\left(\frac{E_u}{kT_{kin}}\right), \quad (2)$$

where E_u is the upper level energy and Q is the rotational statistical sum of the molecule. In the case of a linear molecule, $Q = kT_{kin}/hB$, where B is the rotational constant.

We have estimated the CS column density from the integrated intensity of the (2–1) CS line (Table 2). We derived the optical depth at the line center from the integrated intensity of the (2–1) $C^{34}S$ line (Table 2) using the relationship

$$W_{CS}/W_{C^{34}S} = X(CS)/X(C^{34}S)(1 - \exp(-\tau))/\tau. \quad (3)$$

Here, it is assumed that the profiles of the line absorption coefficients are identical and that the (2–1) $C^{34}S$ line is optically thin. We adopted the abundance ratio $X(CS)/X(C^{34}S) = 22.5$ [15]. The optical depth turned out to be 3.5. Assuming a gas temperature of 30 K (the average of the temperature range 20–40 K given by Kelly and Macdonald [9] and taking $B =$ 24 584.35 MHz, we obtain the CS column density 8×10^{14} cm^{-2}. Assuming a hydrogen column density of 2×10^{23} cm^{-2} [9], we obtain the CS abundance 4×10^{-9}, consistent with previous estimates of the CS abundance for the quiescent gas [16].

The methanol column density and abundance were determined from the 2_0–1_0A^+ line emission at 96.7 GHz. Assuming this line was optically thin, we obtained a methanol column density of 7.5×10^{14} cm^{-2} and an abundance relative to hydrogen of 3.8×10^{-9}; these are values typical of warm clouds [17]. Calculating the methanol column density with the $4_0 - 4_{-1}E$ line at 157 GHz, observed by Slysh *et al.* [18], yields a value ten times smaller (0.7×10^{14} cm^{-2}). This discrepancy is due to underpopulation of the upper level of this transition, 4_0E, at densities on the order of 10^5 cm^{-3} [18].

Table 2. Gaussian parameters of the lines observed toward IRAS 18265−1517

Molecule	Transition	$T_{mb}dV$, K km/s	V_{LSR}, km/s	ΔV, km/s	T_{mb}, K
CH_3OH	$2_{-1}-1_{-1}E$	6.52(0.14)	18.96(0.06)	5.60(0.07)	1.09
CH_3OH	$2_0-1_0A^+$	7.97(0.15)	18.96(0.06)	5.60(0.07)	1.34
CH_3OH	2_0-1_0E	2.48(0.15)	18.96(0.06)	5.60(0.07)	0.42
CH_3OH	2_1-1_1E	0.54(0.13)	18.96(0.06)	5.60(0.07)	0.09
CH_3OH	$5_{-1}-4_0E$	4.15(0.17)	18.22(0.18)	2.04(0.18)	1.91
		10.9(0.17)	18.73(0.18)	9.72(0.18)	1.05
		4.15(0.17)	20.35(0.18)	1.51(0.18)	2.58
CH_3OH	$8_0-7_1A^+$	4.44(0.45)	17.63(0.05)	1.78(0.15)	2.34
		5.38(0.64)	19.178(0.40)	6.58(0.65)	0.77
CH_3OH	$5_{-2}-6_{-1}E$				<0.09
CH_3OH	$6_{-1}-5_0E$	1.54(0.12)	17.84(0.10)	2.7(0.28)	0.54
		4.25(0.39)	18.13(0.12)	8.9(0.45)	0.45
		0.73(0.07)	20.23(0.086)	1.64(0.18)	0.42
CH_3OH	$9_0-8_1A^+$	3.09(0.08)	18.26(0.1)	4.84(0.25)	0.60
CH_3OH	$5_0-5_{-1}E^*$	1.52(0.098)	17.92(0.26)	5.99(0.41)	0.24(0.01)
CH_3OH	$4_0-4_{-1}E^*$	2.42(0.125)	18.07(0.14)	6.01(0.33)	0.38(0.015)
CS	2−1**	8.43(0.92)	17.66(0.14)	5.63(0.66)	1.41
		14.9(1.80)	17.39(0.38)	15.8(1.64)	0.88
CS	3−2		16.96(0.05)	4.23(0.05)	2.44
			21.77(0.05)	2.84(0.05)	0.65
			17.63(0.05)	18.0(0.05)	0.65
$C^{34}S$	2−1	5.55(0.65)	18.8(0.35)	6.0(0.86)	0.87

* Reanalyzed data of Slysh *et al.* [18].

** Reanalyzed data of Larionov *et al.* [11].

Calculations of statistical equilibrium

As is clear from [16, 18] and the current work, numerous methanol lines have been detected in L379 IRS3, both maser and thermal. We have selected 11 methanol lines (Table 3) observed toward IRAS 18265−1517 with a resolution of about 40″ and attempted to estimate the parameters of the emitting gas from these lines, approximating the available spectra with sets of Gaussians. The interval 8−30 km/s was divided into 2-km/s segments, and we calculated the approximated integrated intensity $W = \int_{v_{\min}}^{v_{\max}} G(V_r)dV_r$ for each segment, where $v_{\min}$, $v_{\max}$ are the lower and upper boundaries of a segment and $G(V_r) = \sum_i T_i(V_r)$ is the approximating line profile, i.e., the profile formed by the sum of the approximating gaussians. We computed an error σ^{ap} for each approximated integrated intensity [19]. Using the Large Velocity Gradient (LVG) method, we computed a grid of models for kinetic temperatures 10−100 K, gas densities 0.32×10^4−10^8 cm^{-3}, and specific methanol column densities $N/\Delta V = 0.2 \times 10^{13}$−$0.2 \times 10^{18}$ cm^{-2} (km/s)$^{-1}$. From these models we selected those best fitting the observational data according to the χ^2 criterion

$$\chi^2 = \sum_i \frac{(R_i^{obs} - R_i^m)^2}{(\sigma_i)^2}. \qquad (4)$$

Here, R_i^{obs} and R_i^m represent the approximated and model ratios of the integrated intensities in line i to the approximated integrated intensity of the $5_{-1}-4_0E$ line at 84 GHz, $R_i = W_i/W_{84}$; σ_i is the rms deviation

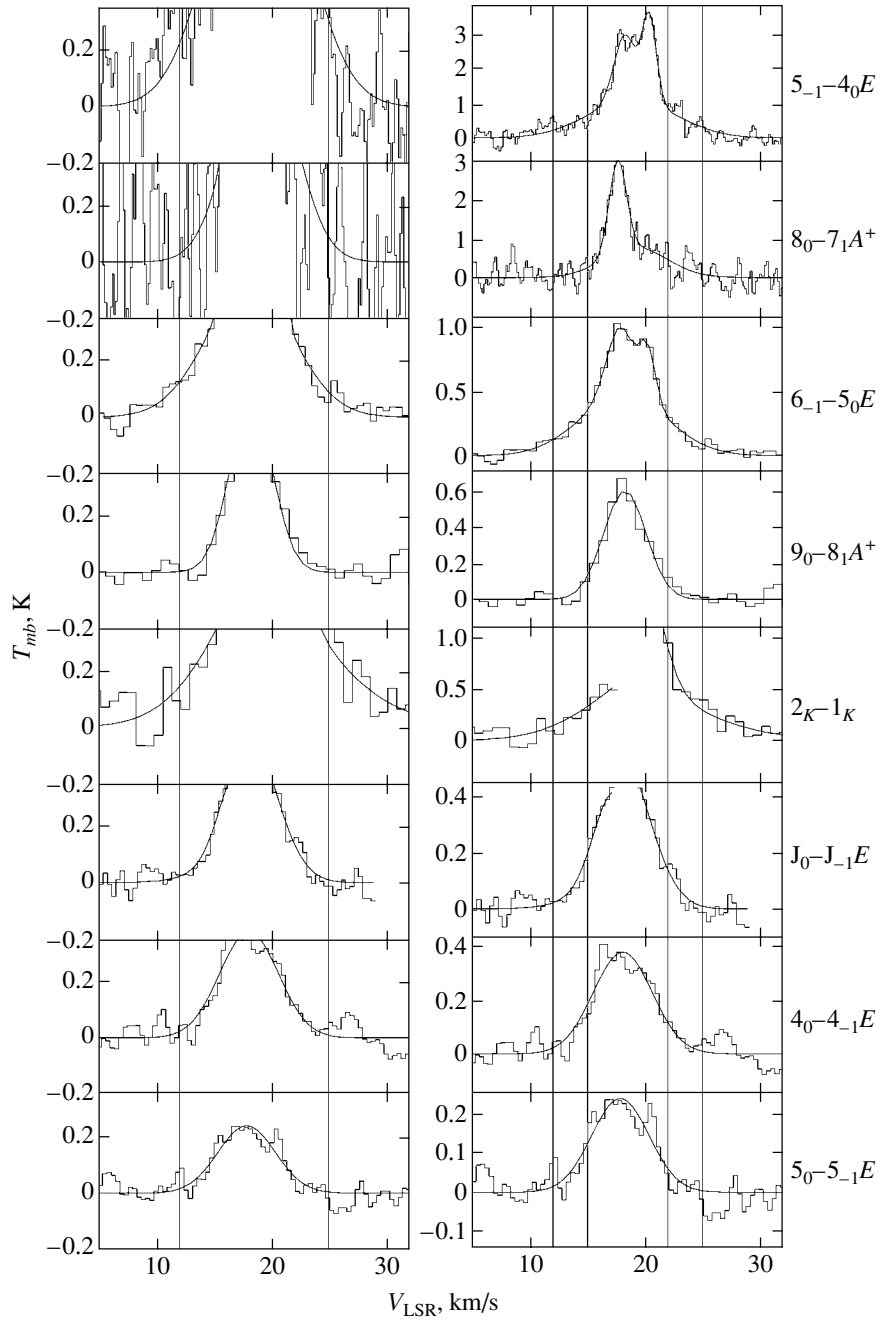

Fig. 6. Spectra of ten methanol lines toward IRAS 18265−1517 measured with an angular resolution of about 40″. The vertical lines at +12 and +25 km/s mark the boundaries between the high-velocity and quiescent gas, and the vertical lines at +15 and and +22 km/s mark the boundaries of the maser features in the 6_{-1}–5_0E and 5_{-1}–4_0E methanol lines. Spectral features are shown on an expanded scale to the left.

of this ratio, calculated as

$$\sigma_i = \sqrt{(W_i/W_{84}^2)^2 \times (\sigma_{84}^{ap})^2 + (1/W_{84})^2 \times (\sigma_i^{ap})^2}. \quad (5)$$

Values of χ^2 were calculated for each of the velocity intervals listed in Table 3. The χ^2 distribution has $s = 7$ degrees of freedom, and the value $\chi^2 < 6.35$ demonstrates that the probability that the model agrees with the observations is $\geq 50\%$. Models with such χ^2 values were found for the velocity intervals 10–12, 12–14, 22–24, and 24–26 km/s. The results of the calculations for these intervals are given in Fig. 7. We found no solutions with χ^2 less than

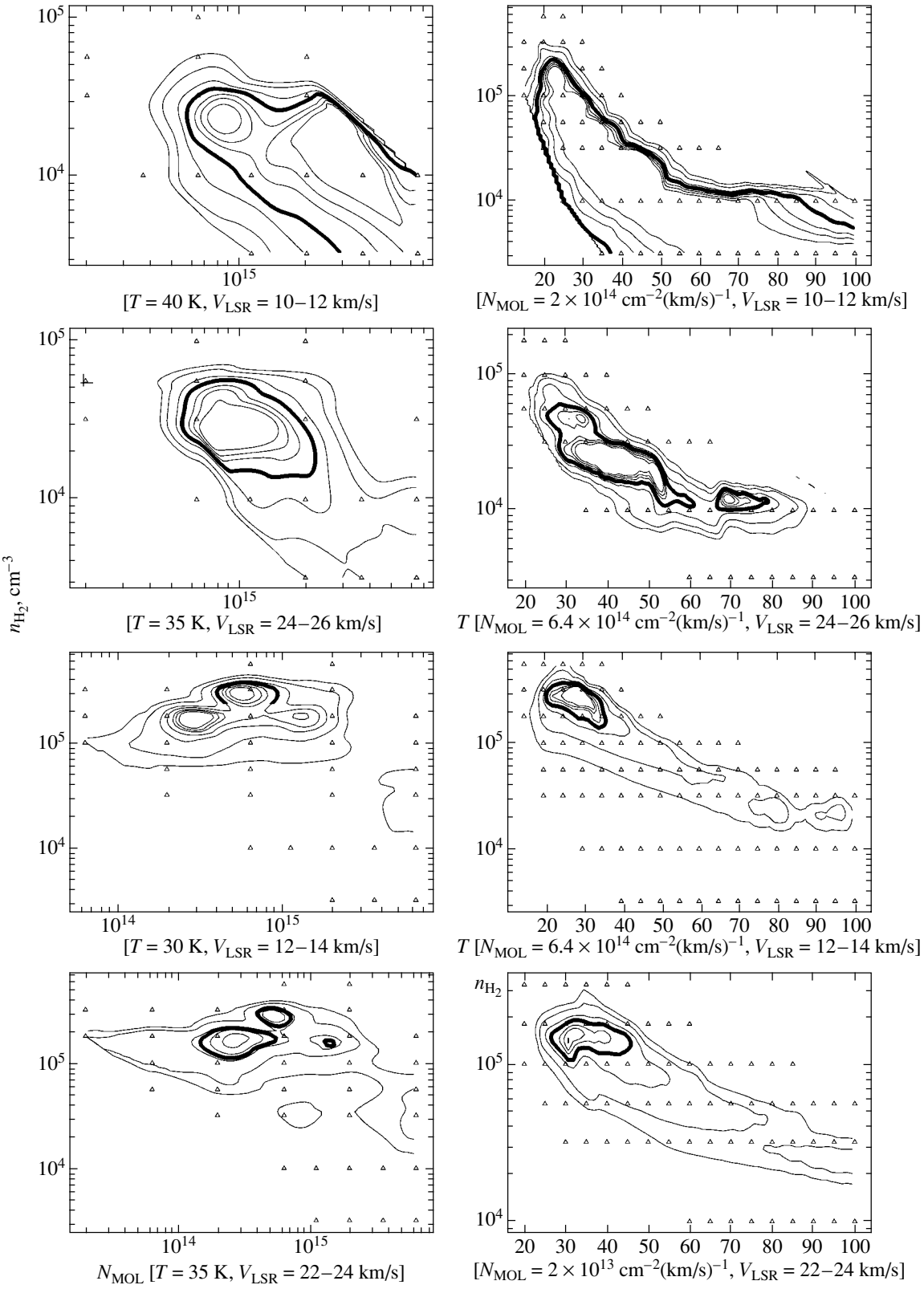

Fig. 7. Results of modeling of the methanol emission in L379 IRS3. The vertical axis plots the hydrogen density, and the horizontal axis plots the kinetic temperature (right) and specific methanol column density (left). The figures in brackets give the values of the fixed parameters for which the plots are given.

Table 3. Approximated integrated intensities of the methanol lines

Transition	Interval, km/s						
	8–10	10–12	12–14	22–24	24–26	26–28	28–30
	$\frac{W,\ \mathrm{K\,km/s}}{\sigma^{ap},\ \mathrm{K\,km/s}}$						
5_{-2}–$6_{-1}E$	0	0	0	0	0	0	0
	0.09	0.09	0.09	0.09	0.09	0.09	0.09
5_{-1}–4_0E	0.136	0.37	0.808	1.251	0.67	0.290	0.099
	0.016	0.056	0.068	0.106	0.062	0.031	0.016
1_0–$1_{-1}E$*	–	–	–	0.162	0.031	0.0035	0.0002
	–	–	–	0.035	0.007	0.001	9.08×10^{-5}
2_0–$2_{-1}E$**	0.0005	0.01	0.086	–	–	–	–
	1.35×10^{-4}	0.002	0.014	–	–	–	–
5_0–$5_{-1}E$	0.0013	0.013	0.079	0.0703	0.011	0.001	5.5×10^{-5}
	0.00046	0.005	0.018	0.0146	0.0035	0.00038	2.5×10^{-5}
4_0–$4_{-1}E$	0.00171	0.0163	0.102	0.117	0.019	0.002	9.07×10^{-5}
	0.00032	0.0034	0.018	0.017	0.004	0.00044	2.66×10^{-5}
9_0–8_1A^+	8.95×10^{-5}	0.0034	0.055	0.0982	0.008	0.0002	3.31×10^{-6}
	1.83×10^{-5}	0.00046	0.007	0.013	0.0012	4.85×10^{-5}	3.34×10^{-6}
8_0–7_1A^+	0.0026	0.024	0.144	0.615	0.18	0.0351	0.004
	0.0009	0.00718	0.036	0.129	0.047	0.01	0.0014
6_{-1}–5_0E	0.101	0.224	0.416	0.571	0.247	0.114	0.031
	0.057	0.123	0.201	0.21	0.109	0.057	0.024
2_{-1}–$1_{-1}E$*	–	–	–	1.198	0.634	0.397	0.234
	–	–	–	0.21	0.12	0.078	0.049
2_0–1_0E**	0.129	0.24	0.416	–	–	–	–
	0.035	0.063	0.12	–	–	–	–

* Due to line blending, only an upper limit for the intensity of the red-wing velocity interval was found.

** Due to line blending, only an upper limit for the intensity of the blue-wing velocity interval was found.

one hundred for the intervals 8–10, 26–28, and 28–30 km/s.[3] It appears that the approximation of the spectrum by sums of Gaussians is unsatisfactory in intervals with weak signals at the wing edges.

The contours in Fig. 7 correspond to $\chi^2 = 2.5, 3.5, 4.5, 6.5, 10, 15$, and 20. The first four contours correspond to confidence levels of approximately 90, 80, 70, and 50%, respectively. The bold contour delimits the region with $\chi^2 \leq 6.5$.

[3] Since the contribution of the maser emission is great at 16–22-km/s, we have done no modeling for this velocity interval.

The intervals 10–12 and 24–26 km/s correspond to the line wings, and the modeling results for these intervals are considered in the next section. Here, we analyze the results for 12–14 and 22–24 km/s, corresponding to the molecular cloud.

According to Fig. 7, the gas density in the cloud can be constrained to be $(1–4) \times 10^5$ cm^{-3} and the kinetic temperature to be T_{kin} at 20–45 K. These figures agree well with the parameters of the molecular cloud obtained by Kelly and Macdonald [9] ($T_{kin} \approx 30$ K, $n_{\mathrm{H_2}} = (1–2) \times 10^{15}$ cm^{-3}). However, in models that reproduce the observed line intensity

ratios, the line brightness temperature turned out to be much higher than the observed value (10 K and higher). Accordingly, the *specific* column density, $\approx 10^{15}$ cm^{-2} (km/s)$^{-1}$, was higher than the *total* methanol column density in the cloud calculated analytically (7.5×10^{14} cm^{-2}). This discrepancy between the models and observational data is partially explained by the offset of the emission peaks at both 12–14 km/s and 22–24 km/s by 20″–30″ to the north and northwest of the IRAS source. However, the observed intensity of the 133-GHz emission is also considerably weaker than is predicted by our models near the peaks. This discrepancy suggests that either the gas is clumpy, diluting the emission, or the emission arises in a thin layer of gas.

4.3. High-Velocity Outflow

The high-velocity outflow of matter shows itself as wings in the CS and CH_3OH lines. Maps of the bipolar outflow in the (3–2) CS line are presented in Fig. 2 (the radial-velocity intervals 8–12 and 24–31 km/s). The red wing is extended in the northeast–southwest direction, and the emission peak is observed at a projected distance of (+15″, +20″) from IRAS 18265–1517 and approximately coincides with the peak of the red wing in the bipolar-outflow CO (2–1) map [9]. The blue wing is slightly extended in the northwest–southeast direction. The emission peak is (+10″, +15″) from IRAS 18265–1517 and is offset approximately 20″ to the east of the blue-wing peak in the map of Kelly and Macdonald [9].

The bipolar-outflow map in the 6_{-1}–5_0E methanol line is given in Fig. 3. The red and blue wings strongly overlap, but their maxima are separated by 20″–25″. The red-wing and blue-wing peaks approximately coincide with the corresponding peaks in the wings of the CS and CO lines. The position offsets of the CH_3OH and CO peaks are about 7″ for the blue wing and about 15″ for the red wing. However, like the CS line wings, there is virtually no emission in the methanol line wings to the south of the central source, which is clearly visible in the bipolar-outflow CO map. The smaller sizes of the bipolar outflow in the methanol and CS lines derived by us may be due to the fact that we have used a narrower range of radial velocities when constructing the maps. In particular, we used the velocity intervals 8.5–12 and 24–31 km/s for the map in the methanol line and −10 to 10 and 25–40 km/s for the CO map.

Kelly and Macdonald [9] proposed a model in which this region contains two outflows, with the center of one located to the north and the center of the other located to the south of IRAS 18265–1517. If this model is correct, we observe only the northern outflow in the CS and methanol lines.

4.4. Parameters of the High-Velocity Gas

Wings are observed in the 6_{-1}–5_0E, 5_{-1}–4_0E, and 2_K–1_K methanol lines (Fig. 6). The 6_{-1}–5_0E and 5_{-1}–4_0E lines belong to class I maser transitions according to the classification of Menten [2]; the 2_K–1_K transitions are purely thermal; i.e., only thermal emission is observed in these lines. No wings have been detected in the class II J_0–$J_{-1}E$ and 5_{-2}–$6_{-1}E$ lines. It is known that the upper levels of class II lines are underpopulated in the absence of strong external radiation at densities on the order of 10^5–10^6 cm^{-3} or lower [18]. Therefore, the absence of wings in the class II lines testifies that (1) there is no strong external radiation in the high-velocity gas and (2) the density of the high-velocity gas does not exceed 10^5–10^6 cm^{-3}.

Note that wings are also absent from the class I 8_0–7_1A^+ and 9_0–8_1A^+ lines. This probably indicates that the temperature and/or density of the high-velocity gas are insufficient to populate the upper levels of these transitions, located at 58.062 and 72.570 cm^{-1}, respectively.

The results of LVG modeling for 10–12 and 24–26 km/s are shown in Fig. 7,[4] which demonstrates that the density of the high-velocity gas is constrained from above to values of the order of 10^5 cm^{-3}.

As in the case of the molecular cloud, the brightness temperature of the methanol lines in the models we selected as "matching the observations" is considerably higher than the observed value. This discrepancy can be explained in a similar way; i.e., either the gas is clumpy or the emission arises in a thin layer of gas.

5. METHANOL MASERS

Methanol masers in L379 IRS3 were first detected by Kalenskiĭ *et al.* [4] in the 7_0–6_1A^+ line at 44 GHz and the 4_{-1}–3_0E line at 36 GHz. Later, Kogan and Slysh [20] and Slysh *et al.* [21] carried out interferometric observations of L379 IRS3 at 44 GHz and found that the source consists of individual maser spots, located approximately 30″ to the north of IRAS 18265–1517. Kogan and Slysh [20] separated the masing region into western and eastern parts; the western part includes maser spots with emission peaks at 16.3–18.8 km/s, while the eastern part contains masers with emission peaks between 18.8 and 20.8 km/s. The strongest 44-GHz masers are located in the western part. Slysh *et al.* [5] and Kalenskiĭ *et al.* [6] have detected masers in the

[4] As noted above, we could not model the methanol emission at 8–10, 26–28, or 28–30 km/s.

6_{-1}–5_0E and 5_{-1}–4_0E lines at 133 and 84 GHz, respectively. The maser emission at both 133 GHz and at 84 GHz can be decomposed into two components with peaks at about 18 and 20 km/s, which probably correspond to the western and eastern parts of the masing region (Fig. 4).

The masers at 44, 84, and 133 GHz belong to class I and are excited by collisions. We observed two other maser transitions of the same class: 8_0–7_1A^+ at 95 GHz and 9_0–8_1A^+ at 146 GHz. At 95 GHz, we detected a narrow feature at 17.63 km/s, against the background of a broader line (Table 2, Fig. 6).[5] The narrow feature is probably a maser line and belongs to the western part. At 146 GHz, we found a quasithermal line with a peak at 18.26 km/s; however, this line is slightly narrower (4.84 km/s, Table 2) than the thermal 5_0–$5_{-1}E$ and 4_0–$4_{-1}E$ lines (6 km/s, Table 2). Therefore, it is possible that a maser contribution is also present at 146 GHz.

The asterisks in Figs. 3 and 4 mark the positions of the 44-GHz class I methanol masers taken from [21]. Figure 3 shows that the maser sources coincide spatially with the wings of the bipolar outflow. This is consistent with the hypothesis that the methanol masers are associated with the bipolar outflows (see Introduction). This raises the question of why in this case the radial velocities of the class I methanol masers *virtually always* coincide with the velocity of the quiescent gas.

Models of cosmic maser sources can be conditionally divided into two groups. The first includes models in which the source sizes coincide with the sizes of maser spots (see, for example, [3]). The second group contains models in which compact maser spots arise in extended inverted sources, due to appropriate kinematics or geometry or both (see, e.g., [22]). As a rule, in a random velocity field such as a turbulent medium, the coherence path will be greater than the mean path along some directions; this can result in strong maser emission along such directions, provided that the corresponding transitions are inverted. The effect of the velocity field on the methanol maser emission was studied by Sobolev *et al.* [22], who showed that emission arising in a turbulent medium can have the appearance of individual spots. According to Slysh *et al.* [18] and Kalenskiĭ *et al.* [6], the 6_{-1}–5_0E and 5_{-1}–4_0E lines in Galactic molecular clouds are usually inverted; it is natural to suppose that the same is true for other class I maser lines. Without discounting the plausibility of group I models, we suggest that the coincidence of the radial velocities of the methanol masers and of the quiescent gas can readily be explained by group II models. The greater the line optical depth averaged over the cloud, the greater the optical depth along the maximum coherence path can be, and the stronger the maser emission can be. In giant molecular clouds, the intensity of line wings essentially always increases as the radial velocity approaches the velocity of the quiescent gas, testifying to an increasing average optical depth. Therefore, strong masers should arise at radial velocities characteristic of the quiescent gas.

Note that the 6_{-1}–5_0E line intensity toward IRAS 18265–1517 given by Slysh *et al.* [5] exceeds the intensity of this line obtained in our observations by a factor of more than 1.5. It is interesting to determine whether this is a consequence of calibration errors or of variability of the masers. Elucidation of this question will require regular observations of L379 IRS3 in the 6_{-1}–5_0E line and other class I maser lines.

6. CONCLUSIONS

(1) We have observed the star-forming region L379 IRS3 in the 6_{-1}–5_0E, 8_0–7_1A^+, and 2_K–1_K methanol lines, the (3–2) CS line, and the (2–1) $C^{34}S$ line. In the 6_{-1}–5_0E methanol and (3–2) CS lines, we observe both emission of the quiescent gas (at radial velocities 12–25 km/s) and emission of the high-velocity gas of the bipolar outflow (outside this interval). We have mapped the molecular cloud and bipolar outflow using the maximum-entropy method.

(2) We have analyzed the maps and compared them with the CO (2–1) and $C^{18}O$ (2–1) maps of Kelly and Macdonald [9]. The integrated (from 12 to 25 km/s) map of the molecular cloud in the (3–2) CS line essentially coincides with the map of the cloud in the (2–1) $C^{18}O$ line. However, the $C^{18}O$ line is narrower than the CS and CH_3OH lines, and the maps contain regions with appreciable CS and CH_3OH emission at 10–12 and 12–24 km/s, where there is virtually no $C^{18}O$ emission. These regions approximately coincide with the wings of the bipolar outflow; therefore, we suggest that the main contribution to the emission comes from the bipolar-outflow gas, which is probably moving in the tangential direction or whose motion has already stopped.

(3) The emission peaks in the bipolar-outflow maps ($V_{LSR} < 12$ km/s and $V_{LSR} > 25$ km/s) in CS and CH_3OH approximately coincide with the emission peaks in the bipolar-outflow map in the (2–1) CO line. However, the emission to the south of IRAS 18265–1517, which is prominent in the bipolar-outflow map in the (2–1) CO line, is almost completely absent from the bipolar-outflow maps in the CS and CH_3OH lines. This may be due to the fact

[5] Val'tts *et al.* [7] did not detect the narrow feature at 95 GHz due to insufficient spectral resolution.

that we have used a narrower radial-velocity range when mapping in the methanol and CS lines than for the CO maps (8.5–12 and 24–31 km/s *versus* −10 to 10 and 25–40 km/s, respectively).

(4) We have determined various parameters of the gas in L379 IRS3. We obtained a CS column density of 8×10^{14} cm^{-2} and an abundance of 4×10^{-9} for the molecular cloud. Using LVG modeling of the methanol emission, we estimate the density of gas in the cloud to be $(1–4) \times 10^5$ cm^{-3} and its kinetic temperature to be 20–45 K. The density of the high-velocity gas is constrained from above by values on the order of 10^5 cm^{-3}. For both the quiescent and high-velocity gas, the brightness of the methanol lines in models that reproduce the observed line-intensity ratios is much higher than the observed brightness. This suggests that either the gas is clumpy, diluting the emission, or the emission arises in a thin layer of gas.

(5) In the $8_0–7_1A^+$ line, we observed a narrow feature at 17.63 km/s against the background of a broader line. This narrow feature is probably a maser line.

ACKNOWLEDGMENTS

The authors are grateful to the staff of the Kitt Peak and Onsala Observatories for help with the observations and to I.E. Val'tts and G.M. Rudnitskiĭ for helpful discussions. This work was partially supported by the Russian Foundation for Basic Research (project no. 01-02-16902), the Radio Astronomy Science and Education Center (project 315), Astronomy grant 1.3.4.2, CRDF grant RP1-2392-MO-02, and a Nonstationary Processes grant.

REFERENCES

1. R. Bachiller and M. Pérez Gutiérrez, Astrophys. J. **487**, L93 (1997).
2. K. M. Menten, *Atoms, Ions and Molecules: New Results in Spectral Line Astrophysics*, Astron. Soc. Pac. Conf. Ser. **16**, 119 (1991).
3. R. L. Plambeck and K. M. Menten, Astrophys. J. **364**, 555 (1990).
4. S. V. Kalenskii, R. Bachiller, I. I. Berulis, *et al.*, Astron. Zh. **69**, 1002 (1992) [Sov. Astron. **36**, 517 (1992)].
5. V. I. Slysh, S. V. Kalenskii, I. E. Val'tts, *et al.*, Astrophys. J. **478**, L37 (1997).
6. S. V. Kalenskii, V. I. Slysh, I. E. Val'tts, *et al.*, Astron. Zh. **78**, 31 (2001) [Astron. Rep. **45**, 26 (2001)].
7. I. E. Val'tts, A. M. Dzura, S. V. Kalenskii, *et al.*, Astron. Zh. **72**, 22 (1995) [Astron. Rep. **39**, 18 (1995)].
8. B. Wilking and J. Blackwell, Astron. J. **100** (3), 758 (1990).
9. M. L. Kelly and G. H. Macdonald, Mon. Not. R. Astron. Soc. **282**, 401 (1996).
10. F. J. J. Lovas, *Catalog*, http://physics.nist.gov/cgi-bin/micro/table5/start.pl
11. G. M. Larionov, I. E. Val'tts, A. Winnberg, *et al.*, Astron. Astrophys., Suppl. Ser. **139**, 257 (1999).
12. V. Promyslov, *Advances in Soft Computing—Engineering Design and Manufacturing*, Ed. by R. Roy, T. Furuhashi, and P. K. Chawdhry (Springer-Verlag, London), p. 421.
13. G. H. Moriarty-Schieven, R. L. Snell, S. E. Ström, *et al.*, Astrophys. J. **319**, 742 (1987).
14. A. Dutrey, S. Yuilltedu, and R. Bachiller, Astron. Astrophys. **117**, 314 (1997).
15. L. G. Mundy, N. J. Evans, II, R. L. Snell, *et al.*, Astrophys. J. **306**, 670 (1996).
16. G. A. Blake, E. C. Sutton, C. R. Masson, and T. G. Phillips, Astrophys. J. **315**, 621 (1987).
17. S. V. Kalenskii, A. M. Dzura, R. Booth, *et al.*, Astron. Astrophys. **321**, 311 (1997).
18. V. I. Slysh, S. V. Kalenskii, I. E. Val'tts, *et al.*, Astrophys. J., Suppl. **123**, 515 (1999).
19. V. G. Promyslov, Astron. Zh. (in press).
20. L. Kogan and V. I. Slysh, Astrophys. J. **497**, 800 (1998).
21. V. I. Slysh, I. E. Val'tts, S. V. Kalenskii, and V. V. Golubev, Astron. Zh. **76**, 892 (1999) [Astron. Rep. **43**, 785 (1999)].
22. A. M. Sobolev, B. K. Wallin, and W. D. Watson, Astrophys. J. **498**, 763 (1998).

Translated by G. Rudnitskiĭ

Astronomy Reports, Vol. 47, No. 4, 2003, pp. 288–300. Translated from Astronomicheskiĭ Zhurnal, Vol. 80, No. 4, 2003, pp. 317–330.

Strömgren Zones of Type II Supernovae

A. V. Pynzar' and V. I. Shishov

Pushchino Radio Astronomy Observatory, Astro Space Center, Lebedev Physical Institute, Russian Academy of Sciences, Pushchino, Moscow region, 142290 Russia

Received August 10, 2001; in final form, August 21 2002

Abstract—The emission measures EM in the directions of supernova remnants and pulsars are considered as functions of their ages t. The resulting plot has a well-defined lower boundary, which can be approximated by the expression $EM_{min} \propto 1/t$. The quantity EM_{min} increases with decreasing age t and does not level off or reach a maximum until $t \cong 500$ yr. It is concluded that the bulk of the radiative energy that goes into ionizing and heating the interstellar gas is released at early stages of the supernova remnant's evolution. We suggest that most of the kinetic energy of the supernova shell is converted into thermal energy and radiated at remnant ages $t < 100$ yr, when the supernova shell, which is expanding at an enormous speed (about 10^4 km/s), overtakes the shell produced by the presupernova in the supergiant stage. We have estimated the ionization energy $E \cong 10^{51}$ erg, diameter $L \cong 60$ pc, and electron density $N_e \cong 7\ \mathrm{cm}^{-3}$ of the HII regions around the supernovae (the supernova Strömgren zones). A list of objects that can be reliably identified as Strömgren zones of type II supernovae is presented. The plot of pulsar pulse broadening τ as a function of the pulsar age t also has a well-defined lower boundary, for which $\tau \propto t^{-2}$ when $t \geq 1000$ yr. This suggests that turbulence develops during the first thousand years after the supernova outburst. It is also concluded that turbulence plays an important role in the formation and evolution of the Strömgren zones of type II supernovae. © *2003 MAIK "Nauka/Interperiodica".*

1. INTRODUCTION

Turbulent plasma is an important component of the interstellar medium and is observed in the directions of all known pulsars. The plasma parameters that can be measured are the dispersion measure DM, emission measure EM, and a number of parameters characterizing the modulation of the radio emission by plasma inhomogeneities. The most extensive data sets have been obtained for τ, the pulse broadening due to scattering in the turbulent medium. The quantity τ is proportional to the square of the dispersion of the electron-density fluctuations $\langle(\Delta N_e)\rangle$. A statistical analysis of the distribution of these quantities in the Galaxy shows that they are interrelated and correspond to the same objects. It has also been shown that turbulent plasma clouds can be divided into two types, A and B [1–3]. Type A clouds are distributed in the space between the spiral arms of the Galaxy, while type B clouds are distributed in the spiral arms. In turn, type B clouds are classified into two subtypes, BI and BII [3]. Type BI clouds are distributed in the spiral arms more uniformly, while type BII clouds are concentrated in compact regions. However, in spite of the large amount of observational data, the mechanisms generating the turbulence in the interstellar plasma remain poorly understood. The sources of turbulence and ionization energy have not been reliably identified with known astrophysical objects. Solving these problems requires new, more accurate measurements of the turbulence spectra and further attempts to associate clouds of turbulent plasma with known astrophysical objects.

In [4], we reported the first observational evidence for the association of some regions of turbulent interstellar plasma with supernova outbursts. We studied the emission measure EM in the direction of a given pulsar as a function of the pulsar age t. The EM–t diagram clearly indicates the existence of a lower boundary $EM_{min} \propto 1/t$ in the range $10\,000\ \mathrm{yr} < t < 1\,000\,000$ yr [4]. According to [4], the dependence of EM_{min} on t suggests that the HII zones around the pulsars near the lower boundary of the EM–t diagram originated either during the supernova explosion that gave birth to the pulsar or during the evolution of the supernova remnant. Unfortunately, there are few young pulsars with ages under 10 000 yr, and the statistics for these ages are insufficient to determine when the ionization energy was released. If the HII zone forms during the early stages in the evolution of the supernova shell or during the supernova explosion, $EM_{min}(t)$ should be constant or should grow at young pulsar ages and then decrease with age. If, however, the HII region forms when the supernova-remnant shell radiates, $EM_{min}(t)$ should peak at a pulsar age of several times 10^4 yr.

1063-7729/03/4704-0288$24.00

To extend the statistics for young pulsar ages, we supplemented the pulsar data presented in [4] with analogous data for supernova outburst. We assumed that pulsars and supernova remnants originate simultaneously, so that the HII regions observed around supernova remnants and pulsars are the same objects. Here, we study the EMs in the directions toward supernova remnants as a function of the remnant ages and compare the resulting plot with the corresponding dependence for pulsars.

2. RELATIONSHIP BETWEEN THE EMISSION MEASURE TOWARD A SUPERNOVA REMNANT AND THE REMNANT'S AGE

We have compiled a list of supernova remnants for which age estimates are available from the literature [5–8] and have determined the EMs toward these remnants.

We derived the EMs using the measured intensities of the Galactic background at 5 and 10 GHz [9–12], in the Hα line [13–17], at 60 μm [18], and in the hydrogen recombination line H166α [19–21]. In addition, for crude EM estimates, we used the data of the photographic Hα sky survey [22] combined with the latitudinal dependence of the EM based on regions for which Hα [13–17] and IR [18] measurements of the background intensity are available.

We calculated the EM from the measured background brightness temperatures, T_b, based on the well-known relationship [23]

$$T_\mathrm{b}(\mathrm{K}) = 3.4\times10^3\left(\frac{1\ \mathrm{GHz}}{\nu}\right)^{2.1}\left(\frac{10^4\ \mathrm{K}}{T_e}\right)^{0.35} \times\left(\frac{\mathrm{EM}}{10^6\ \mathrm{pc\ cm^{-6}}}\right), \quad (1)$$

where the frequency ν is in GHz, the electron temperature of the ionized gas T_e is in K, and the EM of the gas is in pc cm^{-6}. We used this formula to calculate the EM from the measured background intensities at high radio frequencies $\nu = 5$–10 GHz and in the IR, where the diffuse interstellar medium is optically thin. We distinguished the thermal component of the background brightness temperature at 5–10 GHz applying the technique described in [24, 25].

To determine the EM from the measured intensities of the hydrogen recombination line H166α, we used the following expression for the power P emitted in the line [26]:

$$\mathrm{EM} = 2.25\times10^3 T_e^{1.5} n^{-3} b^{-1} P\ \mathrm{pc/cm^6}, \quad (2)$$

where $P(\mathrm{K\,kHz}) = \int T_L(\nu)d\nu$ is the integral of the line intensity over the frequency, $T_L(\mathrm{K})$ is the brightness temperature of the line, $n = 166$ is the principal quantum number, and b is a coefficient characterizing the departure from local thermodynamic equilibrium (assumed here to be unity) [26, 27].

The EM was determined from the measured background intensities in the Hα line in accordance with the formula [15, 16]

$$\mathrm{EM} = 2.75 I_\alpha\left(\frac{T_e}{10000}\right)^{0.9}\exp(2.2E_{B-V})\ \mathrm{pc/cm^6}, \quad (3)$$

where I_α is the Hα line intensity measured in Rayleighs [15]. The term $\exp(2.2E_{B-V})$ corrects the line intensity for dust absorption, and E_{B-V} is the color excess in magnitudes. The dust-absorption data were taken from [28].

Observations of recombination lines suggest that the electron temperature increases with distance from the Galactic center [29]. For this reason, we used the value $T_e = 6000$ K [29] when calculating the emission measure from radio [9–12, 19–21] and IR [18] data, which mainly refer to the inner part of the Galaxy (longitudes $l < 90°$ and $l > 270°$), and the value $T_e = 8000$ K [15, 16] in calculations based on optical data for near-solar regions.

Data for supernova-remnant ages and EMs in the directions toward the regions of these remnants are given in Table 1, whose columns contain (1) the Galactic coordinates (l, b) of the supernova remnants, (2) the EMs in their neighborhoods, (3) the ages of the remnants, and (4) references to the EMs or Galactic-background intensities used to calculate the EMs. Some emission measures in Table 1 may differ from the true EMs by a factor of two. This is due to the fact that large variations in the electron temperature can occur along lines of sight for which the EMs are large (EM > 1000 pc/cm^6); moreover, background-intensity measurements are missing for some directions with small EMs (EM < 100 pc/cm^6, at Galactic longitudes $240° - 360°$ and latitudes $b > 1°$–$3°$), and we estimated the EMs in these cases using Hα photographs of the sky [22], via comparison with regions of the sky for which Hα background-intensity measurements are available [13–17].

The data of Table 1 are also presented in Fig. 1, which plots the EMs as a function of the ages of the supernova remnants, t. However, not all supernova-remnant data can be compared with the pulsar data given in Fig. 2 of our study [4]. It is known that pulsars are related to type II supernova outbursts [7, 31] and that young pulsars ($t < 10^6$ yr), like type II supernova remnants, are located near the Galactic plane.

The remnants are associated with both type I and type II supernovae. To isolate the remnants of type II

Table 1. EMs toward supernova remnants and remnant ages t

l, b, deg	EM, pc/cm^6	t, yr	References for EM data	l, b, deg	EM, pc/cm^6	t, yr	References for EM data
$4.5 + 6.8$	70	397	13, 22	$132.7 + 1.3$	70	27500	18, 22
$5.4 - 1.2$	800	2500	9, 12	$184.6 - 5.8$	75	947	14, 16
$6.4 - 0.1$	2000	9200	11, 20	$189.1 + 3.0$	80	6000	13, 14
$7.7 - 3.7$	160	2000	18	$263.9 - 3.3$	500	13000	17
$11.2 - 0.3$	2500	1000	9, 11, 12	$290.1 - 0.8$	2200	10000	10, 18
$12.0 - 0.1$	3000	6400	11, 20	$291.0 - 0.1$	1500	6500	10, 18
$15.9 + 0.2$	1500	4900	9, 20	$292.0 + 1.8$	160	1300	18
$18.8 + 0.3$	2500	4000	11	$296.5 + 10.0$	30	5000	14–17, 22
$21.5 - 0.9$	1500	500	9, 11, 12	$298.5 - 0.3$	1000	3100	18, 21
$21.8 - 0.6$	1500	6400	9, 11, 18	$304.6 + 0.1$	1500	4000	10, 18
$22.7 - 0.2$	4000	10000	11, 20	$308.8 - 0.1$	2500	4800	10, 18, 21
$23.3 - 0.3$	10000	6800	11, 20	$311.5 - 0.3$	3500	4200	10, 18, 21
$27.4 + 0.0$	5000	6300	11, 20	$315.4 - 2.3$	150	2000	18
$29.7 - 0.3$	4000	660	11, 18	$316.3 - 0.0$	1500	700	18
$31.9 + 0.0$	4000	13000	11, 20	$320.4 - 1.2$	1000	15000	10, 18
$33.6 + 0.1$	3500	6000	11, 18, 20	$326.3 - 1.8$	180	3000	18
$34.7 - 0.4$	1400	13000	9, 12, 18	$327.1 - 1.1$	1500	10000	10, 18
$39.2 - 0.3$	700	2500	18	$327.4 + 0.4$	3000	10000	10, 18
$39.7 - 2.0$	160	100000	18	$327.6 + 14.6$	50	995	14–17, 22
$41.1 - 0.3$	800	2000	18	$328.4 + 0.2$	3000	1500	10, 18, 21
$43.3 - 0.2$	2200	1500	9, 12, 18	$332.4 + 0.1$	8000	6300	10, 21
$49.2 - 0.7$	700	18000	9, 11, 18	$332.4 - 0.4$	8000	2000	10, 21
$53.6 - 2.2$	180	21000	18	$337.0 - 0.1$	7000	3600	10, 21
$69.0 + 2.7$	140	10000	18	$337.2 - 0.7$	2000	5900	10, 18
$74.0 - 8.5$	50	20000	13, 18, 22	$337.8 - 0.1$	7000	6200	10, 21
$74.9 + 1.2$	500	4600	18	$338.5 + 0.1$	7000	6000	10, 21
$78.1 + 1.8$	3000	2600	18	$340.6 + 0.3$	500	5200	18, 21
$82.2 + 5.3$	500	24000	18	$341.9 - 0.3$	1450	7000	18, 21
$89.0 + 4.7$	60	7800	13, 18, 22	$346.6 - 0.2$	1200	6200	10, 21
$89.1 + 3.0$	40	6000	13, 18, 22	$348.5 + 0.1$	3000	1300	10, 21
$93.3 + 6.9$	25	1500	13, 22	$348.7 + 0.3$	2000	1500	10, 18, 21
$109.1 - 1.0$	400	13000	18, 22	$349.7 + 0.2$	3000	260	10, 21
$111.7 - 2.1$	124	336	30	$350.0 - 2.0$	180	8000	18
$116.9 + 0.2$	100	17000	18, 22	$350.1 - 0.3$	2000	2700	10, 18, 21
$119.5 + 10.2$	30	8000	13, 22	$351.2 + 0.1$	2000	6700	10, 18, 21
$120.1 + 1.4$	100	429	13, 18, 22	$352.7 - 0.1$	3000	6200	10, 21
$127.1 + 0.5$	60	18000	18, 22	$357.7 - 0.1$	1000	1000	14, 18, 20
$130.7 + 3.1$	50	820	18, 22				

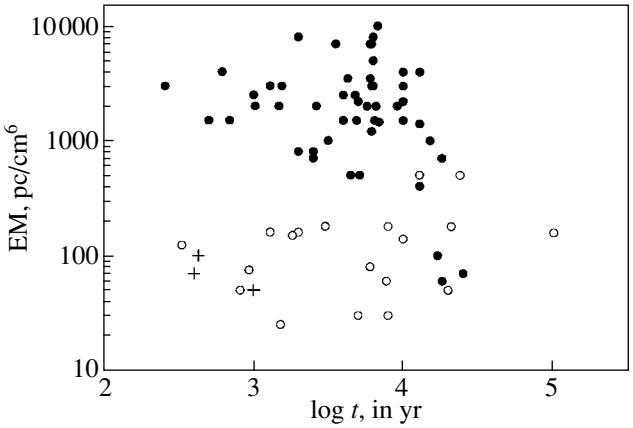

Fig. 1. Relationship between the emission measures EM of the Galactic background in the directions toward supernova remnants and the remnant ages t. The solid circles show low-latitude remnants ($b < 1.4°$), open circles high-latitude remnants, and crosses type I historical remnants—SN 1572 (Tycho Brahe's supernova), SN 1604 (Kepler's supernova), and SN 1006.

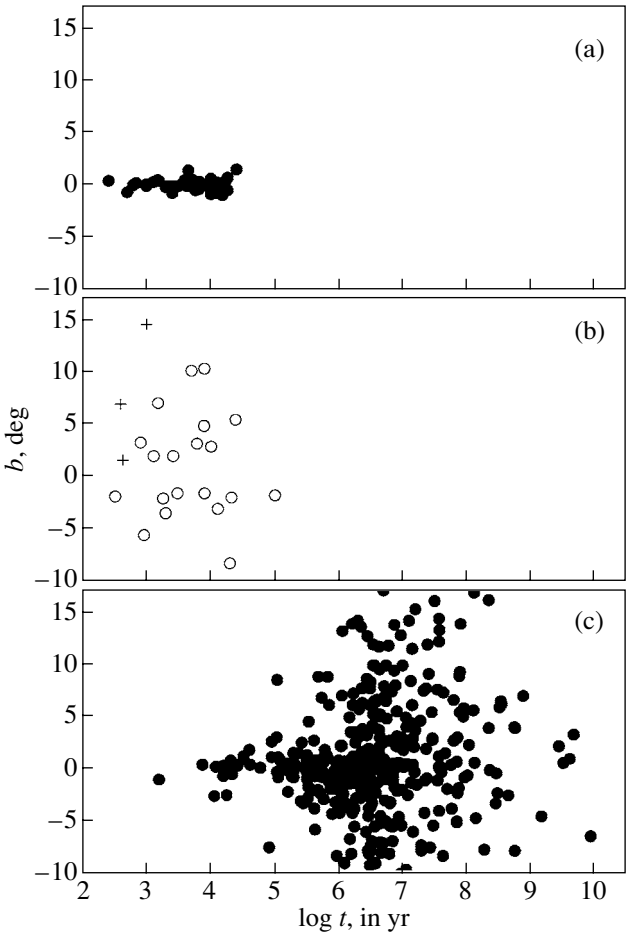

Fig. 2. Relationship between Galactic latitude and age for (a) type II supernova remnants, (b) type I supernova remnants (crosses indicate the data for historical type I remnants—SN 1572 (Tycho Brahe's supernova), SN 1604 (Kepler's supernova), and SN 1006), and (c) pulsars.

supernovae, which should be done for further comparisons between the data for remnants and pulsars, we divided the supernova remnants into low- and high-latitude remnants. The open circles in Fig. 1 indicate data for remnants located at high Galactic latitudes, $b > 1.4°$, while the solid circles represent data for remnants at Galactic latitudes $b < 1.4°$. The boundary $b = 1.4°$ was chosen so that no remnant related to a historical type I supernova (SN 1572 of Tycho Brahe, SN 1604 of Kepler, and SN 1006) was among the objects whose data will be compared with the pulsar data. We can readily see that the points in the EM(t) diagram separate into two groups, or branches. The supernova remnants in the upper and lower branches display EMs on the order of several thousand pc/cm^6 and several hundred pc/cm^6, respectively. There is a lacuna between these branches. The upper branch is a good continuation of the pulsar data into the region of young ages, while the data in the lower branch do not agree well with the pulsar data. It is most likely that the upper branch is formed by type II supernova remnants, which originate during the explosions of young, massive stars of early spectral types, which also give rise to pulsars [7, 31]. The latitudinal distributions of the supernova remnants corresponding to the upper and lower branches of the diagram in Fig. 1 are shown in Fig. 2 together with the distribution of pulsars. We can clearly see that pulsars with ages less than 30 000 yr (the upper boundary for the supernova-remnant ages) are concentrated near the Galactic plane and that their distribution corresponds to that of objects on the upper branch, while the distribution of the lower-branch remnants disagrees substantially with the latitudinal distribution of young pulsars. Therefore, when composing a diagram including data for both pulsars and supernova remnants, it is quite reasonable to include only data for low-latitude supernova remnants, which are located in the upper branch of the diagram in Fig. 1.

3. DEPENDENCE OF THE EM TOWARD A PULSAR OR SUPERNOVA REMNANT ON THE TIME SINCE THE SUPERNOVA OUTBURST

Figure 3 shows the dependence of the EM toward a given pulsar or supernova remnant in the upper branch of the diagram in Fig. 1 on the age of the object. All the pulsar data used here were taken from [32, 33]. The data on the EMs toward the pulsars were obtained as described above, from the same publications and using the same techniques as for the supernova remnants; they correspond to the data presented in [4]. Figure 3 does not contain data for the Crab pulsar, which is a unique object that differs from other pulsars in many respects. We can see that the positions of the points in Fig. 3 corresponding to pulsars and supernova remnants agree well. The age-dependent lower boundary of the collection of points $\mathrm{EM}_{\min}$ is well defined in this figure. The $\mathrm{EM}_{\min}(t)$ relation for supernova remnants smoothly continues the corresponding dependence for pulsars into the region of young ages; this dependence can be approximated by the formula

$$\mathrm{EM}_{\min} = EM_{\min,0}\left(\frac{t_0}{t}\right)^{\gamma}, \quad t \geq 1000\ \mathrm{yr}, \qquad (4)$$

$$t_0 = 1000\ \mathrm{yr}, \quad \mathrm{EM}_{\min,0} \approx 10^3\ \mathrm{pc/cm^3}, \quad \gamma \cong 1.$$

The approximation (4) is fairly stable with regard to the sample used. If we choose for each time interval $\Delta(\log t)$ the minimum EM and formally fit a power law to the resulting sample, the resulting coefficients of the $\mathrm{EM}_{\min}(t)$ dependences for various time intervals $\Delta(\log t) = 1,\ 0.5,\ 0.25$ vary within 30% for $\mathrm{EM}_{\min,0}$ and within 20% for γ. The standard errors in the coefficients obtained when fitting the dependence (1) for each sample are smaller than those indicated above.

The diagram in Fig. 3 clearly demonstrates that $\mathrm{EM}_{\min}$ increases with decreasing age and does not reach a maximum or level off until $t \cong 500$ yr. This means that the bulk of the radiative energy going into ionizing and heating the interstellar gas is released at early stages of the supernova remnant's evolution, at $t < 1000$ yrs. This energy cannot be released during the supernova explosion, since the cooling of the shell due to its spherically symmetric expansion is much faster than its energy loss due to radiation, and most of the shell's energy is transformed into kinetic energy. At the same time, our observational data indicate that the source of ionization energy cannot be radiation at a late evolutionary stage of the supernova shell, $t \cong 10\,000$ yr [7]. These observational data can be explained if we assume that the transformation of the bulk of the supernova shell's kinetic energy into thermal energy and the radiation of this energy take place at remnant ages of <100 yr, when the supernova shell, which is expanding at an enormous speed ($\cong 10^4$ km/s), overtakes the shell formed by the presupernova in the red- or blue-supergiant stage. When these two shells collide, the bulk of the explosion's energy is released as hot radiation, which ionizes the ambient gas. Such an event is expected to occur soon for supernova 1987 in the Large Magellanic Cloud [34, 35]. Within a few years, these shells will collide, and it will be possible to determine the energy released in this collision and the wavelength range of this energy.

The low-mass stars from which type I supernovae, the Crab Nebula, and 3C 58 originated do not have

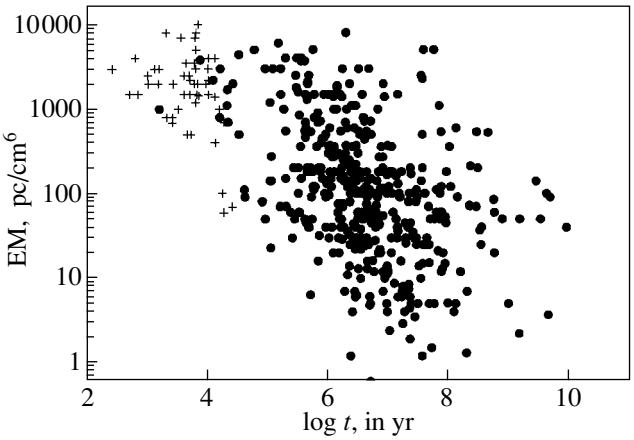

Fig. 3. Emission measure EM toward pulsars (circles) and supernova remnants located in the upper branch of the diagram in Fig. 1 (crosses) as a function of age t.

such powerful and nearby shells. The conversion of the kinetic energy of their shells to ionizing radiation probably occurs later, at $t \cong 10^4$ yr—during the sweeping up of the distributed interstellar gas and the corresponding cooling of the gas to temperatures of the order of 10^6 K, at which the energy of the gas is efficiently lost via radiation.

Note that, in principle, there is another way to explain the evolution curve (4): the migration of pulsars to high latitudes with age, so that the curve describes the latitudinal distribution of the emission measure. However, the migration of a pulsar by 100 pc takes of the order of 1 Myr, so that the curve (4) cannot be explained using latitudinal displacements of the pulsars on shorter times. This is confirmed by the latitudinal distribution of pulsars as a function of their age (Fig. 2c). We have separately constructed the age dependence of the latitudinal distribution of the sample of pulsars located near the delimiting curve (4) in Fig. 3. Figure 4a clearly shows that the mean latitude of the pulsars does not depend on their ages if these ages are under 300 000 yr. Thus, the relation (4) reflects the behavior of the electron density N_e as a function of the time t since the supernova outburst.

To analyze possible selection effects related to the longitudinal distribution of pulsars and supernova remnants, we divided the points in Fig. 3 into two subsets. The data for pulsars and supernova remnants in the longitude range $-50° < l < +50°$ are marked with open circles. The data for objects in the longitude range $50° < l < 310°$ are marked with solid circles. These data are shown in Fig. 4b. Both subsets exhibit similar distributions, with clear-cut lower boundaries. The modest systematic displacement of the subset shown by the open circles toward larger EMs can be explained quite naturally as being due to the systematic increase in the gas density with decreasing distance from the Galactic center.

4. PARAMETERS OF THE HII ZONE AROUND A SUPERNOVA REMNANT OR PULSAR AS FUNCTIONS OF THE OBJECT'S AGE

The evolution of the parameters of the ionized gas surrounding the supernova remnant can be traced by comparing the dependences of the EM and DM on the remnant age. Figure 5 shows the DM as a function of the time t elapsed since the supernova outburst. The circles in this figure represent data for pulsars located at or near the lower boundary $\mathrm{EM_{min}}$ in Fig. 3; t is taken to be the age of the pulsar. The crosses mark DMs obtained for pulsars situated within 1° of supernova remnants. In this case, the age of the supernova remnant located near the pulsar is used for t. The decrease in the DM with increasing t in the interval 10^3–3×10^4 yr is quite obvious. The DMs in this interval are determined by the HII zones formed after the supernova outbursts. Later, in the interval 3×10^4–3×10^6 yr, the DM levels off at a value determined by the background medium. Further, the DM again decreases, due to the random distribution of the pulsars along the line of sight. This means that only pulsars with ages in excess of 3 Myr are present in the solar neighborhood. We also emphasize that the existence of a sharp lower boundary at ages less that 3 Myr suggests that young pulsars are concentrated in compact regions of dense gas. On the whole, the time dependence of the lower boundary in the interval 10^3–3×10^6 yr can be approximated by the relationship

$$\mathrm{DM_{min}} = \mathrm{DM_{SN}} + \mathrm{DM_{ground}}, \qquad (5)$$

$$\mathrm{DM_{SN,min}} \cong \frac{2 \times 10^2}{(t_0/t)^{1/2}}\ \mathrm{pc/cm^3},$$

$$\mathrm{DM_{ground}} \cong 30\ \mathrm{pc/cm^3}.$$

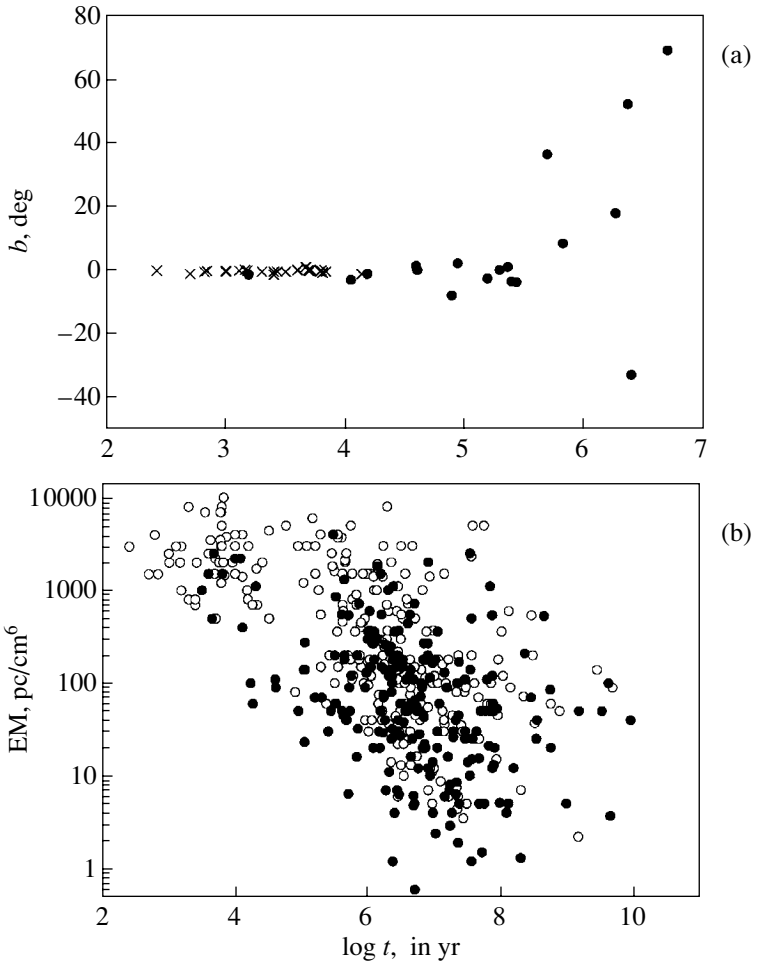

Fig. 4. (a) Relationship between Galactic latitude b and age t for the sample of pulsars (circles) and supernova remnants (crosses) situated near the delimiting curve (1) in Fig. 3; (b) EMs toward pulsars and supernova remnants as functions of their age for two samples—objects whose longitudes are within 50° of the Galactic center (open circles) and whose longitudes exceed 50° (solid circles).

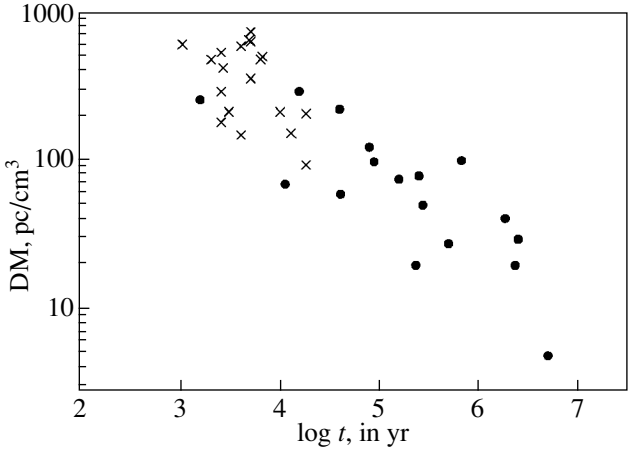

Fig. 5. Relationship between the DM and the age of the supernova Strömgren zone t for pulsars located near the lower boundary of the distribution in Fig. 3 (circles). The crosses mark DMs obtained for pulsars that are less than 1° from the centers of supernova remnants located near the lower boundary in Fig. 3. In this case, the age of the supernova remnant is adopted for t.

The dispersion measure is temperature-independent and can be written in the form

$$\mathrm{DM} = \langle N_e \rangle L. \tag{6}$$

The emission measure derived from observations depends on the assumed temperature. Usually, $T \simeq T_1 = 10\,000$ K is adopted for measurements, and we used similar values when constructing Fig. 1. We denote the corresponding emission measure EM_1. The true EM can be expressed in terms of EM_1 as follows:

$$\mathrm{EM} = \mathrm{EM}_1 \left(\frac{T}{T_1}\right)^{\alpha}, \tag{7}$$
$$T_1 = 10000\ \mathrm{K}, \quad \alpha = 0.35,$$

where the exponent α depends on the measurement procedure. If the EM is determined using high-frequency radio data, $\alpha = 0.35$ (1). We will use this value for α, since the EMs for the young pulsars and supernova remnants determining $\mathrm{EM}_{\min}$ were obtained from high-frequency radio data. The EM can be represented in the form

$$\mathrm{EM} = \langle N_e^2 \rangle L = \mathrm{EM}_1 \left(\frac{T}{T_1}\right)^{\alpha}. \tag{8}$$

We introduce the relative level for the electron-density fluctuations

$$\Delta^2 = \frac{\langle N_e^2 \rangle - \langle N_e \rangle^2}{\langle N_e \rangle^2}, \tag{9}$$

to obtain

$$\langle N_e \rangle^2 L = \frac{\mathrm{EM}}{1+\Delta^2} = \frac{\mathrm{EM}_1 \left(\frac{T}{T_1}\right)^{\alpha}}{1+\Delta^2}. \tag{10}$$

Comparing $\mathrm{EM}_{\min}$ and $\mathrm{DM}_{\mathrm{SN,min}}$, we can determine the density N_e and radius of the region of ionized gas R:

$$\langle N_e \rangle = \frac{\mathrm{EM}_{\min}}{2(1+\Delta^2)\mathrm{DM}_{\mathrm{SN,min}}} \tag{11}$$
$$\simeq \frac{2.5 \left(\frac{T}{T_1}\right)^{\alpha}}{(1+\Delta^2)\left(\frac{t}{t_0}\right)^{1/2}}\ \mathrm{cm}^{-3},$$
$$R = \frac{2(\mathrm{DM}_{\mathrm{SN},min})^2(1+\Delta^2)}{EM_{\min}}$$
$$\simeq \mathrm{Const} \simeq \frac{80(1+\Delta^2)}{(T/T_1)^{\alpha}}\ \mathrm{pc}.$$

Equation (11) takes into account the fact that the EM probes the entire region, being determined by the diameter $2R$, while the DM is determined by the radius R, since the pulsar is situated near the center of the region. Preliminary maps of the distribution of thermal emission near the pulsars and supernova remnants shows that the observed angular size (diameter) of the Strömgren zone is typically of order 1°; at a distance of $r = 3$ kpc, this yields

$$R \simeq 25\ \mathrm{pc}. \tag{12}$$

This R value can be brought into agreement with the estimate (11) if

$$T \simeq 30T_1 \simeq 300\,000\ \mathrm{K}. \tag{13}$$

The N_e and R estimates can be used to estimate E, the total ionization energy of all the gas contained in the HII region. The total number of electrons in the Strömgren zone at $t = t_0 = 1000$ yr is

$$N_{\mathrm{total}} = (\pi/6)\langle N_e \rangle L^3_{|t_o} = \frac{4\pi}{3}(3\times 10^{18})^3 R^2 \mathrm{DM} \tag{14}$$
$$\simeq 1.4\times 10^{62}(1+\Delta^2)^2 \left(\frac{T}{T_1}\right)^{2\alpha}\ \text{particles}.$$

The total energy of the Strömgren zone consists of the ionization energy and the thermal energy of the particles. Assuming equal numbers of ions and electrons, we obtain

$$E \simeq 3.1\times 10^{51}\left[1+\frac{3}{2}(1+x)\frac{T}{T_2}\right]\frac{1+\Delta^2}{\left(\frac{T}{T_1}\right)^{2\alpha}\left(\frac{t}{t_0}\right)^{1/2}}, \tag{15}$$

$$T_2 = \frac{e_{\mathrm{ioniz}}}{k} = 1.6\times 10^5\ \mathrm{K}. \tag{16}$$

Here, T is the electron temperature, $T_i = xT$ is the ion temperature, e_{ioniz} is the ionization energy of the hydrogen atom, and k is the Boltzmann constant. Our estimate for the total energy of the Strömgren zone depends on the temperature T. It first decreases, then increases with T. The energy E is minimum when

$$T = T_{\min} \simeq \frac{1.56T_2}{1+x} \simeq \frac{250\,000K}{1+x}. \tag{17}$$

The estimated energy of the Strömgren zone reaches its absolute minimum when $T_i = 0$ ($x = 0$):

$$\mathrm{E}_{\min} \simeq 1.06\times 10^{51}\frac{1+\Delta^2}{(t/t_0)^{1/2}}, \quad x = 0. \tag{18}$$

We obtain when $T_i = T_e (x = 1)$

$$\mathrm{E}_{\min} \simeq 1.72\times 10^{51}\frac{1+\Delta^2}{(t/t_0)^{1/2}}, \quad x = 1. \tag{19}$$

Note that the estimated energy of the Strömgren zone depends strongly on the temperature T only if $T < T_2$. When $T > T_2$, this energy is close to $\mathrm{E}_{\min}$.

The estimates (18) and (19) for the Strömgren zone's energy at $t = t_0 = 1000$ yr are close to the limiting allowable estimate for the kinetic energy of the supernova shell [7]; for this reason, we cannot assume a highly nonuniform distribution of the electron density and a high filling factor: $\Delta^2 < 1$. On the other hand, the presence of strong turbulence precludes too small values of Δ. These two requirements are compatible provided

$$\Delta \simeq (0.3 - 0.7). \tag{20}$$

We assume for the parameters of the medium

$$T = 250000 \text{ K}, \quad t = t_0 = 1000 \text{ yr},$$
$$x = 0, \quad \Delta = 0.3$$

and, using (11), (15), and (18), we obtain

$$L = 2R = 56 \text{ pc}, \quad N_e = 7.1 \text{ cm}^{-3},$$
$$E = \mathrm{E}_{\min} = 1.16 \times 10^{51} \text{ erg}.$$

5. TURBULENCE IN THE STRÖMGREN ZONE

Information on the turbulence in the Strömgren zones can be inferred from analyses of observed scintillation and scattering effects [36]. These data are much scarcer than data on the EM and DM. The most complete data series have been obtained for measurements of the broadening of pulsar pulses scattered in the turbulent medium, τ [32, 33]. Figure 6 shows data for τ for pulsars located in the lower bounding zone of Fig. 3, reduced to the frequency $f = 300$ MHz, as a function of their ages. Note the strong decrease in τ with increasing age t. On the whole, this dependence can be approximated by the relationship

$$\tau \cong 10 \left(\frac{t_0}{t}\right)^2 \text{ s}. \tag{21}$$

The pulse broadening τ is related to the scattering angle of the plane wave, θ, by the expression [36]

$$\tau = \frac{GR\theta^2}{2c}, \quad G = \frac{2}{\pi^2} \cong 0.2, \tag{22}$$

where c is the speed of light and G is a numerical factor. In (22), G is given for the case of signal propagation in a statistically uniform sphere with distances from the observer r much greater than the radius of the sphere R, $r \gg R$. In addition, it was assumed that the scattering is produced by inhomogeneities with a type II turbulence spectrum, as described in [36], i.e., with a power-law turbulence spectrum and an inner scale $l > \frac{1}{k\theta}$.

The quantities τ and θ^2 can be expressed in terms of the turbulent-spectrum parameters $\Phi_{N_e}(q)$, where q is the spatial frequency. We assume $\Phi_{N_e}(q)$ has the form of a von Kármán spectrum [37]

$$\Phi_{N_e}(q) = \frac{K(n)\langle(\delta N_e)\rangle L_0^3}{(1 + q^2 L_0^2)^{n/2}}, \tag{23}$$
$$K(n) = \frac{\Gamma(n/2)}{\Gamma((n-3)/2)\pi\sqrt{\pi}}$$

where $\langle(\delta N_e)\rangle$ is the mean square of the electron-density fluctuations and L and l are the outer and inner turbulence scales, respectively. We substitute the spectrum (23) into the expression determining the phase-fluctuation structure function for $\rho \ll L$ [38],

$$D_S(\rho) = (k\theta\rho)^{n-2} = 4\pi(\lambda r_e)^2 \tag{24}$$
$$\times \int d^2\mathbf{q}_\perp [1 - \cos(\mathbf{q}_\perp \rho)] \Phi_{N_e}(\mathbf{q}_\perp, q_\parallel)$$

to obtain the following expression for θ:

$$(k\theta)^{n-2} = A(n)(\lambda r_e)^2 \langle(\delta N_e)^2\rangle R L^{-(n-3)}, \tag{25}$$
$$A(n) = 2^{4-n}(n-3)\frac{\Gamma((n-2)/2)}{(n-1)(n-2)\Gamma((n-1)/2)}.$$

Substituting (25) into the expression for τ yields

$$\tau \cong \tau_0 \frac{R}{R_0}\left[\delta^2 \frac{\mathrm{EM}}{\mathrm{EM}_0}\frac{R}{R_0}\frac{L}{L_0}^{-(n-3)}\right]^{2/(n-2)}, \tag{26}$$
$$\tau_0 \cong G R_0 [A(n)\mathrm{EM}_0 R_0 L_0^{-(n-3)}]^{2/(n-2)} \text{ s},$$
$$\mathrm{EM}_0 = 10^3 \text{ pc/cm}^6,$$
$$R_0 = 30 \text{ pc},$$
$$L_0 = 10^{15} \text{ cm}.$$

In (26), the parameter

$$\delta^2 = \frac{\langle(\Delta N_e)^2\rangle}{\langle N_e^2\rangle} \tag{27}$$

denotes the level of the turbulent fluctuations.

Comparing the time dependences of τ (21) and the EM (4) yields

$$\delta^2 = \delta_0^2 \left(\frac{t_0}{t}\right)^{n-3}. \tag{28}$$

Thus, the level of the turbulent fluctuations decreases with time.

Equation (26) can be used to estimate the outer scale of the turbulence. Assuming $\tau = 10$ s and $\delta = 1$, we find for $t = t_0 = 1000$ yr and $n = 11/3$ that

$$L \cong 10^{-3} L_0 = 10^{12} \text{ cm}. \tag{29}$$

This L is too small to be associated with the sizes of neutral-gas clouds originating from the thermal instability of the cooling gas [23], whose expansion in the presence of rapid ionization and heating could produce the observed turbulence. This L also implies

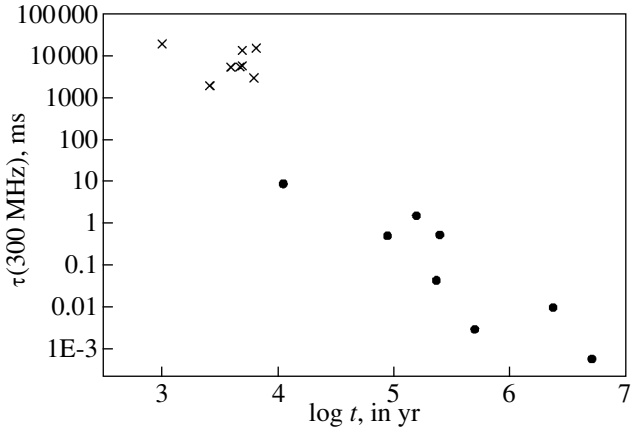

Fig. 6. Relationship between the broadening of pulsar pulses scattered by the turbulent medium, τ, and the age of the supernova's Strömgren zone, t. The circles show data for pulsars located near the lower boundary in Fig. 3, and the crosses, data for pulsars located less than 1° from the centers of supernova remnants situated near the lower boundary in Fig. 3. In the latter case, the age of the supernova remnant is adopted for t.

a faster decay of the turbulence. In particular, the characteristic time for the nonlinear dissipation of the turbulence in the case of three-wave processes is

$$t_{\rm turb} = \frac{1}{\gamma} \cong \frac{L}{v_s} \leq 10^6 s. \qquad (30)$$

Here, γ is the decay rate and v_s is the speed of sound. The numerical estimate (30) was obtained for $\delta = 1$ and $v_s = 10^6$ cm/s.

However, the estimate of L depends strongly on the exponent n. For instance, we have for $n = 3.5$

$$L \cong 10 L_0 = 10^{16} \text{cm}. \qquad (31)$$

This L is fairly close to the expected characteristic sizes of neutral-hydrogen clouds present in the interstellar gas before the supernova outburst. Using this estimate of L results in the following, more realistic, estimate of $t_{\rm turb}$:

$$t_{\rm turb} \leq 300 \text{ yr}. \qquad (32)$$

The question of the type of turbulence spectrum and the value of the exponent n at early evolutionary stages of the Strömgren zone remains unresolved.

6. DISCUSSION

Thus, the data for Strömgren zones that can be detected using EMs determined in the neighborhoods of type II supernova remnants agree well with the data for EMs determined in the neighborhoods of young pulsars, making it possible to study in greater detail variations of the emission measure with time since the supernova outburst. The summarized data indicate that the bulk of the ionizing-radiation energy is released at an early stage of the supernova shell's evolution, less than 300 yr after the supernova outburst. This energy release may be associated with the collision between the supernova shell and the relic shell of the supergiant precursor to the supernova. Such a supergiant shell is observed near SN 1987 in the Large Magellanic Cloud, and a collision between the supernova and supergiant shells is expected in the near future [34, 35]. As the two shells collide, the bulk of the kinetic energy of the supernova shell should be converted into thermal energy and subsequently into hot ionizing radiation. The collision results in a very high gas temperature, on the order of several hundred million Kelvin, raising the question of how such a gas can lose energy via radiation. For instance, if we assume that a shell energy $E = 10^{51}$ erg is converted into the thermal energy of two colliding shells with a total mass of $10 M_\odot$, the corresponding temperature of the medium for a uniform energy distribution is $T = 5 \times 10^8$ K. If the supergiant-shell radius is $R = 0.3$ pc, we obtain a particle density of the order of $N = 10^4$ cm^{-3}. Assuming these temperature and density values and using tabulated values for the efficiency of radiative cooling $\lambda(T) = 10^{-23}$ erg cm^3 s^{-1} (see, e.g., [23]) leads to a total radiation power of $W = 10^{39}$ erg/s and a characteristic radiative cooling time of $t_{\rm rad} = 10\,000$ yr. However, the characteristic timescale for adiabatic cooling due to expansion of the shell is $t_{\rm ad} = 100$ yr. Accordingly, only 1% of the shell's energy can go into X-ray emission. Only when $T \leq 10^6$ K does the function $\lambda(T)$ become two orders of magnitude larger, making efficient radiative energy losses possible.

However, our main conclusion is precisely that the collision energy of the supernova shell and the shell produced by the presupernova at the supergiant stage

Table 2. Expected parameters of the Strömgren zones of type II supernovae

Strömgren zone J2000	l, b, deg	DM, pc/cm^3	EM, pc/cm^6	$\log\tau$ (τ in ms)	$\log t$ (t in yr)
$0117+59$	$126.3-3.5$	49.4	50	–	5.44
$0157+62$	$130.6+0.3$	29.8	70	–	5.30
$0543+23$	$184.4-3.3$	77.7	30	−0.27	5.40
$0614+22$	$188.8+2.4$	96.7	50	−0.29	4.95
$0742-28$	$243.8-2.4$	73.8	70	0.19	5.20
$0835-45$	$263.6-2.8$	68.2	500	0.95	4.05
$0922+06$	$225.4+36.4$	27.3	6	−2.52	5.70
$1111-60$	$291.0-0.1$	–	1500	–	3.81
$1116-41$	$284.5+18.1$	40.5	7	–	6.27
$1136+15$	$241.9+69.2$	4.8	0.6	−3.22	6.70
$1212-62$	$298.5-0.3$	–	1000	–	3.50
$1305-62$	$304.6+0.1$	–	1500	–	3.60
$1342-62$	$308.8-0.1$	–	2500	–	3.70
$1441-60$	$316.3-0.0$	–	1500	–	2.84
$1509+55$	$91.3+52.3$	19.6	1	−2.00	6.37
$1513-59$	$320.3-1.2$	253.2	1000	–	3.19
$1555-53$	$328.4+0.2$	–	3000	–	3.18
$1647-44$	$340.6+0.3$	–	500	–	3.71
$1655-44$	$341.9-0.3$	–	1450	–	3.84
$1710-40$	$346.6-0.2$	–	1200	–	3.79
$1714-38$	$348.5+0.1$	–	3000	–	3.11
$1713-38$	$348.7+0.3$	–	2000	–	3.16
$1717-37$	$349.7+0.2$	–	3000	–	2.42
$1720-37$	$350.1-0.3$	–	2000	–	3.43
$1722-36$	$351.2+0.1$	–	2000	–	3.80
$1731-47$	$342.6-7.7$	121.9	80	–	4.90
$1740-30$	$357.7-0.1$	–	1000	–	3.00
$1801-24$	$5.3-0.9$	289.0	800	–	4.19
$1802-24$	$5.4-1.2$	–	800	–	3.40
$1811-19$	$11.2-0.3$	–	2500	–	3.00
$1818-15$	$15.9+0.2$	–	1500	–	3.69
$1823-12$	$18.8+0.3$	–	2500	–	3.60
$1825-09$	$21.4+1.3$	19.5	60	−1.36	5.37
$1832-10$	$21.8-0.6$	–	1500	–	3.81
$1833-10$	$21.5-0.9$	–	1500	–	2.70
$1846-02$	$29.7-0.3$	–	4000	–	2.82
$1904+05$	$39.2-0.3$	–	700	–	3.40
$1907+07$	$41.1-0.3$	–	800	–	3.30
$1932+22$	$57.4+1.6$	219.0	110	–	4.60
$2016+37$	$74.9+1.2$	–	500	–	3.67
$2046+57$	$94.2+8.6$	99.0	16	–	5.83
$2215+15$	$76.8-32.9$	29.3	4	–	6.40
$2301+58$	$109.1-1.0$	–	400	–	4.10
$2337+61$	$114.3+0.3$	58.4	90	–	4.61

is converted into radiation, which is absorbed by the interstellar gas and forms the Strömgren zone. The properties of this radiation can be determined from the parameters of Strömgren zones presented above. Taking into account the fact that the free path of a photon, l, must be less than the size of the Strömgren zone, $R = 30$ pc, and using computed and tabulated ionization cross sections (see, e.g., [39]), we obtain for a particle density of $N = 7\ \mathrm{cm}^{-3}$ the constraint on the wavelength of the photons $\lambda > 30$ Å. This implies that the temperature of the radiating gas must satisfy the requirement $T < 3 \times 10^6$ K. For a characteristic radiative-loss time scale $t_{\mathrm{rad}} < 100$ yr, we obtain the estimate $T \leq 10^6$ K for the temperature of the ambient medium.

The problem of the formation of this radiation remains unresolved and must be considered separately. Strong inhomogeneity of the medium and strong turbulence seem to play an important role in these processes. For example, we could propose the following scheme. The supergiant shell contains inhomogeneities with enhanced particle densities an order of magnitude higher than the average density. Such inhomogeneities are heated more weakly during the collision of the shells and are also cooled more rapidly—within less than 100 yr, they can reach temperatures of a million Kelvin or so, becoming centers of efficient radiation of the shell's energy. The energy of the remaining gas can be supplied to these inhomogeneities by both thermal conduction and dynamical processes that act to equalize the pressures. We have presented here experimental data that should be taken into account in simulations.

The power law for the decrease of the density with time for $t > 1000$ yr undoubtedly indicates that the gas distribution in the Strömgren zone is nonuniform. This is supported by the presence of strong turbulence during the initial evolution of the Strömgren zone. The ionized gas recombines first in the densest gas clouds. The increase in the recombination time for the least dense HII regions may be related to the fact that some fraction of the energy goes into exciting turbulent motions, which can be an additional source of heat for the least dense plasma regions in late evolutionary stages.

Note also that no such extended Strömgren zones are present around type I supernova remnants. This can be explained by the absence of powerful shells around these supernova, so that the supernova shell is decelerated more slowly and there is no efficient mechanism for the conversion of the kinetic energy of supernova shell into the energy of ionizing radiation.

To conclude, we list in Table 2 objects that we suggest can be identified as the Strömgren zones of type II supernova. The columns of the table contain (1) the name of the object (hours and minutes of right ascension and degrees of declination in the J2000 coordinate system), (2) its Galactic coordinates (l and b), (3) the DM of the pulsars for those objects situated in directions toward pulsars, (4) the EM of the Strömgren zones of type II supernova, (5) the logarithm of the broadening of pulsar pulses at 300 MHz for pulsars situated toward the Strömgren zones of type II supernova, and (6) the logarithm of the age of the object, with t in years.

The possible existence of Strömgren zones around supernova remnants has been discussed many times in the literature [7, 40–45]. At the same time, it has been realized that these objects should be difficult to detect, since most of their radiation is in the far ultraviolet [7, 43, 45]. The data presented here demonstrate that the radio emission of such objects can be detected. We have been able to identify only certain Strömgren zones, whose ages correspond to those of supernova remnants or pulsars. However, since the emission of pulsars is strongly directional, we detect only a small fraction of all pulsars; therefore, the number of supernova Strömgren zones should be much larger than the number of objects in our list. The problem arises of detecting the supernova Strömgren zones against the background of other HII zones. One possible line of research is to compare the brightness temperatures of HII zones at various wavelengths and determine the gas temperatures in these zones, since wide temperature variations from several tens of thousands to a million Kelvin are expected in Strömgren zones.

ACKNOWLEDGMENTS

This work was supported by the Russian Foundation for Basic Research (project no. 00-02-17850), INTAS (grant 00-849), the National Science Foundation (grant N AST 0098685), and the State Science and Technology Program in Astronomy.

REFERENCES

1. J. M. Cordes, J. M. Weisberg, and V. Boriakoff, Astrophys. J. **288**, 221 (1985).
2. A. V. Pynzar' and V. I. Shishov, Astron. Zh. **74**, 663 (1997) [Astron. Rep. **41**, 586 (1997)].
3. A. V. Pynzar' and V. I. Shishov, Astron. Zh. **76**, 504 (1999) [Astron. Rep. **43**, 436 (1999)].
4. A. V. Pynzar' and V. I. Shishov, Astron. Zh. **78**, 585 (2001) [Astron. Rep. **45**, 502 (2001)].
5. D. K. Milne, in *IAU Colloq. 101: Supernova Remnnants and the Interstellar Medium,* Ed. by R. S. Roger and T. L. Landecker (Cambridge Univ. Press, Cambrige, 1988), p. 351.
6. D. H. Clark and J. L. Caswell, Mon. Not. R. Astron. Soc. **174**, 267 (1976).

7. T. A. Lozinskaya, *Supernovae and Stellar Wind. Interaction with the Galactic Gas* [in Russian] (Nauka, Moscow, 1986).
8. J. Rho, Ph. D. thesis (Univ. Maryland at College Park, 1995).
9. W. J. Altenhoff, D. Downes, T. Pauls, and J. Shraml, Astron. Astrophys., Suppl. Ser. **35**, 23 (1978).
10. R. F. Haynes, J. L. Caswell, and L. W. J. Simons, Aust. J. Phys. Astrophys. Suppl. **45**, 1 (1978).
11. T. Handa, Y. Sofue, N. Nakai, *et al.*, Publ. Astron. Soc. Jpn. **39**, 709 (1987).
12. W. J. Altenhoff, D. Downes, L. Goad, *et al.*, Astron. Astrophys., Suppl. Ser. **1**, 319 (1970).
13. R. J. Reynolds, F. L. Roesler, and F. Sherb, Astrophys. J. **192**, L53 (1974).
14. R. J. Reynolds, Astrophys. J. **282**, 191 (1984).
15. R. J. Reynolds and P. M. Ogden, Astron. J. **87**, 306 (1982).
16. R. J. Reynolds, Astrophys. J. **216**, 433 (1977).
17. R. J. Reynolds, Astrophys. J. **203**, 151 (1976).
18. A. Broadbent, C. G. T. Haslam, and J. L. Osborne, Mon. Not. R. Astron. Soc. **237**, 381 (1989).
19. L. Hart and A. Pedlar, Mon. Not. R. Astron. Soc. **176**, 547 (1976).
20. F. J. Lockman, Astrophys. J. **209**, 429 (1976).
21. J. C. Cersosimo, I. N. Azcarate, L. Hart, and F. R. Colomb, Astron. Astrophys. **208**, 239 (1989).
22. J. P. Sivan, Astron. Astrophys., Suppl. Ser. **16**, 163 (1974).
23. S. A. Kaplan and S. B. Pikel'ner, *Physics of the Interstellar Medium* [in Russian] (Nauka, Moscow, 1979).
24. A. V. Pynzar', Astron. Zh. **72**, 462 (1995) [Astron. Rep. **39**, 406 (1995)].
25. A. V. Kovalenko, A. V. Pynzar', and V. A. Udal'tsov, Astron. Zh. **72**, 796 (1995) [Astron. Rep. **39**, 708 (1995)].
26. A. L. Fey, S. R. Spangler, and J. M. Cordes, Astrophys. J. **372**, 132 (1991).
27. M. A. Gordon and T. Cato, Astrophys. J. **176**, 587 (1972).
28. M. P. FitzGerald, Astron. J. **73**, 983 (1968).
29. R. L. Sorochenko, Astron. Nachr. **310**, 389 (1989).
30. K. S. Stankevich and V. P. Ivanov, Pis'ma Astron. Zh. **27**, 339 (2001) [Astron. Lett. **27**, 292 (2001)].
31. R. N. Manchester and J. H. Taylor, *Pulsars* (Freeman, San Francisco, 1977; Mir, Moscow, 1980).
32. J. H. Taylor, R. N. Manchester, and A. G. Lyne, Astrophys. J., Suppl. Ser. **88**, 529 (1993).
33. J. H. Taylor, R. N. Manchester, A. G. Lyne, and F. Camilo, unpublished work (1995).
34. C. S. J. Pun, S. Poirier, G. Sonneborn, *et al.*, Am. Astron. Soc. **193**, 4701 (1998).
35. G. Sonneborn, C. S. J. Pun, R. A. Kimble, *et al.*, Astrophys. J. **492**, L139 (1998).
36. T. V. Smirnova, V. I. Shishov, and D. R. Stinebring, Astron. Zh. **75**, 866 (1998) [Astron. Rep. **42**, 766 (1998)].
37. V. I. Tatarskiĭ, *Wave Propagation in a Turbulent Atmosphere* [in Russian] (Nauka, Moscow, 1967).
38. V. I. Shishov and T. V. Smirnova, Astron. Zh. **79**, 810 (2002) [Astron. Rep. **46**, 731 (2002)].
39. R. A. Syunyaev, *Space Physics* [in Russian] (Sov. Éntsiklopediya, Moscow, 1986).
40. J. C. Brandt, T. P. Stecher, D. L. Crawford, and S. P. Maran, Astrophys. J. **163**, L99 (1971).
41. W. H. Tucker, Astrophys. J. **167**, L85 (1971).
42. N. G. Bochkarev, Diploma work, Astrophysics Department, Moscow State University (1970).
43. M. C. Kafatos and P. Morrison, Astrophys. J. **168**, 195 (1971).
44. G. S. Bisnovatyĭ-Kogan, Astron. Zh. **49**, 453 (1972) [Sov. Astron. **16**, 368 (1972)].
45. S. A. Colgate, Astrophys. J. **174**, 377 (1972).

Translated by A. Getling

Astronomy Reports, Vol. 47, No. 4, 2003, pp. 301–311. Translated from Astronomicheskiĭ Zhurnal, Vol. 80, No. 4, 2003, pp. 331–341.

Photometric and Polarimetric Activity of the Herbig Ae Star VX Cas

D. N. Shakhovskoĭ[1], A. N. Rostopchina[1], V. P. Grinin[1,2], and N. Kh. Minikulov[3]

[1]*Crimean Astrophysical Observatory, Nauchnyĭ, Crimea, 98409 Ukraine*

[2]*Main Astronomical Observatory in Pulkovo, Pulkovskoe sh. 65, St. Petersburg, 196140 Russia*

[3]*Institute of Astrophysics, Academy of Sciences of Tajikistan, ul. Bukhoro 22, Dushanbe, 734670 Tajikistan*

Received August 12, 2002; in final form, August 21, 2002

Abstract—We present the results of our simultaneous photometric and polarimetric observations of the Herbig Ae/Be star VX Cas acquired in 1987–2001. The star belongs to the UX Ori subtype of young variable stars and exhibits a rather low level of photometric activity: only six Algol-like minima with amplitudes $\Delta V > 1^m$ were recorded in 15 years of observations. Two of these minima, in 1998 and 2001, were the deepest in the history of the star's photometric studies, with V amplitudes of about 2^m. In each case, the dimming was accompanied by an increase in the linear polarization in agreement with the law expected for variable circumstellar extinction. The highest V polarization was about 5%. Observations of VX Cas in the deep minima revealed a turnover of the color tracks, typical of stars of this type and due to an increased contribution from radiation scattered in the circumstellar disk. We separated the observed polarization of VX Cas into interstellar ($P_{\rm is}$) and intrinsic ($P_{\rm in}$) components. Their position angles differ by approximately 60°, with $P_{\rm is}$ dominating in the bright state and $P_{\rm in}$ dominating during the deep minima. The competition of these two polarization components leads to changes in both the degree and position angle of the polarization during the star's brightness variations. Generally speaking, in terms of the behavior of the brightness, color indices, and linear polarization, VX Cas is similar to other UX Ori stars studied by us earlier. A number of episodes of photometric and polarimetric activity suggest that, in their motion along highly eccentric orbits, circumstellar gas and dust clouds can enter the close vicinity of the star (and be disrupted there). © *2003 MAIK "Nauka/Interperiodica".*

1. INTRODUCTION

In this paper, we continue our studies of photometric and polarimetric activity of young UX Ori stars, also referred to in the literature as stars with aperiodic Algol-like minima [1]. In our earlier papers (cf. [2–4] and references therein), we demonstrated that the unusual photometric activity of these stars is due to variable circumstellar extinction and testifies to an extremely nonuniform distribution of the matter in the gas and dust disks surrounding them. These papers (see also Natta and Whitney [5]) present evidence that the circumstellar disks of these stars are viewed edge-on or at small angles to the line of sight. This important fact makes it possible to use photometric and polarimetric monitoring of UX Ori stars to study the fine structure of their circumstellar disks.

We present here the results of our simultaneous five-band ($UBVRI$) observations of the linear polarization and brightness of one of the least studied and comparatively inactive stars of this subtype, VX Cas, carried out by our group over 15 years starting in 1987.

2. THE PRINCIPAL CHARACTERISTICS OF VX CAS

The photometry of VX Cas was mainly limited to observations during individual seasons [6–10]. The most detailed studies of the star have been presented by Kardopolov *et al.* [11–14]. As a rule, the brightness minima of VX Cas are of low amplitude and duration. The values of the star's photographic brightness, m_{pg}, in the catalog of Herbig and Bell [15] vary between 10.5^m and 13.3^m. A general impression of the activity of VX Cas can be obtained from distributions of the star's brightness plotted using our data together with those of other authors [6–14, 16] (Fig. 1). They are typical of UX Ori stars: the brightness variations of VX Cas are mainly within 0.5^m of its bright state, with deep minima being extremely rare.

The variable's spectral type was classified as A0III [17] or (A0–A3)V [18]. The latter estimate is confirmed by the recent spectral classification of [19], which gives A0Vep for the spectral type of VX Cas. The spectrum of VX Cas displays moderately strong,

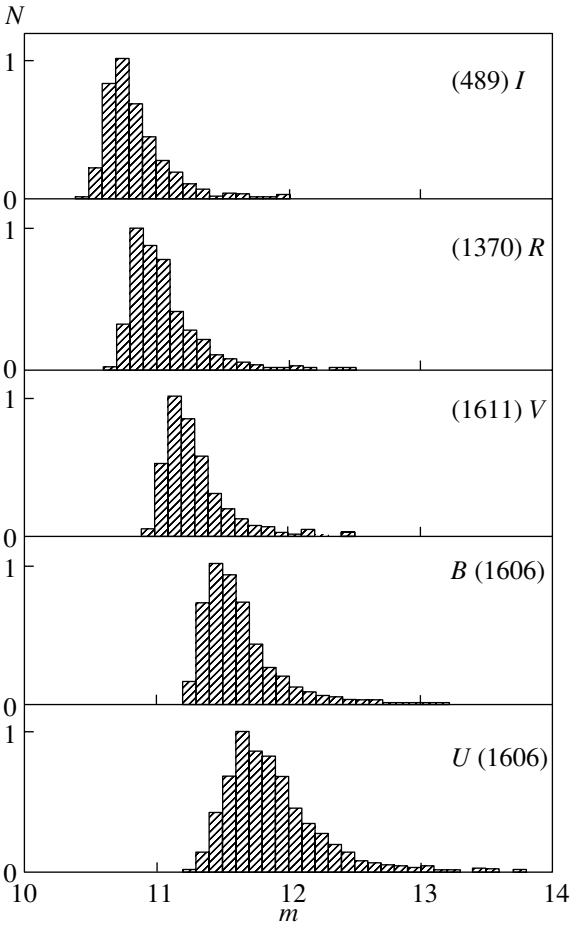

Fig. 1. Activity histograms of VX Cas in the $UBVRI$ bands based on data of the present study and [6–14, 16].

variable, two-component Hα emission [18, 20]. The star's rotation rate is $V \sin i = 178$ km/s [19].

The infrared (IR) observations of [21] and IRAS observations of [22] demonstrated that the star possessed a strong IR excess due to thermal emission from its circumstellar dust. Figure 2 shows the interstellar-extinction-corrected spectral energy distribution (SED) of VX Cas based on our observations during the star's bright state and on the IR data of [21, 22]. In the ultraviolet, we have added the theoretical SED for a Kurucz model [23] for a star of the same spectral type and luminosity class. Using the resulting SED, we find that the IR excess of VX Cas is 46% of the star's bolometric luminosity. Comparison with similar estimates for other UX Ori stars [2, 24–26] shows that this IR excess is among the highest, testifying to the presence of a large amount of gas near the star.

According to [27], the distance to VX Cas is 635 pc, corresponding to a bolometric luminosity of $\log(L_*/L_\odot) = 1.69$ [28]. According to [28], the position occupied by VX Cas in the Hertzsprung–Russell diagram does not differ from those for other UX Ori stars. Comparison with evolutionary tracks yields 2.4 $M_\odot$ for the star's mass and about 2.5 million years for its age. Thus, VX Cas is similar to other Herbig Ae/Be UX Ori stars in terms of its basic characteristics and IR excess.

3. OBSERVATIONS

Our photometric and polarimetric monitoring of VX Cas was carried out using the five-band photopolarimeter designed by Piirola [29] mounted at the 1.25 m telescope of the Crimean Astrophysical Observatory. This instrument permits simultaneous observations of polarization and brightness in all five bands, $UBVRI$. The effective wavelengths of the instrumental system are close to the standard wavelengths of the Johnson system. We reduced our observations to this system using observations of comparison star 1 from Pugach and Koval'chuk [30]. As a rule, we observed using a diaphragm with 10″ diameter; a 15″ diaphragm was used on nights with poor seeing. We averaged photometric observations acquired on a single night. The mean photometric

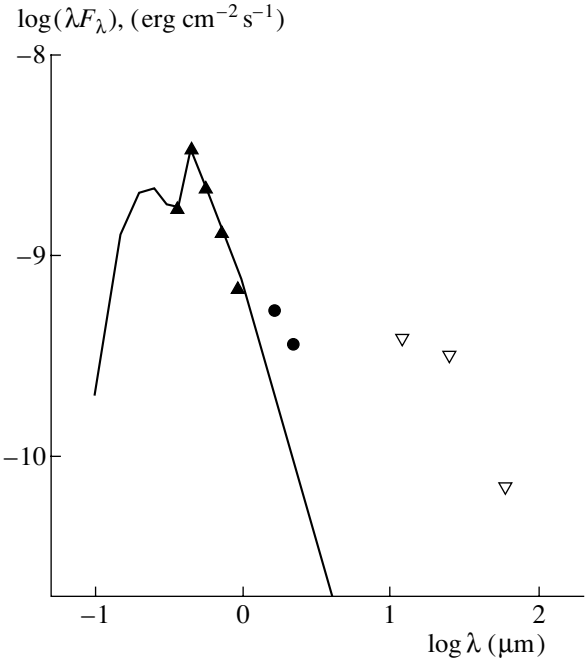

Fig. 2. The reddening-corrected ($E(B-V)=0.3$ [28]) spectral energy distribution of VX Cas during the maximum brightness state based on data of the present study ($UBVRI$) and the IR observations of [21, 22]. The solid curve is the spectral energy distribution of an A0V star from the models of Kurucz [23].

uncertainty was 0.03^m in U and 0.01^m in all other bands.

The vast majority of our observations of VX Cas were obtained in the mode of simultaneous photometry and polarimetry. Depending on the observing conditions (weather, the star's brightness), each linear-polarization measurement consisted of 4 to 24 measurements of the Stokes parameters. We corrected our polarization measurements for the instrumental polarization. Corrections for the instrumental polarization and the system's zero point were determined each month from observations of standard stars. During our 15-year monitoring of VX Cas, we obtained $UBVRI$ photometric measurements on 491 nights, with the star's linear polarization being measured simultaneously on 361 of these nights. The results of our observations are presented in the electronic table available at ftp://cdsarc.u-strasbg.fr/pub/cats/J and in Figs. 1–8.

4. RESULTS

The histograms of the photometric activity of VX Cas presented in Fig. 1 show that, like most other UX Ori stars, VX Cas is usually in its bright state. Deep minima are observed very seldom. During the 15 years of our observations, we recorded only six minima with amplitudes exceeding 1^m, and only two of them had amplitudes in excess of 2^m. During each of the observed minima, we recorded an increase in the degree of linear polarization, accompanied by strong changes of the polarization position angle (Fig. 3). However, we can see from Fig. 3 that the polarization position angle sometimes varied considerably (by as much as 30°–40°) even outside minima.

The minimum of 2001 was observed over approximately three months and was one of the longest. However, the deepest part of this minimum was extremely short and lasted only several days.

The minimum of 1998 was also very long and showed a complex structure (Fig. 4), with three subsequent subminima ($V=13.0^m$, $V=12.6^m$, and $V=11.9^m$). The last two subminima were observed on the ascending branch of the first subminimum, which was the main one in terms of its amplitude. This complex minimum of VX Cas in 1998 resembles a minimum with similar duration and depth that was observed for another UX Ori star, WW Vul [31], which also consisted of individual deep subminima.

Figure 4 shows that the brightness variations of VX Cas during the minimum of 1998 were accompanied by simultaneous variations of the degree of linear polarization: dimming was accompanied by an increase of the star's polarization, and *vice versa*. This means that the complex behavior of the brightness of VX Cas during this minimum, which could have been interpreted as a sequence of two outbursts during the star's egress from the deep minimum if there were no simultaneous polarization measurements, actually

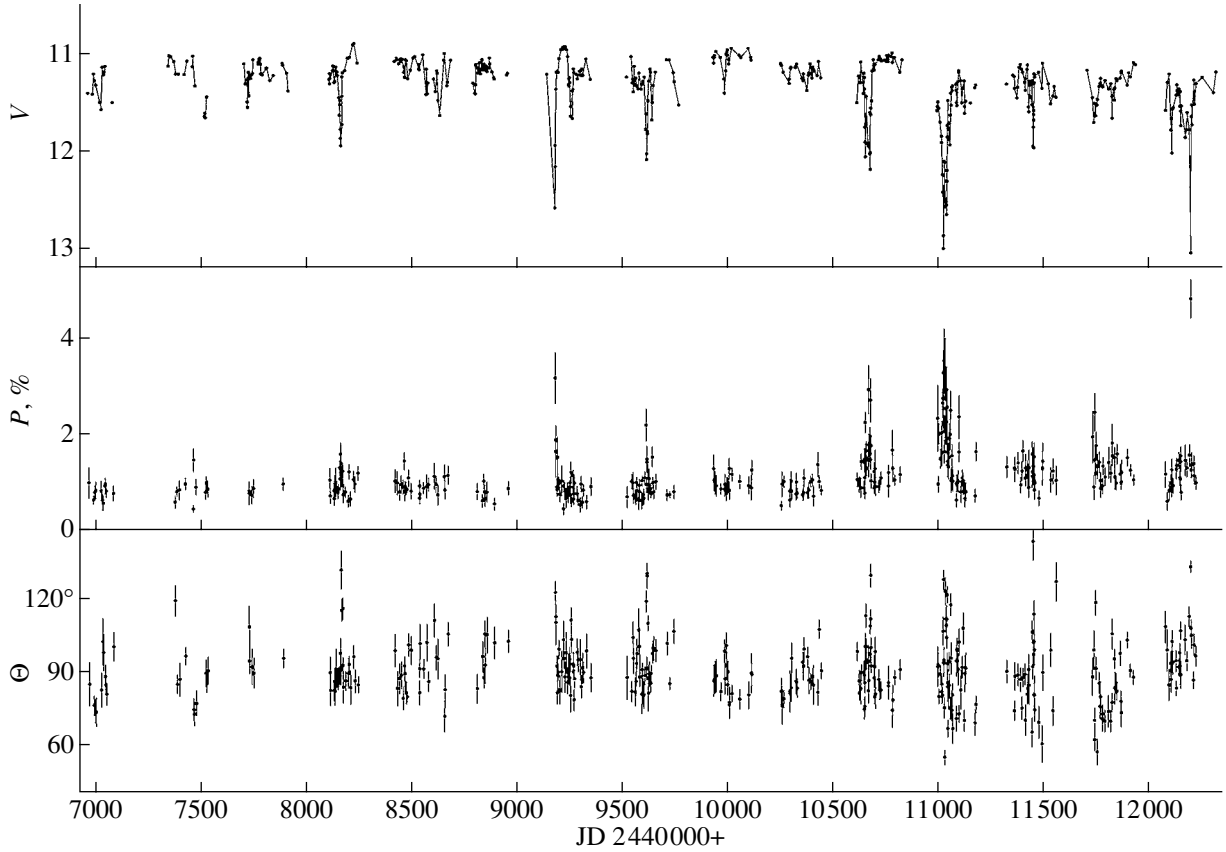

Fig. 3. *V* light curves and curves of linear polarization parameters for VX Cas. An anticorrelation between variations of the brightness and linear polarization is evident.

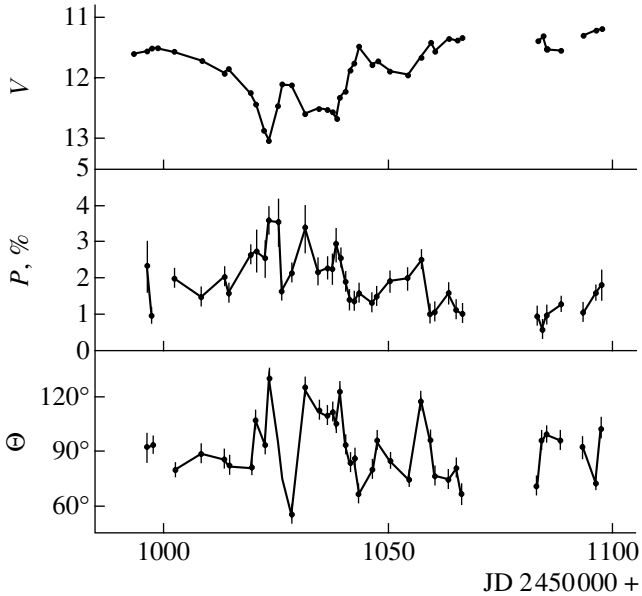

Fig. 4. Behavior of the brightness and linear polarization of VX Cas during the deep minimum of 1998. Note the complex structure of the minimum and the strict anti-correlation between variations of the star's brightness and linear polarization, testifying to the eclipsing nature of all the observed features of the minimum.

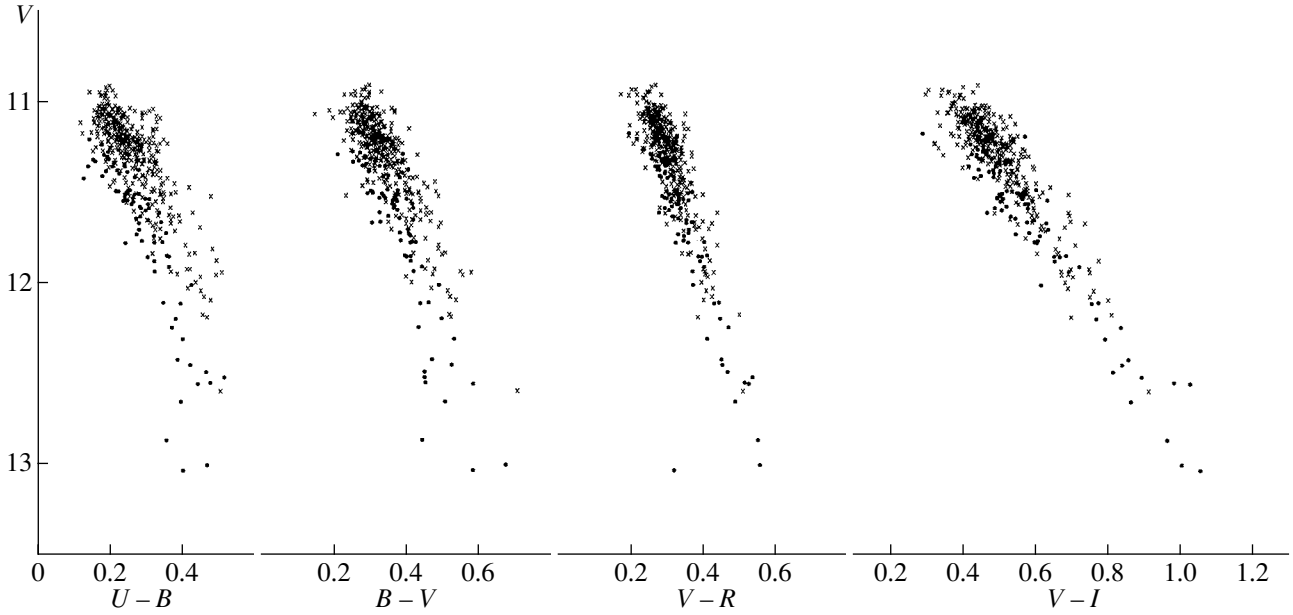

Fig. 5. Color–magnitude diagrams for VX Cas plotted using the data of our electronic table. The filled dots are the star's color indices for the 1998 and 2001 seasons, when the deepest photometric minima were observed.

had an eclipsing nature, reflecting the complex structure of a circumstellar cloud crossing the line of sight.

This episode is a good example showing the importance of simultaneous brightness and polarization observations for young, irregular variables. Such observations make it possible to correctly interpret stellar photometric activity when photometric data alone are insufficient to properly identify the variability mechanism.

We can see in Fig. 4 that the increase in the polarization and the variable's dimming during the ingress into the minimum do not begin simultaneously: the polarization begins to increase when the amplitude of the brightness decrease exceeds $\approx 0.5^m$. This provides evidence that the intrinsic polarization of VX Cas in its bright state is rather low, so that the polarization observed in this state is predominantly interstellar. We will see in Section 5 that this is confirmed by the results of numerical simulations.

The color–magnitude diagrams in Fig. 5 display the variations of the color indices of VX Cas during the minima. When the star's brightness decreases, its color indices increase (the star becomes redder), which can be explained by the selective extinction of the stellar radiation in gas and dust clouds crossing the line of sight. Beginning with a certain brightness level (which is different for different color indices), the direction of the color track in the $(U-B)$–V and $(B-V)$–V diagrams changes, and the reddening no longer occurs. This feature of the photometric behavior of VX Cas is also characteristic of many other UX Ori stars and is explained by the increased contribution of the stellar radiation scattered by circumstellar dust when the direct radiation is attenuated as it passes through the circumstellar gas and dust clouds [32]. If we estimate the derivative $d(B-V)/dV$ from the upper part of the $(B-V)$–V color track (which is unaffected by the scattered light), we can derive the reddening law for VX Cas associated with the interstellar dust: $R = 5 \pm 0.1$. Figure 5 also shows that the color tracks in the color–magnitude diagrams display a large scatter, especially in the blue.

Figure 6 presents the relation between the polarization of VX Cas and its brightness in each of the five bands. The polarization increase in each of the bands follows a nonlinear law. This type of dependence of the polarization on brightness is characteristic of variable circumstellar extinction [32] and is observed for all UX Ori stars (cf. the reviews [2–4] and references therein). Figure 6 also shows that the observed data points display a significant (up to 1%) scatter of the polarization at all brightness levels, including the star's bright state. We discuss possible origins of this scatter in Section 5.

Figure 7 present the V-band diagram of the Stokes parameters. The cloud of data points in the upper part of the diagram corresponds to the star's brightness variations near its bright state. Variations of the Stokes parameters during the brightness mimima are mainly due to changes of the parameter P_y. In the two deepest minima, the linear polarization parameters P_x and P_y were close to each other (within 3σ).

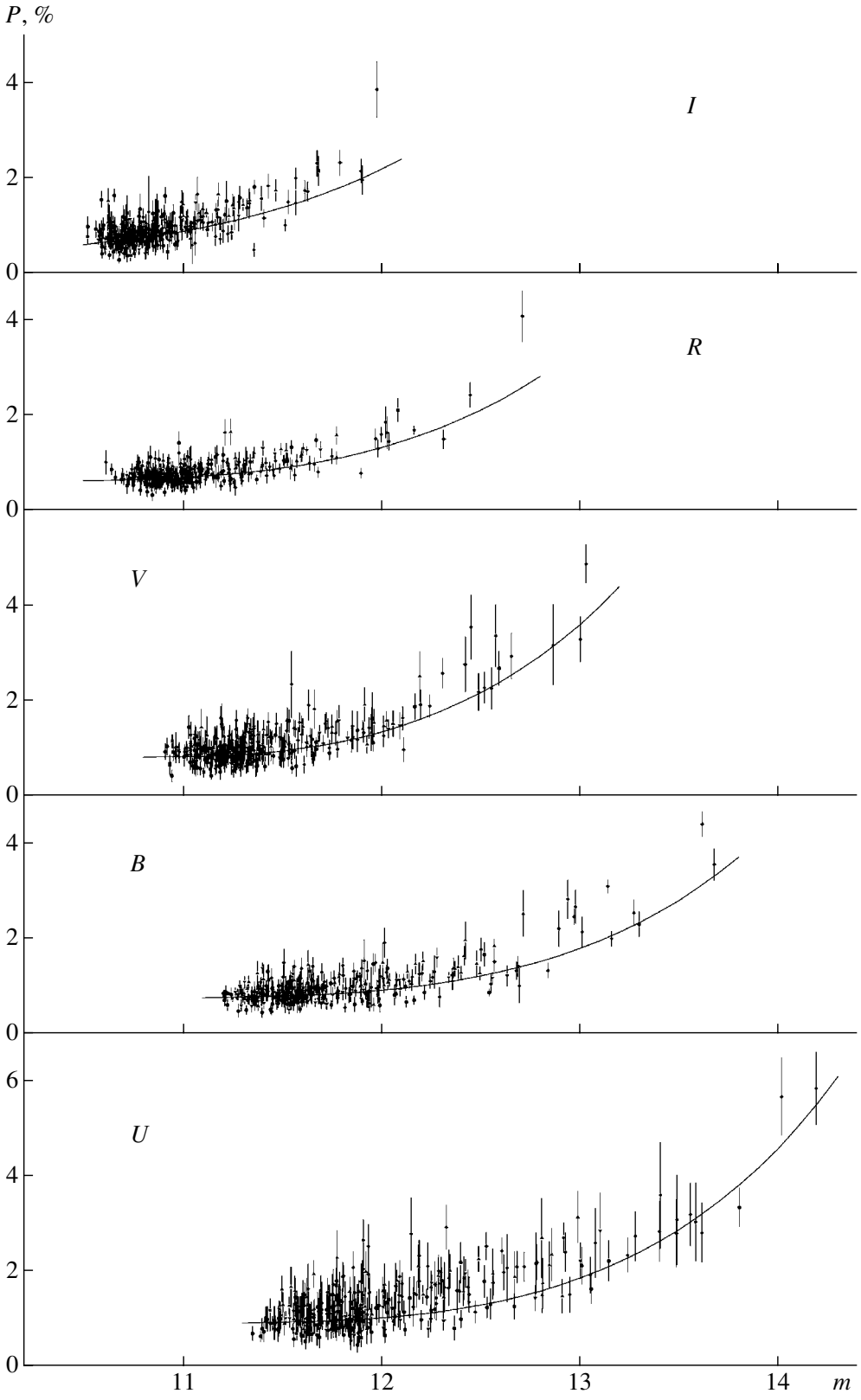

Fig. 6. Relation between polarization and brightness for VX Cas in the $UBVRI$ bands, plotted using the data of our electronic table. The solid curves are the theoretical relations for the variable circumstellar extinction model of [32], plotted using data on the intrinsic and interstellar polarization from the table.

A more detailed analysis of the Stokes parameters shows that, during the minimum of 1998, the points in the (P_x, P_y) diagram moved quite differently from the linear shift expected for nonvarying parameters of radiation scattered by circumstellar disk: we observed motion along "loops" in the (P_x, P_y) diagram, through the leftmost points of Fig. 7, during both the ingress and egress of the first, deepest, subminimum; similar "loops" with lower amplitudes were observed during both subsequent, less deep, subminima.

The remaining brightness minima observed by us were either insufficiently deep or too brief to enable a detailed discussion of the behavior of the Stokes parameters in the (P_x, P_y) diagram.

We present the characteristic wavelength dependences of the linear polarization of VX Cas in various brightness states in Fig. 8. In all cases except the brightest state, when the interstellar polarization dominates, the level of polarization grows toward the blue. A similar transformation of the linear-polarization wavelength dependences is observed for other UX Ori stars [2]. This is clearly due to selective extinction in circumstellar clouds, resulting in larger optical depths of the clouds toward shorter wavelengths. This also explains the reddening of UX Ori stars during the ingress into their minima (see above), as well as the more rapid increase of the contribution of scattered radiation to the combined light of the star+circumstellar disk in the blue, reflected in the behavior of the $U - B$ and $B - V$ color indices in the color–magnitude diagrams (Fig. 5).

5. ANALYSIS AND INTERPRETATION OF THE RESULTS

5.1. Photometry

Thus, during the 15 years of our photometric and polarimetric monitoring of VX Cas, we acquired observations in both the star's brightest state and in its deepest minima. In two of the minima, in 1998 and 2001, the amplitude of the brightness variability exceeded 2^m. Comparison of our data with the photometric data of other authors [6–14, 16] shows that these two minima were the deepest in the history of the photometric studies of VX Cas.

The complex structure of the 1998 minimum (Fig. 4) testifies that the gas and dust cloud that crossed the line of sight consisted of three separate, optically thick fragments (cores) that were denser than the rest of the cloud. However, judging from its shape and duration, the 2001 minimum was due to a single extended cloud with a dense dust core embedded in it. Comparison of the color indices in the color–magnitude diagrams with the earlier results [6–14, 16] reveals no significant differences in the

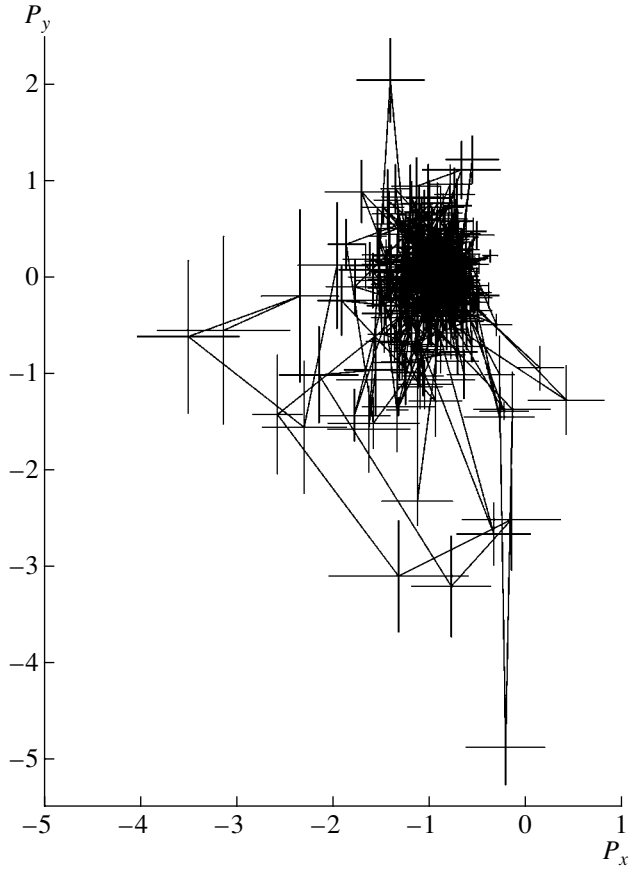

Fig. 7. Variations of the Stokes parameters in the P_x, P_y plane, based on the data in the electronic table.

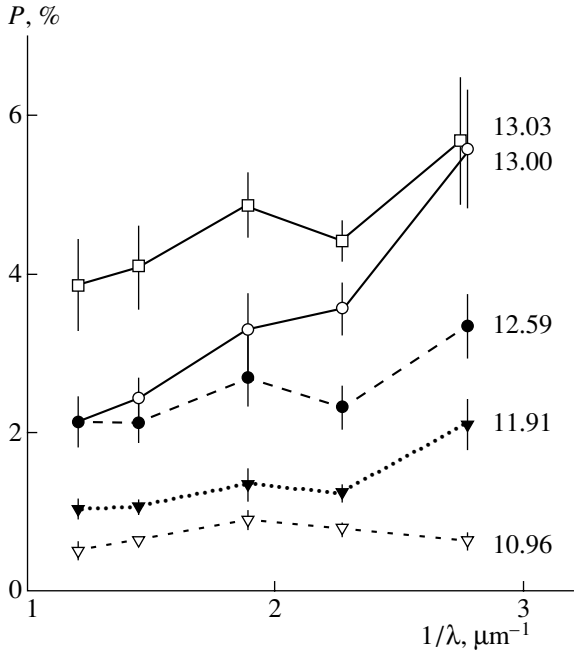

Fig. 8. Wavelength dependences of the linear polarization of VX Cas for different brightness states (the V magnitudes are indicated to the right).

variations of the star's color indices. A turnover of the color tracks was observed for $U-B$ and $B-V$, and an indication of a turnover in $V-R$ can be found for the minimum of 2001 (Fig. 5).

As noted above, the color–magnitude diagrams for VX Cas (Fig. 5) display a significant scatter of the data points. To clarify the origins of this scatter, we considered the color–magnitude diagrams for each observing season separately. This demonstrated that the states of the star observed during the last four seasons, including the deep minima of 1998 and 2001, were responsible for the increased scatter in the diagrams. The beginning of the 1998 observing run found the star already faint. As noted above, this brightness minimum had a duration of about 100 days and a complex structure, with the star returning to its bright state only in 1999. The dots in Fig. 5 show the data for this observing season; for part of the 1999 run, until the star's complete egress from the minimum; and for 2001. It is clear that these data points lie parallel to the bulk of the data points and are somewhat displaced downwards. This shows that the minima of 1998 and 2001 occurred against the background of an overall decrease of the star's brightness by approximately 0.3–0.4^m. Figure 4 shows that this decrease began during the 1998 observing run and is still continuing.

We can see from the light curve of VX Cas (Fig. 3) that, in some cases, the star displayed its maximum brightness immediately after its egress from a minimum. This was especially evident during the two minima of 1990 and 1993, when the star's brightness immediately after the minima was higher than the normal brightness level by approximately 0.2^m–0.3^m. Such brightenings of the star could be due to a local clearing of the circumstellar medium after a circumstellar cloud had crossed the line of sight. Another reason for enhanced brightness could be additional scattered light due to an increased amount of dust in the nearest vicinity of the star immediately after a minimum. In this latter case, it is natural to assume that the star's dimming during the minimum and subsequent brightening were due to the same gas and dust cloud, which had crossed the line of sight and then moved around the star, becoming an additional source of scattered light. In this case, we can estimate the distance from the star of the clouds responsible for these episodes. Taking into account the fact that the duration of the episodes from the star's ingress into a minimum until it reaches its maximum brightness after the egress from the minimum was two to three months (Fig. 3), if the star's mass is 2.4 $M_\odot$ (cf. Section 2), we find that the circumstellar clouds passed the star at a distance not exceeding 1 AU in each of these episodes.

If we assume that such clouds are fragments of a classical accretion disk that is dominated by circular Keplerian motion and that matter spirals toward the star, we should observe recurrent eclipses of the star with a period of about 2–3 months. Since such eclipses were not observed, the circumstellar clouds must have entered the close vicinity of the star in motion along highly eccentric orbits. Such clouds should be disrupted partially or completely by tidal perturbations as they pass through periastron, supplying circumstellar matter to the region surrounding the young star. This scenario is confirmed by another episode of photometric and polarimetric activity of VX Cas, discussed below.

5.2. Polarimetry

Comparing the observations for VX Cas with those for other stars of the same type [2–4, 24, 25], we find considerable similarities. In general, the polarimetric activity of VX Cas can be explained in models with variable circumstellar extinction [32]. The same conclusion was recently drawn by Oudmaijer *et al.* [33], who present observations of linear polarization and brightness for a large sample of young stars, each observed on several nights. Their polarimetric observations of VX Cas were obtained on nine nights; simultaneous brightness measurements were obtained on seven nights and show an anticorrelation between the star's variations of brightness and linear polarization, as is characteristic of UX Ori stars.

As noted above, in addition to variations of the polarization parameters of VX Cas due to the star's eclipses, we also observed strong fluctuations of the polarization position angle during the star's bright state. We believe the origin of these fluctuations to be scattering of the star's light by gas and dust clouds passing nearby the star but not crossing the line of sight.

We can see in Fig. 3 that, in addition to variability with time scales from several days to several weeks, the brightness and polarization of VX Cas also show slower variations on a time scale on the order of several years, or even longer. As already noted, the level of the bright state of VX Cas was systematically lower during the last four seasons (by approximately 0.3^m) compared to the earlier observing runs. Simultaneously, the star's linear polarization in the bright state increased by approximately 0.5%. The scatter of the polarization position angle also increased considerably: it was about 30° during our first observing seasons but reached 60°–70° during the last four seasons.

Figure 3 shows that all these changes coincide in time with the deep and long minimum of 1998.

Interstellar and intrinsic polarization of VX Cas in its bright state from (1)

P_{is} %	$\sigma_{P_{is}}$ %	PA_{is}	$\sigma_{PA_{is}}$	$P_{in}(0)$ %	$\sigma_{P_{in}}$ %	$PA_{in}(0)$	$\sigma_{PA_{in}}$
0.95	0.06	64.2°	1.7°	0.42	0.03	117.8°	2.3°
0.78	0.04	68.7	1.2	0.35	0.02	121.6	1.6
0.98	0.05	62.6	1.5	0.59	0.03	124.7	1.7
0.68	0.04	69.4	1.8	0.40	0.03	126.3	2.0
0.40	0.08	68.6	5.5	0.57	0.06	121.3	2.9

After its completion and until the present time (i.e., by 2002), the star has not returned fully to the state observed prior to 1998. This means that the giant gas and dust cloud that gave rise to the extended eclipse of 1998 was partially or completely disrupted when it passed close to the star, adding some amount of dust to the star's nearest vicinity. The presence of this dust increased the circumstellar extinction and apparently influenced the conditions for the illumination of the rest of the circumstellar dust by the star. This could be related to the increase in the scatter of the polarization position angle observed after the minimum of 1998.

5.3. The Intrinsic Polarization of VX Cas

Our polarization measurements in the two deep minima (1998 and 2001) gave comparable (within 3σ) values for the linear polarization parameters. Thus, despite the features of the photometric and polarimetric behavior of VX Cas that provide evidence for strong fluctuations of the scattered light, in our attempt to isolate the star's intrinsic polarization, we will proceed on the assumption (as in our earlier papers) that the Stokes parameters of the scattered light were constant during the entire analyzed time interval. As a result, we obtain some kind of time-averaged information about the star's intrinsic polarization. Assuming that the dust clouds screening the star do not introduce their own polarization and only attenuate the star's direct (unpolarized) light, we can use the relation between the observed polarization variations and the amplitude of the star's brightness variations Δm:

$$\mathbf{P}_{obs}(\Delta m) = \mathbf{P}_{is} + \mathbf{P}_{in}(\Delta m), \qquad (1)$$

where

$$\mathbf{P}_{in}(\Delta m) = \mathbf{P}_{in}(0) \times 10^{0.4\Delta m}. \qquad (2)$$

Here, $\mathbf{P}_{obs}(\Delta m)$ is the observed linear polarization, $\mathbf{P}_{in}(0)$ is the star's intrinsic polarization in the bright state, and $\mathbf{P}_{is}$ is the interstellar polarization.

Writing this equation for observations of VX Cas in each of the bands and separately for each of the Stokes parameters, we obtain a set of equations whose weighted least-squares solution yields the mean values of the interstellar and intrinsic polarization in the bright state (table). The table shows that the position angles of the intrinsic polarization of VX Cas in different bands coincide within the statistical errors. The same is true of the interstellar component of the polarization. Since we solved the system of equations (1) independently for each of the five bands, the coincidence of the polarization position angles testifies to the self-consistency of our solution.

It also follows from the table that the wavelength dependence of the interstellar polarization generally does not contradict the theoretical dependence, described by Serkowski law with a maximum in the V band. However, the agreement is not satisfactory in the blue (U band), possibly due to variability of the Stokes parameters of the scattered light or to an insufficient number of observations in the deep brightness minima. We can see in the table that the position angles of the intrinsic and interstellar polarization differ by about 60°. The star's intrinsic polarization during the bright state is considerably lower than the interstellar polarization. These two facts throw light on the origin of the variations of the polarization position angle of VX Cas when the star dims (Fig. 3), which are due to competition between the two mechanisms polarizing the star's radiation.

5.4. The Polarization Map of the Surroundings of VX Cas

Another method of determining the interstellar polarization is based on observations of the polarization of stars in the nearest vicinity of the studied star. The main difficulty of this method is to select stars at approximately the same distance as the program star (based on their interstellar reddening). This selection assumes that the stars have no intrinsic reddening due to circumstellar extinction and that the interstellar reddening per unit distance is the same for all stars in that region. In our case, we used the list of surrounding stars selected in this way by Bartaya and Kharadze [34]. We measured the linear polarization for these stars, as shown in Fig. 9. The polarization

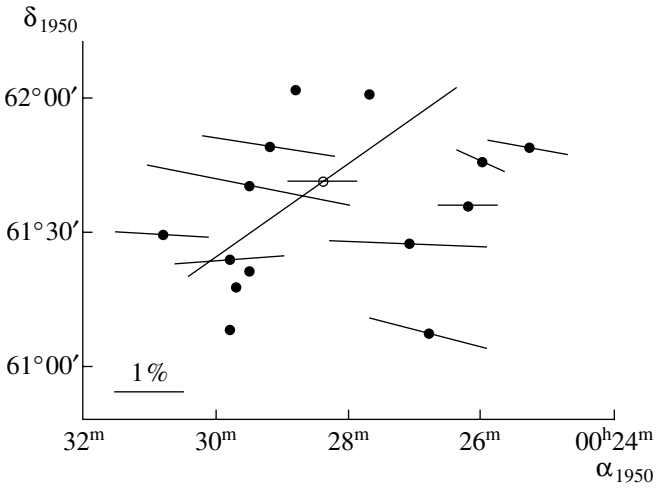

Fig. 9. Polarization map of the surroundings of VX Cas. The polarization of VX Cas itself is shown for its bright state and for the deepest part of the minimum of 2001.

vectors of the surrounding stars are collinear within $\approx 20°$, testifying to a fairly regular structure for the magnetic field near the star. The weighted mean V-band parameters of the interstellar polarization estimated using all the surrounding stars are $P_{IS} = 1.67 \pm 0.24\%$ and $\theta_{IS} = 82° \pm 3°$. Comparison with the data in the table shows that the position angle, θ_{IS}, coincides with the theoretical value derived from (1), $\theta_{\rm is}$, to within 15–20°, whereas the degree of polarization, P_{IS}, is considerably higher than the model value, $P_{\rm is}$. This may indicate that some of the surrounding stars are actually at larger distances than VX Cas.

6. CONCLUSIONS

The results of our many-year photometric and polarimetric observations of VX Cas presented here demonstrate that the behavior of the star's linear polarization parameters and photometric characteristics is in general agreement with that expected for variable circumstellar extinction: the polarization in the bright state of the star is determined by its interstellar component, whereas the intrinsic polarization, due to scattering of the star's light by the circumstellar dust, dominates during deep minima.

Several specific features of the photometric and polarimetric activity of VX Cas indicate that at least some of the gas and dust clouds giving rise to brightness minima move in strongly eccentric orbits and can appear very near the star, at distances on the order of 1 AU or less. Such clouds are partially or completely disrupted by tidal forces and supply additional matter to the star's neighborhood. This is especially evident for the deep and long minimum of 1998: after the passage of the gas and dust cloud that caused this minimum, some dust remained near the star, causing it to dim by approximately $\Delta V = 0.3^m$ and leading to an increase in its polarization by $\approx 0.5\%$, which has persisted for several years. Events such as this complement our earlier results [3, 35], which formed the basis for the conclusion that there can be strong fluctuations of the Stokes parameters of the scattered light of UX Ori stars due to close passages of circumstellar gas and dust clouds.

ACKNOWLEDGMENTS

This study was partially supported by the Program "Nonstationary Phenomena in Astrophysics" of the Presidium of the Russian Academy of Sciences.

REFERENCES

1. B. V. Kukarkin *et al.*, *General Catalogue of Variable Stars*, 4th ed. (Nauka, Moscow, 1985).
2. V. P. Grinin, N. N. Kiselev, N. Kh. Minikhulov, *et al.*, Astrophys. Space Sci. **186**, 283 (1991).
3. V. P. Grinin, in *The Nature and Evolutionary Status of Herbig Ae/Be Stars*, Ed. by P. S. Thé, M. R. Pérez, and E. P. J. van den Heuvel, Astron. Soc. Pac. Conf. Ser. **62**, 63 (1994).
4. V. P. Grinin, in *Disks, Planetesimals, and Planets*, Ed. by F. Garzon, C. Eiroa, D. de Winter, and T. J. Mahoney, Astron. Soc. Pac. Conf. Ser. **219**, 216 (2000).
5. A. Natta and B. A. Whitney, Astron. Astrophys. **364**, 633 (2000).
6. G. V. Zaĭtseva, Perem. Zvezdy **17**, 294 (1970).
7. G. V. Zaĭtseva, Candidate's Dissertation in Physics (Moscow, 1974).
8. E. A. Kolotilov, G. V. Zaĭtseva, and V. I. Shenavrin, Astrofizika **13**, 253 (1977).
9. A. F. Pugach, Astron. Astrophys. **39**, 8 (1979).

10. D. Böhm, Mitt. Verand. Sterne **10**, 76 (1984).
11. V. I. Kardopolov and G. K. Filip'ev, Perem. Zvezdy **22**, 103 (1985).
12. V. I. Kardopolov and G. K. Filip'ev, Perem. Zvezdy **22**, 153 (1985).
13. V. I. Kardopolov and G. K. Filip'ev, Perem. Zvezdy **22**, 455 (1985).
14. V. I. Kardopolov, G. K. Filip'ev, A. F. Shaimieva, and N. A. Shutemova, Astron. Zh. **65**, 951 (1988) [Sov. Astron. **32**, 498 (1988)].
15. G. H. Herbig and K. R. Bell, Lick Obs. Bull., No. 1111 (1988).
16. A. V. Berdyugin, Izv. Krym. Astrofiz. Obs. **87**, 107 (1993).
17. G. U. Koval'chuk and A. F. Pugach, Kinem. Fiz. Neb. Tel **8**, 71 (1992).
18. E. A. Kolotilov, Astrofizika **13**, 33 (1977).
19. A. Mora, B. Merin, E. Solano, *et al.*, Astron. Astrophys. **378**, 116 (2001).
20. O. V. Kozlova, V. P. Grinin, and A. N. Rostopchina, Astron. Astrophys. Trans. **8**, 249 (1995).
21. I. S. Glass and M. V. Penston, Mon. Not. R. Astron. Soc. **167**, 237 (1974).
22. W. B. Weaver and G. Jones, Astrophys. J., Suppl. Ser. **78**, 239 (1992).
23. R. Kurucz, Astrophys. J., Suppl. Ser. **40**, 1 (1979).
24. A. N. Rostopchina, V. P. Grinin, A. Okazaki, *et al.*, Astron. Astrophys. **327**, 145 (1997).
25. A. N. Rostopchina, V. P. Grinin, D. N. Shakhovskoĭ, and P. S. Tè, Astron. Zh. **77**, 420 (2000) [Astron. Rep. **44**, 365 (2000)].
26. A. N. Rostopchina, V. P. Grinin, and D. N. Shakhovskoĭ, Astron. Zh. **78**, 60 (2001) [Astron. Rep. **45**, 51 (2001)].
27. V. S. Shevchenko, *Herbig Ae/Be Stars* (FAN, Tashkent, 1989).
28. A. N. Rostopchina, Astron. Zh. **76**, (1999) [Astron. Rep. **43**, 113 (1999)].
29. V. Piirola, Observ. Astrophys. Labor. Univ. Helsinki Rept. **6**, 151 (1984).
30. A. F. Pugach and G. U. Koval'chuk, Perem. Zvezdy **22**, 9 (1983).
31. V. P. Grinin, N. N. Kiselev, N. Kh. Minikulov, and G. P. Chernova, Pis'ma Astron. Zh. **14**, 514 (1988) [Sov. Astron. Lett. **14**, 219 (1988)].
32. V. P. Grinin, Pis'ma Astron. Zh. **14**, 65 (1988) [Sov. Astron. Lett. **14**, 27 (1988)].
33. R. D. Oudmaijer, J. Palacios, C. Eiroa *et al.*, Astron. Astrophys. **379**, 564 (2001).
34. R. A. Bartaya and E. K. Kharadze, Bull. Abastuman. Astrofiz. Obs. **38**, 12 (1968).
35. V. P. Grinin, D. N. Shakhovskoĭ, V. I. Shenavrin, *et al.*, Astron. Zh. **46**, 715 (2002) [Astron. Rep. **46**, 646 (2002)].

Translated by N. Samus'

Astronomy Reports, Vol. 47, No. 4, 2003, pp. 312–325. Translated from Astronomicheskiĭ Zhurnal, Vol. 80, No. 4, 2003, pp. 342–356.

Modeling of Emission Spectra of the Flaring Red Dwarf EV Lac: Active Regions, Flares, and Microflares

I. Yu. Alekseev[1], É. A. Baranovskiĭ[1], R. E. Gershberg[1], I. V. Il'in[2], B. P. Pettersen[3], D. N. Shakhovskoĭ[1], and M. Jablonsky[4]

[1]*Crimean Astrophysical Observatory, Nauchnyĭ, Crimea, 98409 Ukraine*

[2]*Astronomy Department, Oula University, Finland*

[3]*Cartographical Institute, Agricultural University, Norway*

[4]*Nordic Optical Telescope, Canary Islands, Spain*

Received April 28, 2002; in final form, May 23, 2002

Abstract—Echelle spectrograms of the flaring red dwarf EV Lac obtained on the Nordic Optical Telescope are used to study the chromosphere of the star during the impulsive flare of 23:19 UT on August 30, 1994, and in two nearby time intervals when $UBVRI$ photometry showed the star to be in a quiescent state. The high spectral resolution of the observations enabled the detection of broad Balmer emission wings in the nonflaring state, which are interpreted as evidence for microflares. Semiempirical models for active regions in the chromosphere, flares, and microflares are constructed and used to compare the main physical characteristics of these structures. The place of the detected microflares in the overall energetics of flare events in EV Lac is discussed. © *2003 MAIK "Nauka/Interperiodica".*

1. INTRODUCTION

Many studies have been dedicated to calculations of theoretical models for the chromospheres of late-type stars, beginning with the pioneering work of Kandel [1]. However, there exist only a few chromospheric models for active M dwarfs displaying chromospheric emission that are based firmly on observations. Kelch *et al.* [2] and Giampapa *et al.* [3] constructed models using CaII K line profiles, but these refer only to the lower part of the chromosphere where the radiation of this ion forms. In the chromospheric model for EQ Vir calculated by Giampapa *et al.* [3], the observed fluxes in the resonance doublets of calcium and magnesium required different filling factors for the sources of these lines.

Mauas and Falchi [4] calculated a semiempirical model for the atmosphere of the flare star AD Leo in its quiescent state, selecting the model parameters in order to simultaneously reproduce a large number of observed quantities: the stellar continuum from the $UVBR$ bands to 25 μm; the profiles of the Balmer lines, the Na D doublet, the Mg b triplet, the CaI λ 4227 Å and CaII K lines, and a component of the infrared triplet of this ion at λ 8499 Å; and the fluxes in the Ly_α MgII h and k lines. Eight elements were taken into account in these calculations, assigning them solar abundances and assuming a turbulence velocity of 1–2 km/s. In the resulting model, the Ly_α flux was a factor of three higher than the observed value, the observed and calculated fluxes for the magnesium doublet coincided, the flux in the CaII K line was a factor of five higher than the observed value, and the fluxes in the H_α, H_β, H_γ, and H_δ lines differed from the observed values by −34, 13, 17, and 27%, respectively. Some of these discrepancies can be attributed to differing activity states for the star during nonsimultaneous observations in different regions of the spectrum.

Efremovich *et al.* [5] constructed a grid of hydrostatic chromospheric models for AD Leo, varying the depths of the temperature minimum and the base of the transition zone while requiring that the temperature gradient remain constant: $dT/d\log m = \text{const}$, where m is the radial density from infinity to the atmospheric level considered in g/cm^2. They found that the observed H_α profile for the quiescent state of the star is best reproduced when the temperature minimum is at the level $\log m = -1$ and the base of the transition zone is at $\log m = -4$.

Recently, Baranovskiĭ, Gershberg, and Shakhovskoĭ [6, 7] modeled emission-line spectra of the flaring red dwarf EV Lac in its quiescent and active states based on spectral and photometric observations carried out at the Crimean Astrophysical Observatory (CrAO) as part of a program of coordinated observations in 1994 and 1995 [8]. They used the algorithm of [9–10] for the calculation of semiempirical models for

radiating astrophysical objects. The spectral observations were obtained on the 2.6-m Shain telescope of the CrAO on six nights in 1994 at $\lambda\lambda$ 4190–5480 Å with a resolution of 4 Å, and on five nights in 1995 near the H_α line with a resolution of 0.37 Å on the first night and 0.74 Å on the remaining nights. Photoelectric monitoring of the star was carried out on the 1.25-m reflector of the CrAO.

The calculation of the emission-line spectra of EV Lac in its quiescent state consisted of constructing a hydrostatic chromosphere model that reproduced the mean observed equivalent widths and profiles of the H_α, H_β, and H_γ emission-line profiles and did not yield significant emission in the HeI λ 4471 Å line, which is not observed in the spectra of this star outside of flares. The photoelectric observations were used to select time intervals in which there were no flares. It was possible to reproduce the observations using three models: for a chromosphere uniformly covering the entire stellar surface and for ensembles of active regions occupying one-half and one-third of the stellar surface and contributing all the observed chromospheric line emission, with the absence of such emission from the remaining parts of the surface. In all three models, the observations required the presence of a temperature plateau in the chromosphere, extending in height over the column density range from $\log m = -5.5$ to $\log m = -2.3$, where most of the flux in the Balmer lines is formed. The electron temperature in this region is 6500–7000 K, and the electron density ranges from 10^{11} to 2×10^{12} cm^{-3}. Having an extent in depth of about 500 km, this structure lies appreciably closer to the stellar surface than the analogous plateau in the solar atmosphere.

Taking into account the hydrogen-line filling factor of the chromosphere of EV Lac [6] indicated that the active regions should have higher density, higher optical depth, higher mean electron temperature, a broader temperature range in the temperature plateau, and a smaller extent in depth of this plateau (i.e., a larger gradient $dT/d\log m$) than a uniform chromosphere.

Baranovskiĭ *et al.* [6, 7] calculated emission-line spectra of EV Lac in its active state for six times during four flares. $UBVRI$ observations were used to estimate the additional continuous emission of the star. It was assumed that the flares develop in one of the active regions, which occupy a total of one-third of the stellar surface, with the area of the flare being an additional free parameter. The calculations showed that, as in the quiescent state, the flare structures required the presence of a temperature plateau, with its lower boundary at a depth of $\log m = -1$ and its upper boundary at depths from $\log m = -3$ to $\log m = -2$. The electron temperature in the plateau region was 6000–7000 K, while the electron density reached 3×10^{12}–2×10^{13} cm^{-3}.

Here, we carry out a similar analysis of spectral observations of EV Lac obtained using the SOFIN echelle spectrograph [11] mounted on the Nordic Optical Telescope (NOT) on the Canary Islands. This instrument has a higher spectral resolution and covers a much broader range of wavelengths in each exposure, enabling us to obtain qualitatively new results.

2. OBSERVATIONS

Spectral monitoring of EV Lac on the 2.56-m NOT telescope was carried out using the SOFIN echelle spectrograph on November 3–4, 1993 and August 29–31, 1994. We used a low-resolution camera with a two-pixel resolution of $R = 30\,000$ and an entry slit width of 1.6". The Astromed-3200 CCD camera with 1152×298 pixels recorded 35 spectral orders in the wavelength range 3600–9000 Å, each of which covered about 130 Å. The mean exposure time was 5 min. The reduction of the resulting echelle spectrograms was carried out using the 3A package [12] and included the standard procedures for flat-fielding, subtraction of scattered light using two-dimensional spline fits, determination of the spectral orders, removal of cosmic rays, and integration with weighting functions. The wavelength calibration was carried out using a thorium–argon comparison spectrum, and the wavelengths in individual orders were obtained on the basis of general agreement for all lines in the image. The typical wavelength error at the center of the images was about 50–100 m/s. The final steps of the reduction of the spectrograms were corrections for vignetting and the orbital motion of the Earth.

Table 1 presents general information about the EV Lac spectra obtained on the NOT. The observation phases were calculated using the data of Alekseev [13].

Only the spectrograms of August 30, 1994, obtained during coordinated observations of EV Lac when parallel $UBVRI$ monitoring observations were obtained at the CrAO, were subjected to a further detailed analysis. The deep dip in the light curve in Fig. 1 is due to a discontinuity in the guiding when the star passes through the meridian.

3. MODELING THE SPECTRA OF THE QUIESCENT STATE

In their modeling of spectra obtained during the quiescent state of EV Lac, Baranovskiĭ *et al.* [6] applied the algorithm described in [6] to mean emission-line profiles obtained in time intervals when a visual

Table 1. Spectral observations of EV Lac on the NOT

Date	Nov. 3, 1993	Nov. 4, 1993	Aug. 29, 1994	Aug. 30, 1994	Aug. 31, 1994
Number of spectra	3	48	46	76	7
Phase	0.66	0.89	0.75	0.21	0.44
$W_{\mathrm{H}\alpha}$, Å	4.10 ± 0.04	3.94 ± 0.03	4.11 ± 0.07	3.90 ± 0.06	4.08 ± 0.09
$W_{\mathrm{H}\beta}$, Å	7.19	5.67 ± 0.24	7.65 ± 0.55	6.98 ± 0.14	5.4 ± 0.6
$W_{\mathrm{H}\gamma}$, Å		4.58 ± 0.49	7.38 ± 0.35	5.14 ± 0.25	2.1 ± 1.0
$W_{\mathrm{H}\delta}$, Å			5.22 ± 0.29	4.22 ± 0.32	
$W_{\mathrm{H}\varepsilon}$, Å				4.74 ± 0.38	
$W_{\mathrm{K\ CaII}}$, Å				13.5 ± 1.6	
$W_{\mathrm{H\ CaII}}$, Å				8.65 ± 0.77	

inspection of the light curves did not reveal any obvious flares. However, the NOT spectrograms obtained in 1994 show that there are substantial variations in the stellar spectra obtained during such intervals: in the presence of nearly constant H_α and H_β intensities, the H_δ intensity varies by a factor of a few. Therefore, we first analyzed spectra in the interval UT 21:05–21:20, when the Balmer line equivalent widths were small, so that these spectra were most likely to correspond to a genuine quiescent state. Figure 1 shows that the guiding discontinuity referred to above occurred during the first three minutes of this exposure. Observations at the Stephanion Observatory of the University of Thessaloniki in Greece at this same time did not indicate any significant brightness variations [8].

Figure 2a compares the Balmer and CaII H line profiles observed in the indicated time interval (solid curves) with the calculated profiles of these lines (dotted curves) for the quiescent chromospheric model of [6], in which one-third of the stellar surface is occupied by active regions and there is no hydrogen-line emission or absorption from the remaining two-thirds. The line profiles are normalized to the adjacent continuum level. The CaII emission is superimposed on a strong absorption line, so that its adjacent continuum is appreciably lower. The profiles show that, if the spectral resolution is lowered to that of the CrAO observations [6], there will be a satisfactory agreement between the observed and calculated profiles of the H_α and H_β lines, which were those primarily used in [6], but the divergence between the corresponding profiles grows rapidly at shorter wavelengths.

To improve the agreement, we varied the physical parameters and size covered by the active regions while preserving the condition of hydrostatic equilibrium; the best fit we could obtain is shown in Fig. 2b. Figure 3 presents the initial model for the active regions from [6], denoted as "3" in Fig. 5 in that paper and here as model 2a; 24% of the stellar surface is covered by active regions in model 2b. The line intensities in model 2b exceed the observed values by factors of three to five, but when the line emission is averaged with the contribution from the "empty" surface that is free from emission and absorption lines, we obtain profiles that are close to the observed profiles.

A comparison of Figs. 2a and 2b shows that we were not able to achieve a good agreement in the line wings as we improved the agreement of the profile intensities. However, broad line wings are observed during flares. Therefore, we attempted to reproduce the observed profiles as a sum of the radiation of quiescent active regions and flares.

In addition to making it possible to fit for the observed broad wings, adding a flare contribution improves the ratios of the equivalent widths of the Balmer lines: since there is an appreciable variety of Balmer decrements during flares, varying the intensity of the flare emission enables us to produce the maximum equivalent width for any line in the interval from H_β to H_ε.

Naturally, adding flares required adjustment of the parameters for the active regions; the final result is shown in Fig. 2c. In this case, the agreement between the observed and calculated Balner line profiles is substantially better. While we were searching for a suitable model for the line profiles, we systematically monitored the flare brightness in the continuum to ensure that the brightness of the star did not significantly exceed the observed value. The best-fit model yielded $\Delta U \sim 0^m.01$, which does not contradict our assignment of the spectrogram to the quiescent state

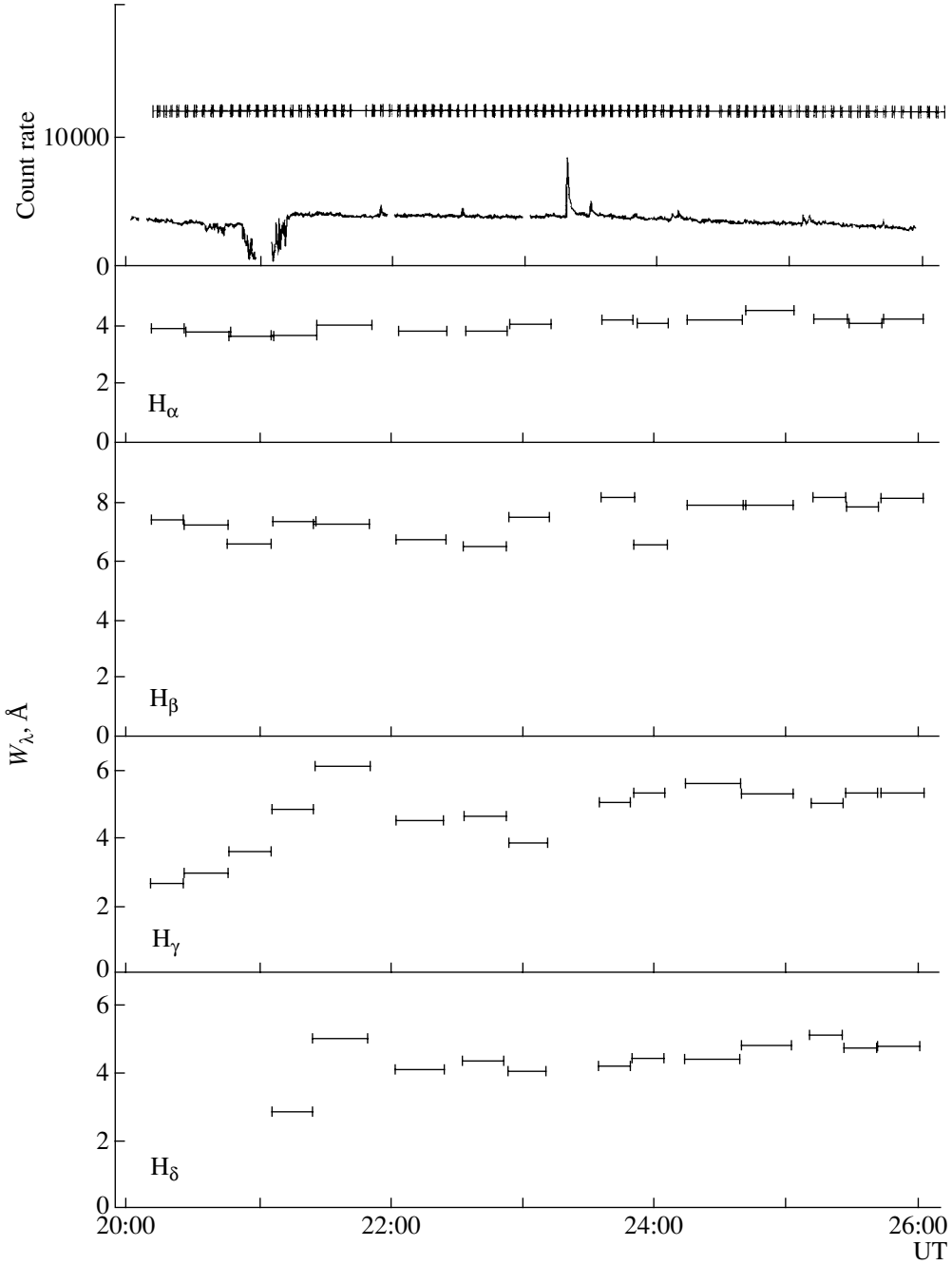

Fig. 1. *U* light curve of EV Lac obtained on August 30–31, 1994 (upper panel) and measured emission-line equivalent widths (four subsequent panels). The positions of several dozen intervals of spectral observations of the star are indicated on the time axis of the upper panel.

of the star. Accordingly, the variable structures we have added should be considered microflares rather than flares.

The agreement of the observed and calculated CaII H profiles in Fig. 2c remained unsatisfactory. Improvement of this agreement requires that we increase the density in the microflare model or vary the run of the temperature in regions with temperatures below 10 000 K accordingly. In this case, however, the fit to the Balmer lines worsens. We were not able to find a good fit to all the lines using a single microflare. We were finally able to achieve good agreement by adding three microflares with different temperatures and characteristic densities to the active-region emission (Fig. 2d). Note that the idea that microflares might be responsible for variations in the emission-

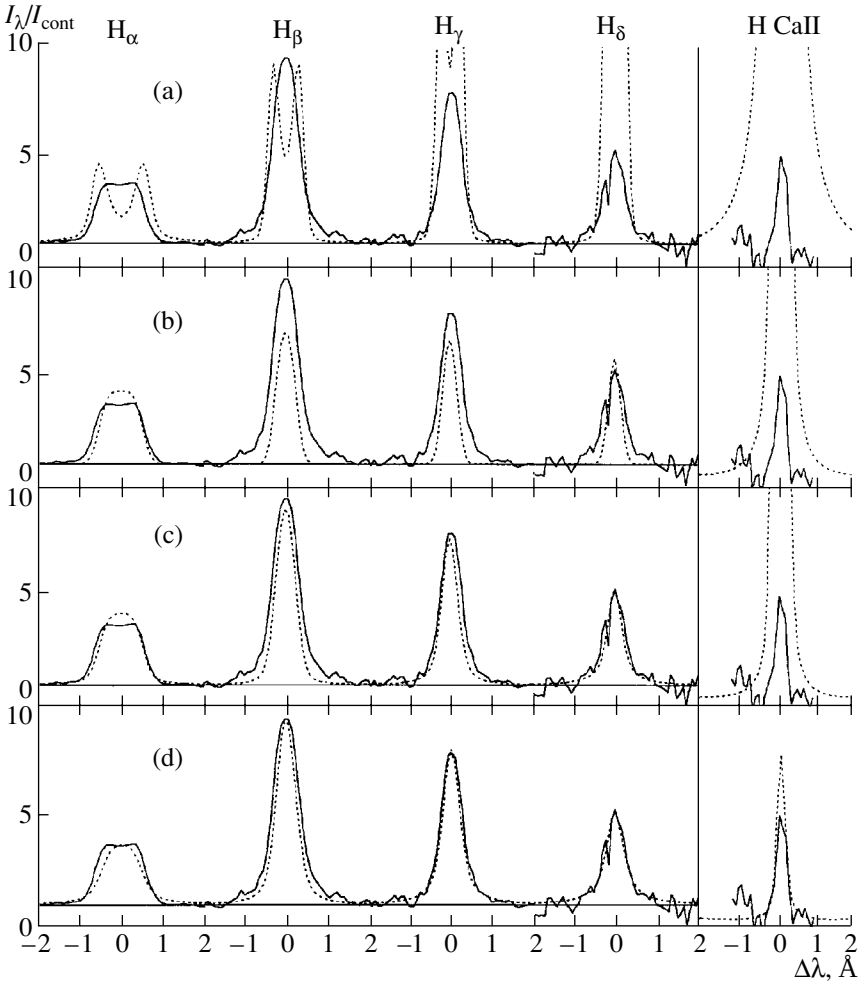

Fig. 2. Profiles of emission lines in the spectrum of EV Lac on August 30, 1994 at UT 21:05–21:20. The solid curves show the observed profiles and the dotted curves the calculated profiles for models (a) 2a, (b) 2b, (c) 2c, and (d) 2d (see text for more detail).

line profiles in the absence of photometrically detectable flares has been qualitatively discussed earlier (see, for example, [14]).

Thus, the best reproduction of the observed spectrograms of EV Lac for August 30, 1994, at UT 21:05–21:20 was achieved by a model simultaneously including the emission of active regions covering 21% of the visible hemisphere of the star and three microflares. The model of these active regions is denoted 2d in Fig. 3, and the models for the microflares will be discussed below. In model 2d, the areas of the active regions and of the three flares are in the ratio 21 : 2 : 1 : 0.5, and their contributions to the total H_β equivalent width are 22, 16, 40, and 22%, respectively. Although the microflares contribute about fourth-fifths of the flux in the line, their contribution to the continuum remains modest—overall, it should exceed the total brightness of the star by only $\Delta U \sim 0^m.015$, which is below the detection threshold of our photometric observations.

We then carried out a similar analysis for the spectrogram of EV Lac obtained on August 30, 1994 at UT 23:35–23:50. Figure 4 is analogous to Fig. 2: Figures 4a–4d compare the observed emission-line profiles for this time interval with profiles calculated using model "1/3" from [6], which we denote model 4a (it coincides with model 2a; Fig. 4a), with a refined model for the active regions (Fig. 4b), a model including the active regions and a single microflare (Fig. 4c), and a model including the active regions and three microflares, which increase the star's brightness by $\Delta U = 0^m.024$ (Fig. 4d). All the active-region models for this time interval (4a, 4b, 4c, and 4d) are also shown in Fig. 3.

Table 2 presents the parameters for all the active-region models we have considered: the fraction of the visible disk of the star occupied by active regions and

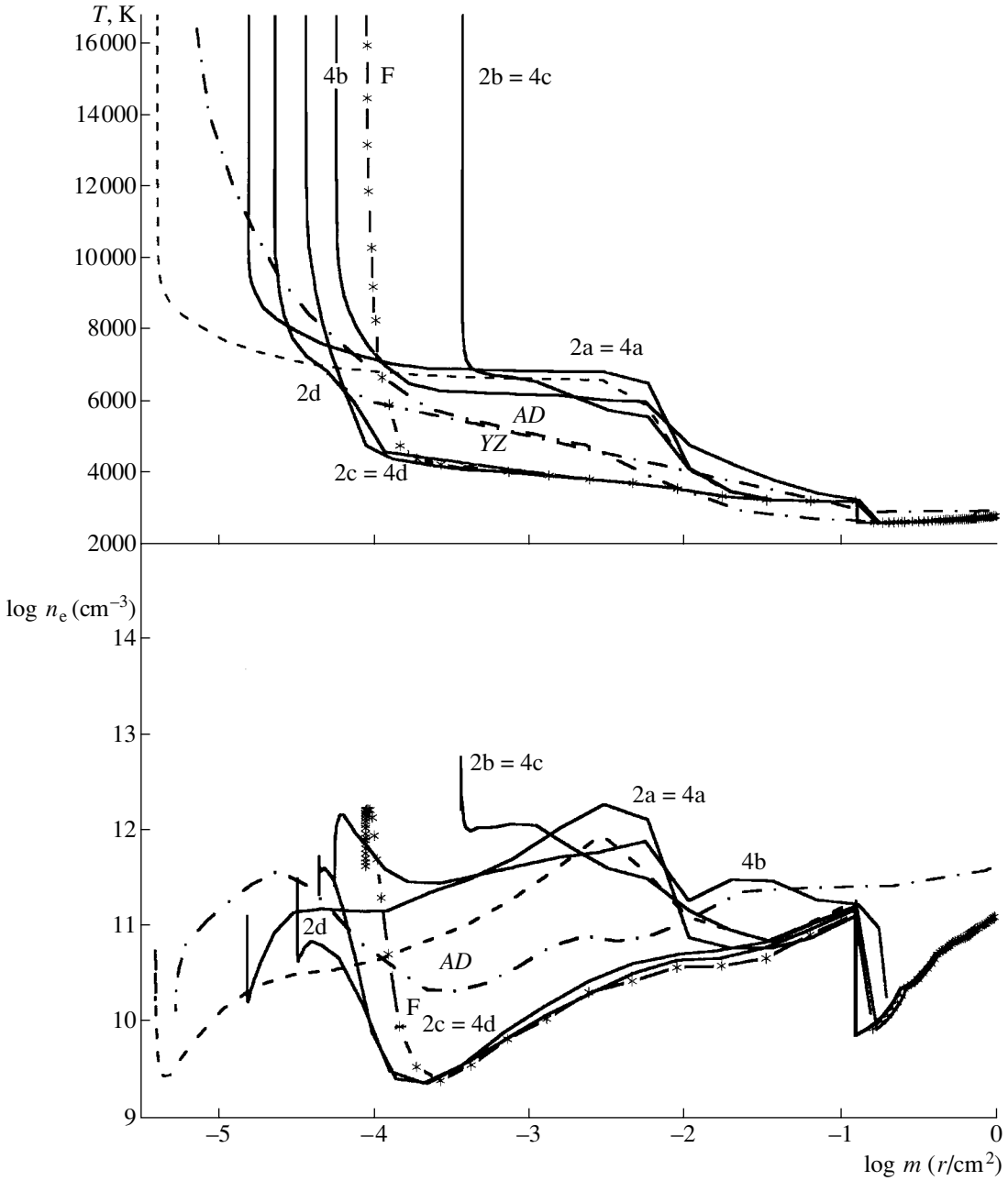

Fig. 3. Semiempirical models for the active regions on EV Lac (solid curves), uniform-chromosphere models for YZ Cmi [3] and AD Leo [4] (dot-dashed curves), and the uniform-chromosphere model for EV Lac from [7] (dashed curve). The active-region model during a flare of EV Lac on August 30, 1994 at UT 23:19 is shown by the dashed curve with asterisks, marked by the F.

the ranges of the column density, electron density, total density, and temperature encompassing the region of the stellar chromosphere from which 80% of the Balmer emission arises. It also gives a comparison of the observed and calculated equivalent widths for the hydrogen and calcium lines and the optical depths at the centers of these lines; for models c and d, the total equivalent widths for the active regions and microflares are indicated. The absolute intensities at the center of the H_β line are also given.

Table 2 and Figure 3 show that the same active-region model can fit the spectrum for UT 21:05–21:20 with only active-region emission and the spectrum for UT 23:35–23:50 with contributions from the active regions and a single microflare. Another active-region model can fit the spectrum for the first interval with contributions from the active regions and one

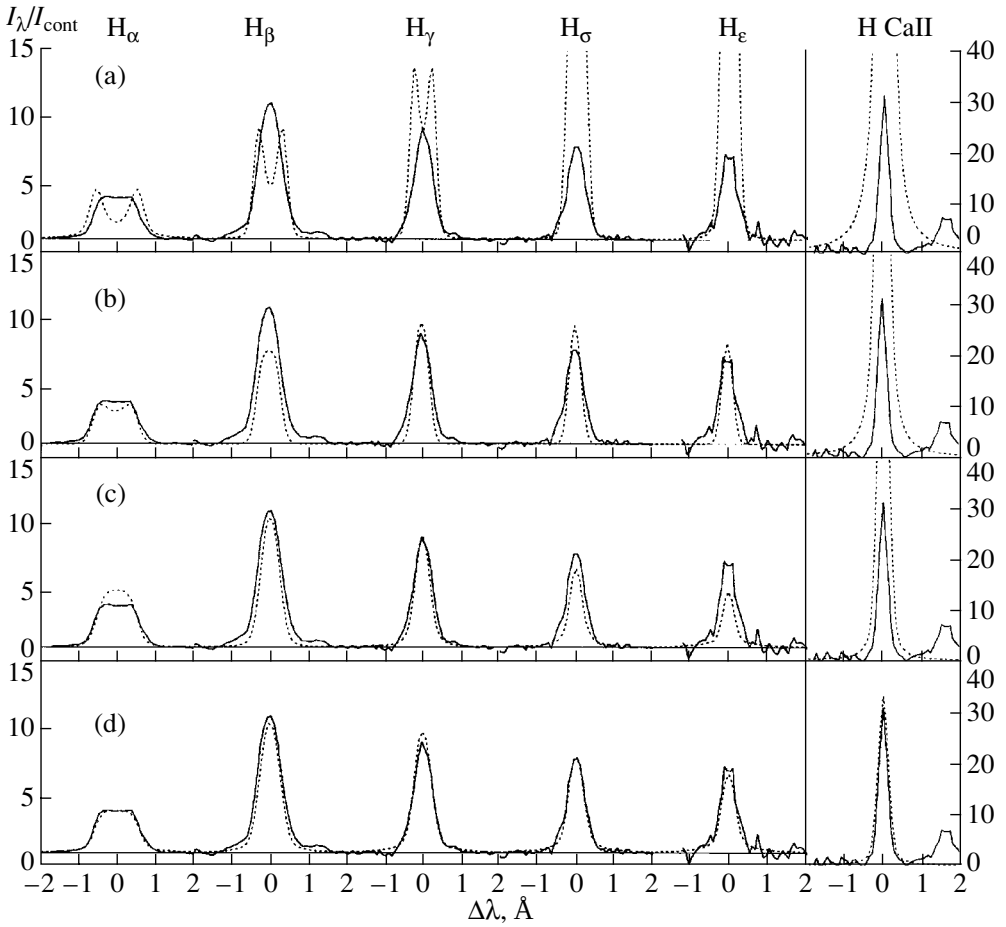

Fig. 4. Profiles of emission lines in the spectrum of EV Lac on August 30, 1994 at UT 23:35–23:50. The solid curves show the observed profiles and the dotted curves the calculated profiles for models (a) 4a, (b) 4b, (c) 4c, and (d) 4d (see text for more detail).

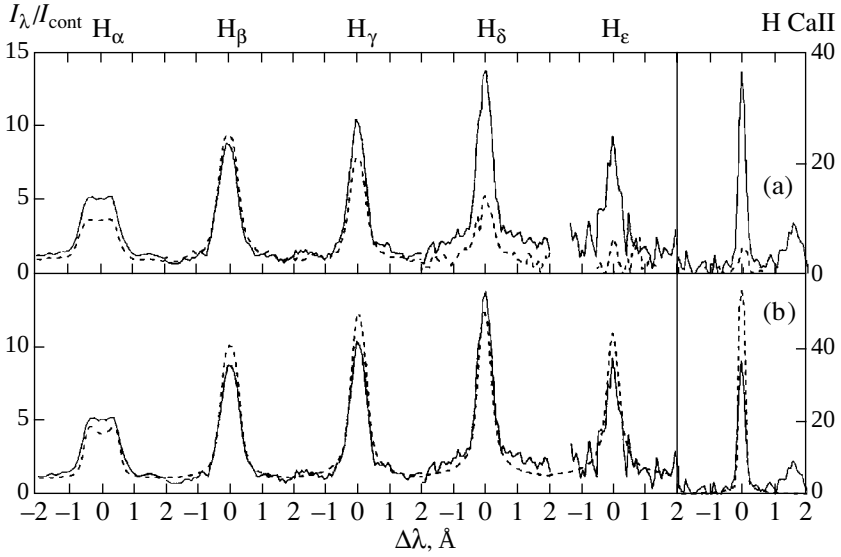

Fig. 5. The solid curves show profiles of emission lines in the spectrum of EV Lac on August 30, 1994 at UT 23:16–23:19. The dashed curves show (a) the profiles observed at UT 21:05–21:20 and (b) the model representation of the flare emission as a sum of the contributions of the active regions and three flares.

Table 2. Models for chromospheric active regions on EV Lac

Spectrogram for UT 21:05–21:20							
Parameter		Model 2b		Model 2c		Model 2d	
S, %		24		21		18	
$\log m$ (g/cm^2)		−3.4...−3.2		−4.4...−4.2		−4.5...−4.2	
$\log n_e$ (cm^{-3})		12.8–12.0		11.6–11.0		10.7–10.7	
$\log n_H$ (cm^{-3})		12.8–14.4		11.8–12.8		11.8–12.4	
T_e, K		15 400–6740		12 900–6150		9740–6830	
				$(W_{\rm ar} : W_{\rm mf1})_{H\beta} = 32 : 68$		$(W_{\rm ar} : W_{\rm mf1} : W_{\rm mf2} : W_{\rm mf3})_{H\beta} =$ 22 : 16 : 40 : 22	
Line	$W_\lambda^{\rm meas}$, Å	$W_\lambda^{\rm calc}$, Å	τ	$\Sigma W_\lambda^{\rm calc}$, Å	τ	$\Sigma W_\lambda^{\rm calc}$, Å	τ
H_α	3.5	3.7	36	4.2	13	3.5	3.3
H_β	7.2	3.5	5.0	5.6	1.8	5.8	0.46
H_γ	4.9	2.5	1.7	4.1	0.62	4.8	0.15
H_δ	2.7	1.9	0.79	2.8	0.29	3.3	0.07
H CaII	1.0	10	4×10^4	3.9	4×10^4	2.0	4×10^4
$I_{H\beta}$, 10^6 erg cm^{-2} s^{-1} ster^{-1} Å		0.90		0.25		0.10	
Spectrogram for UT 23:35–23:50							
Parameter		Model 4b		Model 4c		Model 4d	
S, %		24		21		24	
$\log m$ (g/cm^2)		−4.3...−2.2		−3.4...−3.2		−4.4...−4.2	
$\log n_e$ (cm^{-3})		11.9–11.9		12.8–12.0		11.6–11.0	
$\log n_{\rm H}$ (cm^{-3})		12.0–14.8		12.8–14.3		11.8–12.8	
T_e, K		12 200–6020		15 400–6740		12 900–6150	
				$(W_{\rm ar} : W_{\rm mf1})_{H\beta} = 60 : 40$		$(W_{\rm ar} : W_{\rm mf1} : W_{\rm mf2} : W_{\rm mf3})_{H\beta} =$ 18 : 4 : 69 : 9	
Line	$W_\lambda^{\rm meas}$, Å	$W_\lambda^{\rm calc}$, Å	τ	$\Sigma W_\lambda^{\rm calc}$, Å	τ	$\Sigma W_\lambda^{\rm calc}$, Å	τ
H_α	4.2	3.4	50	4.8	36	3.9	13
H_β	8.1	4.4	7.0	5.8	5.0	6.6	1.8
H_γ	4.7	4.0	2.3	4.4	1.7	5.8	0.62
H_δ	3.8	3.2	1.1	3.2	0.79	4.4	0.29
H_ε	3.5	2.6	0.6	2.3	0.44	3.4	0.16
H CaII	8.8	35	1×10^5	25	4×10^4	11	4×10^4
$I_{H\beta}$, 10^6 erg cm^{-2} s^{-1} ster^{-1} Å		0.72		0.90		0.25	

microflare and the spectrum for the second interval with contributions from the active regions and three microflares. The relations 2b ⇒ 4c and 2c ⇒ 4d, i.e., the drift of one model in Table 2 to the right and downward, has a simple physical explanation: between the two time intervals near UT 23:19 and UT 23:30, which we have treated as quiescent states of the star, there were flares with maximum amplitudes of $\Delta U^{\max} = 0\overset{m}{.}85$ and $\Delta U^{\max} = 0\overset{m}{.}27$ [8], which increased the contribution of the microflare emission in the stellar spectrum at UT 23:35–23:50 from 0 to 40% in the case 2b ⇒ 4c or from 68% to 82% in the case 2c ⇒ 4d.

The fact that, as Fig. 3 shows, active-region mod-

els 2d and 4d proved to be fairly similar suggests that our procedure for subtracting the contribution of the microflares from the total spectra was reasonably effective.

In connection with the resulting estimates of the total areas on EV Lac covered by active regions, $S = 18–24\%$ of the visible disk, we note that, in the zonal spottedness model of [8] for this star for this period, the total area covered by dark spots was about 14% of the total surface area of the star [8].

Naturally, we cannot expect a completely unambiguous picture from our complex, multicomponent representations of the observed emission-line spectra. However, Figure 3 and Table 2 suggest the following general, qualitative conclusions. A comparison of models 2b and 4b with 2a = 4a shows that including high terms in the Balmer series and the CaII H line in the active-region models lowers the estimated optical depths in the hydrogen lines appreciably, the electron temperature in the active regions slightly, and the upper boundary of the region of hydrogen radiation substantially. If the observed line radiation has a substantial contribution from microflares, then (in models 2d and 4d) the electron temperature is further decreased appreciably, the upper boundary of the region of hydrogen radiation raised slightly, and the extent of the temperature plateau narrowed appreciably. Significant lowering of the active-region temperature results in a substantial decrease in the electron density n_e due to the decrease in the degree of ionization, and the fairly complex dependence $\log n_e(\log m)$ is determined by the action of two competing factors: the growth in the temperature, which increases the degree of ionization by three orders of magnitude, right to unity, and the decrease in the total density with height in the atmosphere.

Finally, we note that the models for the quiescent states of the uniform chromospheres of YZ CMi [3] and AD Leo [4] for temperatures lower than 10 000 K are located in the strips in the (T_e, $\log m$) and ($\log n_e$, $\log m$) planes that are occupied by our calculated models. The closeness of the uniform-chromosphere model for AD Leo obtained by Mauas and Falchi [4] and our own active-region models for EV Lac can be associated with a lower contribution of microflares for the spectrum of AD Leo, as is expected, since the flare-detection rate for this star is a factor of two to three lower than for EV Lac.

4. MODELING THE SPECTRA OF THE FLARE OF EV LAC ON AUGUST 30, 1994, AT UT 23:19

To analyze the flare emission, we used the spectrogram obtained at UT 23:16–23:19, which includes the onset and maximum of this rapid flare; averaging over this interval, $\langle \Delta U \rangle = 0^m.23$, $\langle \Delta B \rangle = 0^m.03$, and $\langle \Delta V \rangle = 0^m.01$. We initially modeled the flare at UT 23:19 assuming flare radiation together with active-region emission described by a model that was close to 2d or 4d.

When modeling the flare, we must explain not only the line profile and intensity but also the additional emission in the UBV broad photometric bands, which is due virtually entirely to flaring of the continuum. It is possible to achieve agreement of all the considered parameters of the flare emission due to the different dependences of these parameters on the physical characteristics of the flares. For example, the Balner line emission is increased when the temperature in the chromosphere is increased, but the continuum emission also rises when the temperature increase is sufficiently high. Beginning with some level, the continuum grows as rapidly as the line emission, and the temperature growth ceases to influence the relative intensities $I_\lambda/I_{\rm cont}$. Further increase in the line intensity can be achieved by increasing the density, but the continuum also grows in this case. The relationship between the flare amplitudes ΔU, ΔB, and ΔV depends on the temperature at and above the temperature plateau and on the extent of this plateau: the ratio $\Delta U/\Delta B$ decreases with growth in the temperature at the plateau and decrease in the temperature above the plateau. We applied all this reasoning while fitting the models to the observations.

Figure 5a presents the line profiles obtained for UT 23:16–23:19 (solid curves) and UT 21:05–21:20 (dashed curves). During the flare, the H_α, H_γ, H_δ, and, especially, CaII H emission was strengthened relative to the corresponding emission during the quiescent state of the star, while, in contrast, the H_β was even slightly weakened. This weakening could be eliminated if we include a modest increase in the continuum during the flare. The lack of increased emission in this line is associated with the decay by the onset of the flare of the microflare or microflares that made the largest contribution to the emission of this line during the quiescent state. As we can see in Fig. 5a, the maximum equivalent width during the flare is possessed by H_δ, i.e., by a higher line in the Balmer series than in the quiescent state.

We were not able to obtain a good fit to the observed parameters of the line profiles and continuum using a single flare, and only a sum of the emission of three flares with different temperatures, densities, and extents for the temperature plateau yielded acceptable agreement. The best fit that we were able to achieve is shown in Fig. 5b: the calculated profiles (dashed) are the result of summing the active-region emission with the emission of three flares. The calculated flare models are presented in Fig. 6 and Table 3. As in

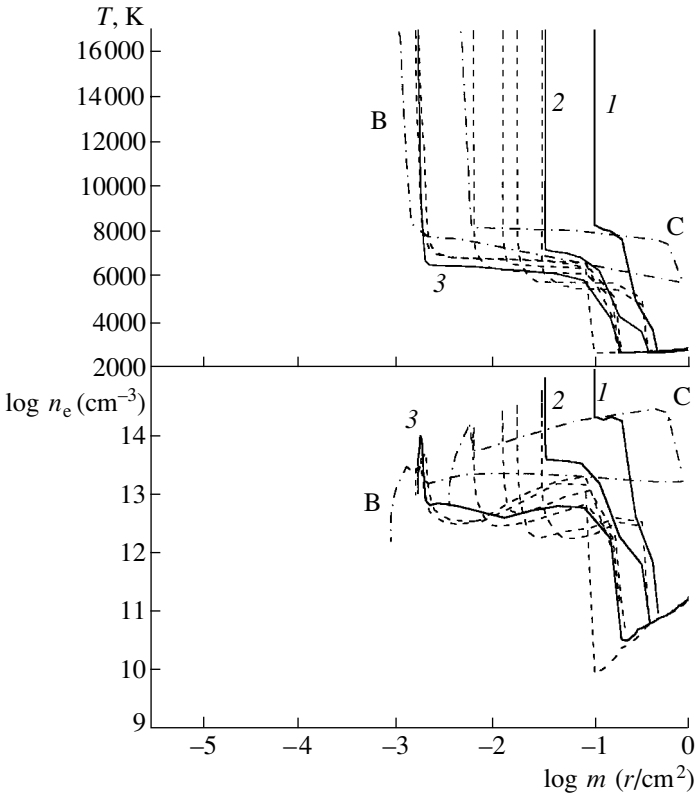

Fig. 6. Semiempirical models for flares on red dwarfs: the models of Mauas and Falchi [15] for two times during the decay phase of a strong flare on AD Leo (dot-dashed), and the flares of EV Lac considered in [7] (dotted) and on August 30, 1994 at UT 23:19 (solid).

Table 2, the ranges for physical parameters of the regions giving rise to 80% of the H_β flux are indicated in Table 3. In Fig. 6, the dot-dashed curves B and C show the calculation results of Mauas and Falchi [15] for two times during a strong flare of AD Leo, the dashed curves show our models for the active state of EV Lac according to [7], and the solid curves *1*, *2*, and *3* show the models for the flare of EV Lac of August 30, 1994 at UT 23:19. A comparison of the flare models shows that models 2 and 3 for August 30, 1994 are very close to the models of [7], while model 1, which is the strongest and makes the dominant contribution to the line wings and continuum, has a deeper and hotter temperature plateau. The electron densities in the calculated flare models are, on average, two orders of magnitude higher than the densities of the active regions discussed above.

In spite of its multicomponent nature, the fit to the observed flare spectrum in Fig. 5b is less successful than the fits of the spectra for the quiescent state of the star in Figs. 2 and 4. This may be due to the fact that even a set of three hydrostatic, stationary flare models is insufficient to reproduce the appreciably nonstationary, impulsive flare emission.

The model for the active regions during the flare is shown in Fig. 3 by the dashed curve with asterisks, denoted F. At first, the F curve is very close to models 2d and 4d, but, beginning with some depth, the temperature and therefore the electron density of this model becomes substantially higher than in the quiescent-state active regions. Our calculations indicate that the contribution of the active-region emission to the total H_β emission is 50%, which is more than twice the corresponding contribution in the quiescent state. It is possible that this is because the entire active-region area is activated during the flare, so that the number of microflares grows along with the occurrence of the individually detectable larger flares. Our active-region models probably represent some average of substantially inhomogeneous structures.

5. CHARACTERISTICS OF MICROFLARES

The term "microflare" refers to eruptive phenomena that are not accessible to direct detection, whose existence can be deduced only via various statistical properties of the nonstationary objects. Since the detection limit for individual flares depends appreciably on the region of the spectrum considered, the absolute brightness of the source, and the sensitivity of the

Table 3. Models of flares of EV Lac

Spectrogram of UT 23:16–23:19				
Parameter	Active regions	Flare 1	Flare 2	Flare 3
S, %	22	0.01	0.06	0.22
$\log m$ (g/cm^2)	−4.6...−3.4	−0.9...−0.7	−1.4...−0.8	−2.8...−1.1
$\log n_e$ (cm^{-3})	10.9–11.5	15.0–14.5	14.7–13.0	13.6–12.7
$\log n_H$ (cm^{-3})	12.3–13.3	15.0–15.5	14.7–16.1	13.6–15.9
T_e, K	11 500–6670	15 000–7200	14 500–6100	13 500–6000

$\Delta U = 0\overset{m}{.}25$, $\Delta B = 0\overset{m}{.}023$, $\Delta V = 0\overset{m}{.}005$

$(W_{\rm ar} : W_{\rm f1} : W_{\rm f2} : W_{\rm f3})_{\rm H\beta} = 50 : 25 : 20 : 5$

Line	$W_\lambda^{\rm meas}$, Å	$\Sigma W_\lambda^{\rm calc}$, Å	$\tau_{\rm ar}$	$\tau_{\rm f1}$	$\tau_{\rm f2}$	$\tau_{\rm f3}$
H_α	6.9	5.1	16	4×10^4	3×10^3	650
H_β	5.8	8.1	2.2	6×10^3	480	91
H_γ	8.0	9.5	0.75	2×10^3	160	31
H_δ	13	9.8	0.35	910	76	14
H_ε	5.5	9.3	0.19	510	42	8
H CaII	10	15	2×10^4	7×10^4	7×10^4	5×10^4
$I_{\rm H\beta}$, 10^6 erg cm^{-2} s^{-1} ster^{-1} Å			0.7	70	64	24

instruments used, the characteristic energies for different microflares could differ by orders of magnitude. For example, analyzing the soft X-ray radiation of UV Cet, EQ Peg, and Proxima Cen outside of flares, Butler and Rodonó [16] found fine structure that they called microflares, with characteristic time scales of about 20 s and energies of $E_X \sim 2 \times 10^{30}$ erg, while solar microflares in the ultraviolet are characterized by energies of about 10^{27} erg. Further, Butler *et al.* [17] detected a linear correlation between the total energies $E_{\rm H\gamma}$ and E_X that was the same for stellar and solar flares and covered four orders of magnitude; Mathioudakis and Doyle [18] continued this correlation to the quiescent state of active M dwarfs, leading to the conclusion that microflares make the dominant contribution to the "quiescent" emission of active stars in the H_γ line.

Linsky and Wood [19] associated the broad wings of the SiIV and CIV lines of the transition region in the spectrum of AU Mic detected with the Hubble Space Telescope with microflares. Further, substantial contributions of microflares to these lines—10–40% of the line flux outside of individually detectable flares—were deduced in the spectra of α Cen A, AD Leo, LQ Hya, and EK Dra using fast spectrophotometric HST measurements [20–22].

Apparently, we now have the first opportunity to estimate the main characteristics of microflares and constructure models for these events in the optical, based on the emission of the dominant radiating elements—hydrogen and calcium.

A comparison of the corresponding quantities in Tables 2, 3, and 4 and in Figs. 3, 6, and 7 shows similarity of the parameters of the flares and microflares and substantial differences between the characteristics of active regions and microflares. On average, microflares occur at depths that exceed the depths of the active regions by a factor of 100 (according to the parameter m) and have characteristic electron densities that likewise exceed those in active regions by two orders of magnitude. The largest differences between microflares and active regions occur in models 2d, 4d, and F, where three flare events were included in the modeling. The optical depths in the H_α line are, on average, several tens for both types of structure.

It follows from Figs. 6 and 7 that the flares at UT 23:16–23:19 have temperatures that exceed the temperatures of microflares by 2000–3000 K, while

Table 4. Models of microflares of EV Lac

Parameter	Model 2c	Model 2d		
		Microflare 1	Microflare 2	Microflare 3
Spectrogram of UT 21:05–21:20				
S, %	0.9	0.1	1.1	0.2
$\log m$ (g/cm^2)	−1.57...−1.53	−1.14...−1.13	−1.87...−1.74	−1.16...−1.15
$\log n_e$ (cm^{-3})	14.4–12.1	15.0–12.6	14.2–11.8	14.8–12.6
$\log n_{\rm H}$ (cm^{-3})	14.6–15.2	15.0–15.5	14.3–14.8	15.1–15.7
T_e, K	10200–5100	14 000–6000	11 000–5100	10 700–6000
Line	τ	τ	τ	τ
H_α	19	54	18	15
H_β	2.7	7.8	2.6	2.0
H_γ	0.93	2.7	0.88	0.70
H_δ	0.44	1.3	0.41	0.32
H_ε	0.24	0.70	0.23	0.18
H CaII	4×10^4	7×10^4	4×10^4	3×10^4
$I_{H\beta}$, 10^6 erg cm^{-2} s^{-1} ster^{-1} Å	26	38	20	5.5
Spectrogram of UT 23:35–23:50				
Parameter	Model 4c	Model 4d		
		Microflare 1	Microflare 2	Microflare 3
S, %	0.6	0.02	1.0	0.6
$\log m$ (g/cm^2)	−1.57...−1.53	−0.74...−0.70	−1.57...−1.50	−3.4...−2.2
$\log n_e$ (cm^{-3})	14.4–12.1	15.4–12.3	14.5–12.1	12.9–12.3
$\log n_{\rm H}$ (cm^{-3})	14.6–15.2	15.4–16.1	14.5–15.3	12.9–14.8
T_e, K	10 200–5100	14 400–4600	11 000–5000	10 500–6000
Line	τ	τ	τ	τ
H_α	19	170	18	100
H_β	2.7	25	2.6	14
H_γ	0.93	8.4	0.88	4.7
H_δ	0.44	4.0	0.41	2.2
H_ε	0.24	2.2	0.23	1.2
H CaII	4×10^4	7×10^4	3×10^4	3×10^4
$I_{H\beta}$, 10^6 erg cm^{-2} s^{-1} ster^{-1} Å	26	52	20	5.7

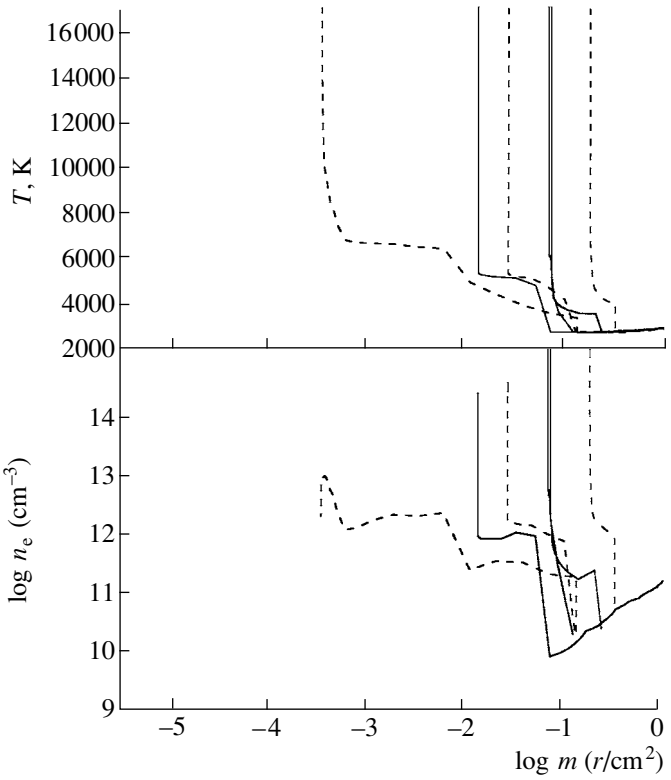

Fig. 7. Semiempirical models for microflares of EV Lac on August 30, 1994: the solid curve shows model 2d for UT 21:05–21:20 and the dashed curve model 4d for UT 23:35–23:50.

the regions of flares and microflares overlap in depth. In other words, there is strong heating of the stellar atmosphere in flares.

6. CONCLUSIONS

Our use of high-quality observational material—echelle spectrograms with high spectral resolution over the entire wavelength range considered combined with $UBVRI$ photometry—necessitated the introduction of an even more nonuniform source of chromospheric emission in EV Lac than in the models of [6]. Namely, the observations require the presence of permanently present microflares that are virtually undetectable photometrically but nevertheless make the dominant contribution to the Balmer-line emission. We have constructed the first semiempirical models of these structures, which reveal appreciable similarities to models for individual detectable flares but substantial differences from models for active regions. In our microflare models, the electron density is enhanced by two orders of magnitude compared to the values for active regions, and the temperature plateau is shifted further toward deep layers in the atmosphere.

The microflares have significant emission in the U band, but, due to their small dimensions, their contribution to the total U brightness usually does not exceed $0^m.02$. With such mean microflare amplitudes, a star with apparent magnitude $U = 12^m.9$ at a distance of 5.13 pc radiates an additional energy in the U band of about 1×10^{30} erg in 15 min, which corresponds to an average, detectable solar flare. Let us consider the place of events with such energies in the overall ensemble of flare phenomena on EV Lac, turning to their energy spectrum.

According to Gershberg and Shakhovskiĭ [23], the cumulative energy spectrum for flares on EV Lac in the U band constructed from individually detectable events has the form

$$\log \tilde{\nu} = 26.76 \pm 0.05 - (0.89 \pm 0.06) \log E_U \quad (1)$$

or

$$\tilde{\nu} = 1.15(E_U/10^{30})^{-0.89}, \quad (2)$$

where $\tilde{\nu}$ is the cumulative frequency of flares with energy exceeding 10^{30} erg in inverse hours and E_U is the total energy of a flare in ergs. The mean flare rate ν is related to their cumulative frequency $\tilde{\nu}$ by the expression

$$\nu = -d\tilde{\nu}/d(E_U/10^{30}) = 1.02(E_U/10^{30})^{-1.89}. \quad (3)$$

As can be seen in Fig. 2b of [23], the spectrum $\tilde{\nu}(E_U)$ constructed from observations of individual

flares includes only events with $E_U > 10^{31}$ erg. Let us neglect differences in the energies of the three microflares whose presence we deduced; i.e., we will consider each of them to have energy $E_U = 10^{30}/3$ erg. Then, according to (3), $\nu(10^{30}/3) = 8.2\ \mathrm{h\,rs}^{-1}$; i.e., flares with such energies should occur, on average, every 7.4 min. This rate is consistent with Fig. 1, where we can see appreciable variations in the equivalent widths of emission lines when the data are averaged over intervals of 15 min. In other words, the microflares represent a natural low-energy continuation of the ensemble of flares on EV Lac used to construct the flare energy spectrum in [23].

All this suggests that the microflares we have indirectly detected do not represent qualitatively new phenomena: they are physically identical to individually detectable flares and differ only in their lower total energy. Since these microflares belong to an ensemble of flares whose cumulative energy spectrum has a spectral index smaller than unity, they contain overall less energy than the more powerful individually detectable events and consequently cannot be the main sources of heating in the stellar atmosphere.

Finally, we have represented a noncontinuous, impulsive flare with a set of three different hydrostatic models that together can explain certain differences between the observed flare spectrum and the spectra of the star in its quiescent state: the presence of broad line wings, the flare continuum, and the shift of the maximum equivalent width to the H_δ line.

7. ACKNOWLEDGMENTS

This work was carried out using the Nordic Optical Telescope, which is operated and used jointly by Denmark, Finland, Iceland, Norway, and Sweden and is located on the island of La Palma at the Observatory del Roque de los Muchachos of the Instituto de Astrofísica de Canarias. The work of I.Yu.A. and R.E.G. was partially supported by DFFD contract 02/0700300. We thank E.I. Zhigalkina for help in preparing the figures for publication.

REFERENCES

1. R. Kandel, Ann. Astrophys. **30**, 999 (1967).
2. W. L. Kelch, J. L. Linsky, and S. P. Worden, Astrophys. J. **229**, 700 (1979).
3. M. S. Giampapa, S. P. Worden, and J. L. Linsky, Astrophys. J. **258**, 740 (1982).
4. P. J. D. Mauas and A. Falchi, Astron. Astrophys. **281**, 129 (1994).
5. D. Jevremovic, J. G. Doyle, and C. J. Butler, in *Proc. 11th Cambridge Workshop on Cool Stars, Stellar Systems, and the Sun*, Ed. by R. J. Garcia Lopez, R. Rebolo, and M. R. Zapatero Osorio, Astron. Soc. Pac. Conf. Ser. **223**, 815 (2001).
6. E. A. Baranovskiĭ, R. E. Gershberg, and D. N. Shakhovskoĭ, Astron. Zh. **78** (1), 78 (2001) [Astron. Rep. **45**, 67 (2001)].
7. E. A. Baranovskiĭ, R. E. Gershberg, and D. N. Shakhovskoĭ, Astron. Zh. **78** (4), 359 (2001) [Astron. Rep. **45**, 309 (2001)].
8. E. P. Abranin, I. Yu. Alekseev, S. Avgoloupis, *et al.*, Astron. Astrophys. Trans. **17**, 221 (1998).
9. E. A. Baranovskiĭ, E. V. Malanushenko, and A. V. Shumko, Astron. Zh. **74**, 454 (1997) [Astron. Rep. **41**, 399 (1997)].
10. V. G. Lozitskiĭ and E. A. Baranovskiĭ, Izv. Krym. Astrofiz. Obs. **88**, 67 (1993).
11. I. Tuominen, I. V. Ilyin, and P. P. Petrov, in *Astrophysics with the NOT*, Ed. by H. Karttunen and V. Piirola (Univ. of Turku, 1999), p. 47.
12. I. V. Ilyin, Licentiate dissertation (University of Oulu, 1996).
13. I. Yu. Alekseev, Astron. Zh. **73**, 81 (1996) [Astron. Rep. **40**, 69 (1996)].
14. B. W. Bopp, Mon. Not. R. Astron. Soc. **168**, 255 (1974).
15. P. J. D. Mauas and A. Falchi, Astron. Astrophys. **310**, 245 (1996).
16. C. J. Butler and M. Rodonó, Ir. Astron. J. **17**, 131 (1985).
17. C. J. Butler, M. Rodonó, and B. H. Foing, Astron. Astrophys. **206**, L1 (1988).
18. M. Mathioudakis and J. G. Doyle, Astron. Astrophys. **240**, 357 (1990).
19. J. L. Linsky and B. E. Wood, Astrophys. J. **430**, 342 (1994).
20. B. E. Wood, J. L. Linsky, and T. R. Ayres, Astrophys. J. **478**, 745 (1997).
21. S. H. Saar, M. R. Morgan, J. A. Bookbinder, *et al.*, in *Cool Stars, Stellar Systems, and the Sun*, Ed. by J.-P. Caillault, Astron. Soc. Pac. Conf. Ser. **64**, 471 (1994).
22. S. H. Saar and J. A. Bookbinder, in *Proc. Tenth Cambridge Workshop on Cool Stars, Stellar Systems, and the Sun*, Ed. by R. A. Donahue and J. A. Bookbinder, Astron. Soc. Pac. Conf. Ser. **154**, 1560 (1998).
23. R. E. Gershberg and N. I. Shakhovskaya, Astrophys. Space Sci. **95**, 235 (1983).

Translated by D. Gabuzda

Astronomy Reports, Vol. 47, No. 4, 2003, pp. 326–332. Translated from Astronomicheskiĭ Zhurnal, Vol. 80, No. 4, 2003, pp. 357–363.

Triplet Spectra of H_2O Masers and Protoplanetary Disks

E. E. Lekht[1,2] and A. M. S. Richards[3]

[1] *Instituto Nacional de Astrofísica, Óptica y Electrónica, Luis Enrique Erro No. 1, Apdo Postal 51 y 216, Tonantzintla, Puebla, 72840 Mexico*

[2] *Sternberg Astronomical Institute, Universitetskiĭ pr. 13, Moscow, 119992 Russia*

[3] *Jodrell Bank Observatory, Macclesfield, Cheshire, SK11 9DL United Kingdom*

e-mail: lekht@inaoep.mx

Received July 15, 2002; in final form, October 10, 2002

Abstract—An analysis of the H_2O maser emission associated with protoplanetary disks is presented. Triplet H_2O spectra can be formed at certain stages in the evolution of Keplerian disks. The dependence of the mass of the central star in the Keplerian disk on the disk radius is derived. The calculations are based on the distribution of the water-vapor molecules (maser spots). In S140, the observed elongated maser spots (chains) with a smoothly varying line-of-sight velocity are interpreted as protoplanetary structures with a small intrinsic rotation. © *2003 MAIK "Nauka/Interperiodica"*.

1. INTRODUCTION

A group of spectra with triplet structures can be selected from the wide variety of H_2O maser spectra associated with sources in star-forming regions. These are of special interest because such spectra can be formed in a Keplerian disk observed edge-on. Cesaroni [1] was the first to draw attention to this. The main criteria used to choose a model for the S255 maser and determine its parameters were the detected anticorrelation between the fluxes of the lateral triplet components and the observed doublet structure for the red component. The S140 maser was likewise identified with a Keplerian disk on the basis of such triplet structure and anticorrelations, as well as sinusoidal variability of the radial velocities of the components [2]. For some clumps of material, the parameters of their orbital motions were calculated.

Pashchenko *et al.* [3, 4] have shown that the H_2O spectrum of S255, considered to be a classical triplet in 1987–1989 [1], was fairly complex in other periods of its evolution, consisting of a large number of components. Long-term monitoring of another Keplerian disk candidate, S269, has shown that the triplet structure is likewise not permanent [5]. From time to time, emission features can appear either between or outside lateral triplet components, sometimes at considerable distances from them.

High-angular-resolution observations of NGC 2071 and W75N have shown that one group of maser spots in each source forms an ellipse with a more or less regular spot-to-spot distribution of radial velocities; the ellipses have sizes (semimajor axes) of about 20 and 200 AU, respectively. The derived parameters of the maser emission regions provide evidence for Keplerian disks [6, 7]. A protoplanetary disk has also been detected in IC 1396N [8].

Groups of maser-spot chains have been observed in S140 [9]. It is thought that some groups could be associated with protostars. The estimated disk radius for one of the groups is 60 AU; the extent of the chains is from $\sim$0.3 to 1.2 AU.

Studies of the Orion KL H_2O maser have also detected highly organized structures in the form of chains of compact components [10]. The estimated component sizes are $\sim$ 0.1 AU. Matveenko *et al.* [10] have suggested that the formation of protostars is accompanied by accretion disks and bipolar outflows, followed by maser emission in the water-vapor line.

Thus, the appearance of the H_2O maser emission spectra varies strongly with time, from being simple (2–3 components) to rather complex (large numbers of components). Triplet spectral structure has been observed not only for single emission features but also for groups of features with close radial velocities (for example, S255 [3, 4]). This testifies that the associated Keplerian disks may be very nonuniform.

The variation of the structure of the H_2O spectrum could be related to changing activity of the star. As Yorke and Krügel [12] and Tutukov and Shustov [13] have shown, the accretion of material onto a star is not stationary, and the stellar luminosity can vary over periods of 4–10 years. Matveenko *et al.* [10] have suggested that precession of accretion disk rings could also lead to considerable variations of the maser emission.

1063-7729/03/4704-0326$24.00

The current paper considers triplet H_2O spectra and their relation to protoplanetary disks. We have used observational data published earlier, as well as our subsequent observations.

2. OBSERVATIONAL DATA

Most information about the early stages of star formation comes from observations of maser emission, mainly H_2O emission at $\lambda = 1.35$ cm. Long-term monitoring of masers has great importance and has made it possible to find triplet spectra and trace their evolution. The detection of anticorrelations of the fluxes of the triplet components and radial-velocity drifts of individual emission features have become arguments in support of Keplerian disk models. The protoplanetary disk parameters and central star masses have been calculated for some such masers (S140 and S255). The stellar masses of other sources have also been estimated, but they have a different type of structure—expanding envelopes—and we do not consider these data here.

High-angular-resolution observations have shown that maser spots form primarily two kinds of distributions: elongated chains and ellipses. The former structure is identified with bipolar outflows, while the latter is associated with protoplanetary disks or expanding envelopes rotating around the central star. We wish to select masers that are identified only with protoplanetary disks. In these disks, the individual triplet components represent elongated chains of maser spots with smoothly varying line-of-sight velocities.

VLBI observations have directly determined the angular sizes of the maser-emission region (protoplanetary disk) in a number of sources: Orion KL (two of the eight maser spot groups), S140(2), NGC 2071 (IRS 1), IC 1396N, and W75N (VLA2). The VLBI observations were carried out mostly at low maser activity levels, so that we do not have a complete picture of the disk structure of some sources.

Figure 1 presents our previously unpublished H_2O spectra of the S140 maser from monitoring in 1999–2002. The vertical arrow shows the scale in Janskys, and the horizontal axis is the radial velocity relative to the Local Standard of Rest.

Figure 2a shows the average spectrum of S140 for January 2000–March 2001. The arrows in Fig. 2b denote the positions of the emission peaks for various time intervals. The horizontal lines show the radial-velocity intervals in which maser emission was observed.

Figure 3 shows the Keplerian disk radius as a function of the mass of the central star. The open circle is the point for the Solar System (see Section 4). The cross marks a limiting case for the Orion maser [10]. The smooth fitted curve is dashed, and the dotted curve is a Lorentz profile.

3. INDIVIDUAL SOURCES

3.1. S140

Richards *et al.* [9] found three groups of maser spots in S140, each of which could in principle have its own activity center. Our single-dish monitoring yields the integrated spectrum of these features.

Before 1994, the maser had a large intensity (up to 3000 Jy) and a pronounced triplet structure. The flux anticorrelation was present, as well as radial-velocity drifts for all three triplet components. Weak emission features appeared seldom; for instance, features with fluxes of several Janskys were observed in 1982–1983 at velocities of $-(8–6)$ km/s, which are not standard for the triplet.

There are good reasons to suppose that the observed intense triplet emission belonged to one of the three groups of features. A comparison of the spectra of these groups [9] with our monitoring spectra indicates that the strong maser emission was probably associated with groups of spots having the coordinates RA $= 22^h17^m41\overset{s}{.}1085$, DEC $= 63°03'41\overset{''}{.}470$ (1950).

We denote this region S140(1). Upper limits for the disk radius and stellar mass for this region (80 AU and $5M_\odot$, respectively) were derived from the variations of the radial velocity of the central component [2]. We have used this limiting radius when plotting Fig. 4. The chains detected in this region have a radial-velocity dispersion of $\sim$2 km/s. In the Keplerian disk model [2], this corresponds to an extent of the maser-emission region along the radius or ring that is almost an order of magnitude larger than observed. The line profile of each chain is close to Gaussian, ruling out a superposition of emission from individual chain elements. In addition, the lines are fairly broad, from 0.83 to 0.94 km/s (at the 0.5 level). During our monitoring, the widths of single lines were much smaller, from 0.3 to 0.6 km/s.

It is most likely that the observed chains are elongated maser spots with radial-velocity gradients. They could be protoplanetary clumps whose density grows toward the center. In this case, the above-mentioned difficulty with the extent of the chain is removed.

In 1994–2001, the S140 maser was not so active as before, but emission was observed over almost the entire velocity interval from -17 to 6 km/s. In 2002, the spectrum had regained the triplet structure, though it was slightly asymmetric. The central and redshifted components consisted of several emission features. The average spectrum (January 2000–March 2001) demonstrates that the triplet structure was also present before 2002, but only for groups of features and at different radial velocities. The largest

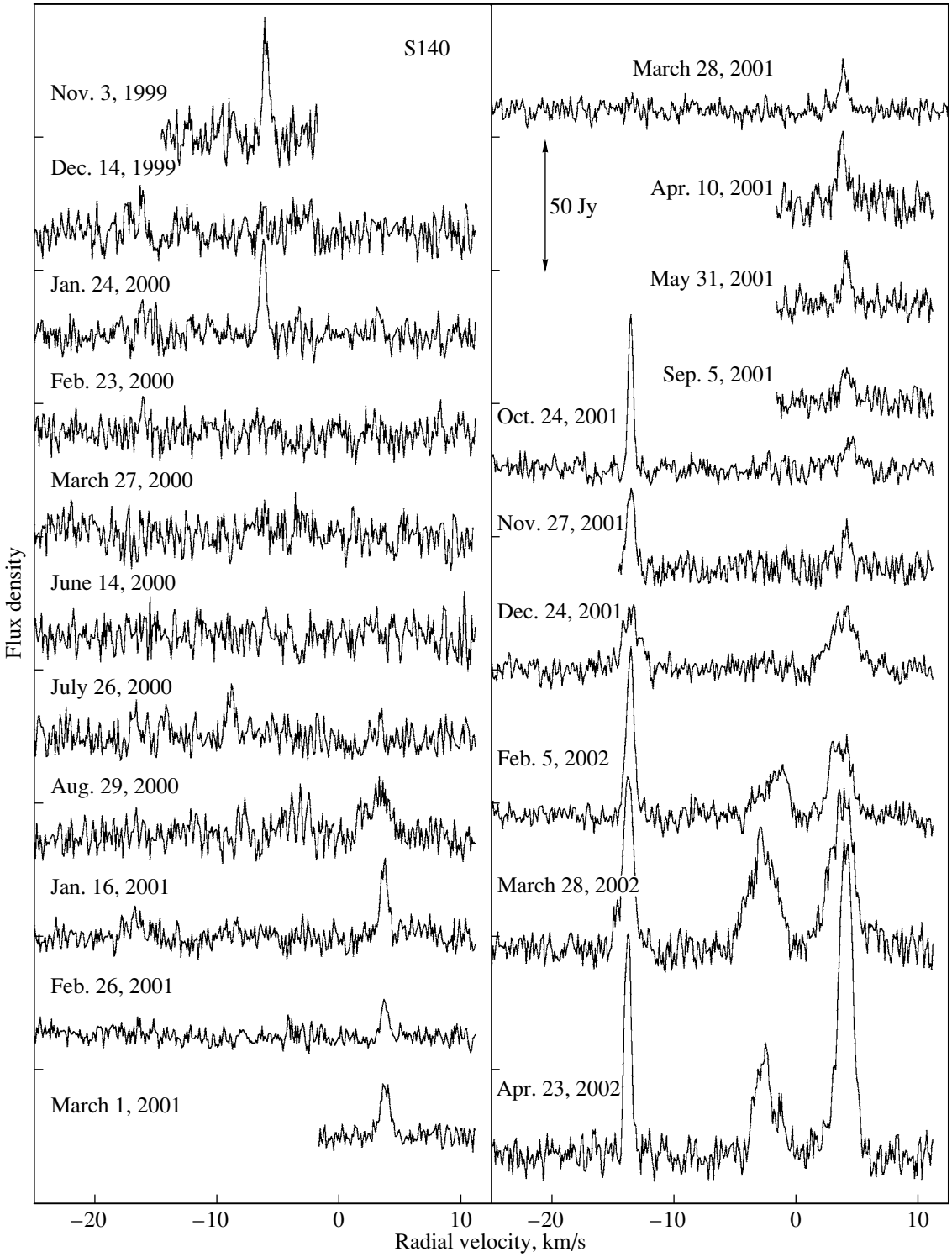

Fig. 1. The H_2O maser emission spectra of S140. The vertical arrow shows the scale.

velocity dispersion, from 5 to 11 km/s, was observed for the redshifted component.

Beginning in mid-2001, we observed a double component with a central velocity of −13.6 km/s and subcomponents separated in velocity by 0.3–0.4 km/s. Emission with a similar structure was observed in 1981–1983 at −15.2 km/s, as well as in 1990. The region of maser emission in 2001–2002 cannot be identified with any of the regions responsible for the emission at velocities from −15.4 to

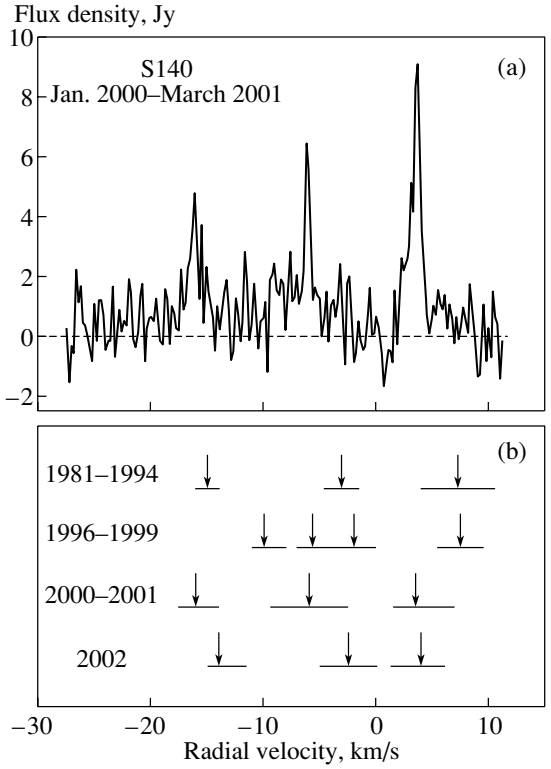

Fig. 2. Average spectrum of S140 from January 2000 to March 2001.

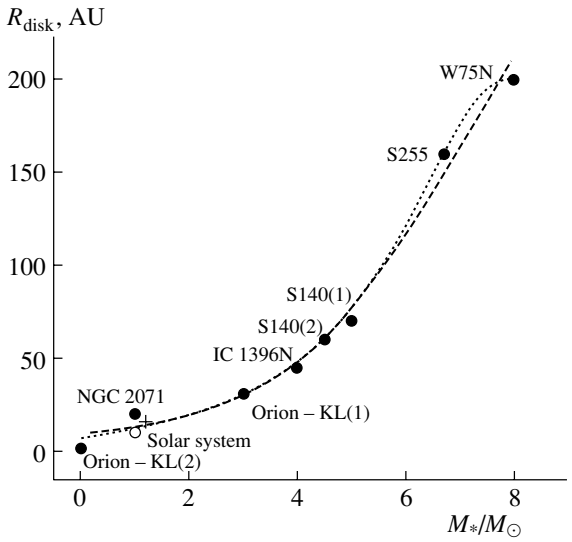

Fig. 3. Keplerian disk size as a function of the mass of the protostar as derived from H_2O maser observations (see text).

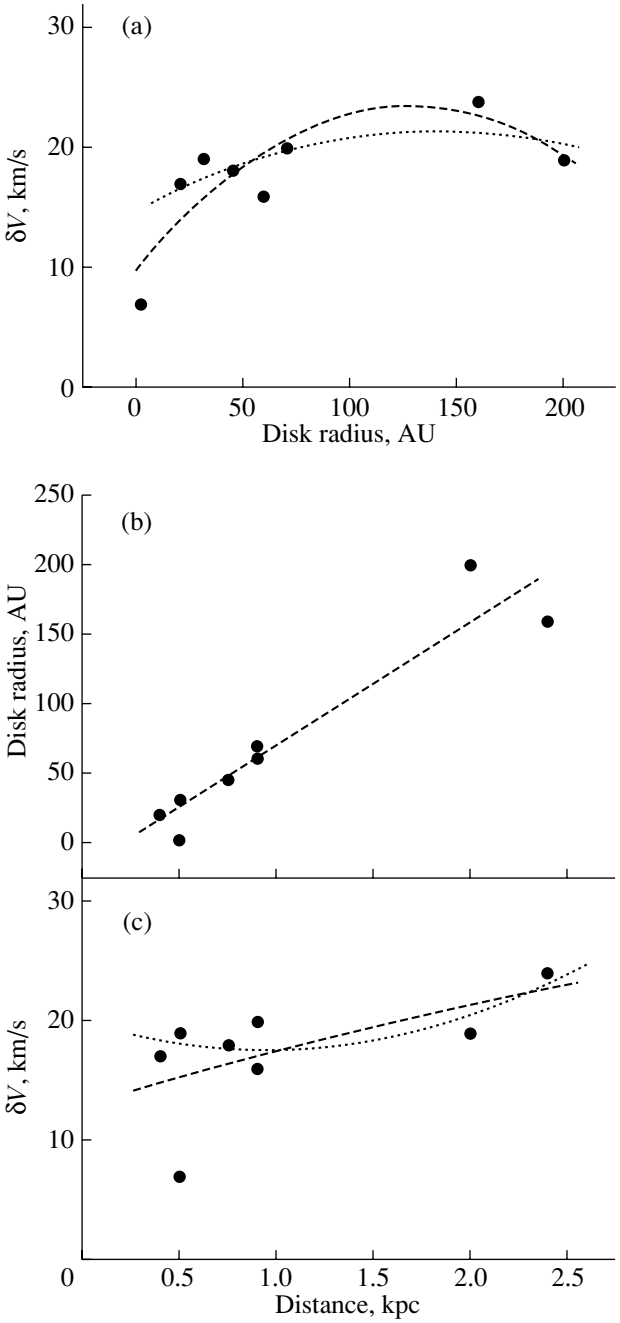

Fig. 4. Dependences between various Keplerian disk parameters.

−14 km/s before 1994. Extrapolation of the radial-velocity variations of pre-1994 components due to their orbital motion yields velocities that differ from −13.6 km/s. Furthermore, we observed no radial-velocity drift, while this drift should be no smaller than 0.8 km s^{-1} yr^{-1} [11].

The evolution of the maser emission demonstrates that, although the H_2O spectrum represents a superposition of the emission from three individual regions after 1994, it basically retains the triplet structure. These regions have no appreciable peculiar motions relative to each other; therefore, at least two of them could have triplet spectra.

According to Richards *et al.* [9], the other

Keplerian disk parameters derived from observations of H_2O masers

Source	Disk radius, AU	Mass of the star, $M_\odot$	δV, km/s	r, pc
Orion–KL (1)	31	3	19	500
Orion–KL (2)	1.7	0.007	~7	
NGC 2071	20	1	17	400
S255	160	6.7	24	2400
W75N	200	8	19	2000
S140 (1)	≤70	≤5	19	900
S140 (2)	60	4.5	16	
IC 1396N	45	4	19	750

maser-emission region has the coordinates RA = $22^h17^m26^s.703$, DEC = $63°03'33''.629$ (1950). We denote this source S140(2). This isolated region has an angular radius of 75 mas, or 60 AU for a distance to S140 of 900 pc. In the Keplerian disk model, the 2.7-km/s feature must be located in the inner part of the disk, and the lateral triplet features are the components at −18 and −2.4 km/s. We adopt −10.2 km/s for the velocity of the central star. Using the formula for Keplerian motion, we obtain a mass for the star of $\approx 4.5M_\odot$.

3.2. S255

S255 was the maser source that initiated the first studies of Keplerian disks. Its three-peaked spectrum and the anticorrelation of the fluxes of the lateral components represented a classical example of the formation of maser emission in a Keplerian disk.

Our long-term monitoring of the S255 maser shows a persistent triplet structure in the H_2O spectra [4]. During periods of high maser activity, the spectra consisted of three groups of central and lateral emission features. The recurrence of the H_2O spectrum triplet structure is important evidence for a nonuniform Keplerian disk.

The disk size and protostar mass in S255 were derived from an analysis of the time variations of the maser emission of individual components [4]. We obtained about 160 AU for the outer disk radius. Based on an analysis of the radial-velocity drifts of the three components, we obtained masses of $(6–7)M_\odot$. We will adopt the average stellar mass of $6.7M_\odot$.

3.3. The Maser in Orion KL

According to Matveenko *et al.* [10], powerful compact maser sources in the Orion Nebula are distributed in eight active regions. Two of these contain chains of compact components and an elliptical structure. The disruption of the triplet structure of the spectra of a region that underwent a powerful flare is explained by the approximately hundredfold amplification of only some emission features in a molecular cloud. The absence of triplet structure has somewhat hampered estimation of the velocity dispersion. However, the mass of the protostar ($3M_\odot$) was estimated from an analysis of the spectra and the probable peculiar velocity of the maser-emission region and molecular cloud. We adopt the maximum value 31 AU for the disk radius. In addition, Matveenko *et al.* [10] considered a limiting case for the system's velocity. We will use the values for the stellar mass and disk radius obtained for this limiting case: $M = 1.2M_\odot$ and $R = 16$ AU.

The other elliptical region has a fairly small size and protostar mass. The extent of this region may be limited by the fourth ring. In this case, $R \sim 7$ AU. The mass of the protostar does not exceed $0.007M_\odot$.

3.4. Other Sources

In spite of the fact that the W75N H_2O maser has a fairly developed spectral structure, the spectrum showed a triplet structure for groups of features in some time intervals. On this basis, a possible model of the maser as a Keplerian disk was proposed [13]. Torrelles *et al.* [7] have found two groups of maser spots in this region, one of which is compact and forms a shell around a radio continuum source. The shell radius is about 200 AU. The mass of the central star was estimated to be $\approx 8M_\odot$ based on the radial-velocity dispersion about the average velocity.

A considerably smaller disk was found in NGC 2071 [6]. For a distance of 400 pc, the disk radius is 20 AU and the mass is $\approx M_\odot$.

Another method was used to determine M and R for the maser in IC 1376N [8]. The detected compact group of sources has a radial-velocity gradient, leading to the consideration of protoplanetary disk models. The stellar mass was estimated from the bolometric luminosity of the infrared source IRS2 ($4M_\odot$). The disk radius is 45 AU.

4. PROTOSTAR MASS AND KEPLERIAN DISK RADIUS

The data on all the sources are listed in the Table, which presents the (1) names of the maser sources, (2) outer radius of the protoplanetary disk in AU,

(3) mass of the central star in solar masses, (4) radial-velocity dispersion (δV) for the H_2O maser emission, and (5) distance to the source in parsecs. Here, by the radial-velocity dispersion, we mean the difference of the radial velocities of the lateral components of the triplet spectrum. In the case of S140, the disk radius derived from the variability of the velocity of the central component was larger than the radius found using the blueshifted component. For this reason, the value of δV was decreased to 20 km/s.

Figure 3 plots the data of the Table. We have added a point for the solar system as a Keplerian disk in the initial stage of its evolution. We adopted ~ 10 AU for the outer radius, slightly greater than the distance from the Sun to Saturn. The dashed curve shows the fitted polynomial. In all cases, the disk size corresponds to the radius where the density remains sufficient to create the required line-of-sight optical depth for water vapor molecules. For this reason, we have not adopted the maximum radius of the solar system and have limited our consideration to Saturn's orbit. Although the density at Saturn's orbit was less than at Jupiter's orbit, water vapor molecules could be blown out by the stellar wind and light pressure. As a result, the outer part of the disk (at Saturn's orbit) could contain a sufficient number of masing water molecules. Possible pumping sources include the stellar wind, IR emission, and material falling onto the accretion disk from the surrounding medium.

The dashed fitted curve describes the relationship between the disk diameter and mass of the protostar fairly well. Again, we note that the points on this plot have been obtained using different methods: from long-term monitoring of H_2O masers and from VLBI observations. The points for Orion KL (2) and NGC 2071 stand out somewhat. The source in Orion KL (2) may be fairly young, so that the accretion of material onto the star is important. In addition, the system could be unstable. Matveenko *et al*. [10] do not rule out the possibility of stellar-wind-driven expansion of the ring structure in this source. If this object is fairly young, the disk parameters could change in the course of its evolution, and the mass of the protostar could increase. For instance, with an expansion velocity of 0.64 km/s [10], the disk radius could double in ~ 15 years.

The derived relationship is best described by a Lorentz profile (dashed). This is physically meaningful. The molecular disk around an already formed star cannot have an unlimited radius. Furthermore, we must take into account the fact that we have estimated the radii from the distribution of water-maser emission regions. In the case of a large disk, the density of matter (in particular, of water-vapor molecules) will strongly decrease, and the column density of coherent water-vapor molecules will not be sufficient. Indeed, as we can see from the plot, there is a cutoff at a disk radius of about 200 AU (a stellar mass of $\sim 8 M_\odot$).

We have also attempted to find correlations between other parameters of the Keplerian disks. Figure 4 presents plots constructed using the data of the Table. The dashed curves show fitted second-order polynomials. Since one point clearly stands apart, it was not included when deriving the dotted curves. We can clearly see in Fig. 4a that δV varies only slightly, and depends only weakly on R. The weak R dependence can be explained by the fact that R and M_* are already related by a functional relationship (Fig. 3). Nevertheless, we can estimate that δV in the Keplerian disk has a maximum value of 23 km/s for a disk radius of ~ 130 AU.

In the middle plot, we can trace a linear dependence of the disk radius on the distance to the source, with a coefficient of proportionality of about two. The existence of such a relationship seems unlikely to us, and it is probably due to selection effects. This appears to be confirmed by the lack of a correlation between the velocity dispersion and the source distance (Fig. 4c).

Thus, we can suppose that a star of mass M_i with a protoplanetary disk of radius R_i is formed from a molecular cloud of some mass, with M_i and R_i related as shown in Fig. 3. In addition, the size of the protoplanetary disk is probably limited.

5. CONCLUSIONS

(1) Some maser sources display a triplet structure in their H_2O spectra at certain stages of their evolution.

(2) Triplet structure can appear at certain phases in the evolution of a Keplerian disk, most likely in the initial stage, when the disk is not very nonuniform. In the case of strongly fragmented disks, the triplet structure occurs for groups of features.

(3) Evidence for Keplerian disks can include

—the arrangement of maser spots in an ellipse (the maser is observed almost edge-on), with an ordered distribution of line-of-sight velocities;

—triplet structure of the H_2O spectrum persistent during many years;

—velocity drifts of the components, reflecting the Keplerian motion of clumps of material in the field of the central star;

—anticorrelations of the fluxes of the lateral components and of the fluxes of the lateral and central components (for single emission features and groups of features);

—chains of maser spots with smooth spot-to-spot radial-velocity variations.

(4) The maser-spot chains in S140 represent elongated structures with a radial-velocity gradient and density increase toward the center. Such structure could be a protoplanetary cloud with a small intrinsic rotation relative to the center of mass.

(5) We have obtained a relationship between the mass of the protostar in the Keplerian disk and the disk radius, which is approximated well by a Lorentz profile.

ACKNOWLEDGMENTS

The RT-22 Pushchino radio telescope is supported by the Ministry of Industry and Science of the Russian Federation (registration number 01-10). The authors are grateful to the staff of the Pushchino Radio Astronomy Observatory for their great help with the observations.

REFERENCES

1. R. Cesaroni, Astron. Astrophys. **233**, 513 (1990).
2. E. E. Lekht, S. F. Likhachev, R. L. Sorochenko, and V. S. Strel'nitskiĭ, Astron. Zh. **70**, 731 (1993) [Astron. Rep. **37**, 367 (1993)].
3. M. I. Pashchenko, E. E. Lekht, and I. I. Berulis, Astron. Zh. **78**, 696 (2001) [Astron. Rep. **45**, 600 (2001)].
4. M. I. Pashchenko, E. E. Lekht, and A. M. Tolmachev, Pis'ma Astron. Zh. (in press) [Astron. Lett. (in press)].
5. E. E. Lekht, M. I. Pashchenko, and I. I. Berulis, Astron. Zh. **78**, 1081 (2001) [Astron. Rep. **45**, 949 (2001)].
6. J. M. Torrelles, J. F. Gómez, L. F. Rodríguez, *et al.*, Astrophys. J. **505**, 756 (1998).
7. J. M. Torrelles, J. F. Gómez, L. F. Rodríguez, *et al.*, Astrophys. J. **489**, 744 (1997).
8. V. I. Slysh, I. E. Val'tts, V. Migenes, *et al.*, Astrophys. J. **526**, 236 (1999).
9. A. M. S. Richards, E. E. Lekht, V. Samodurov, *et al.*, Astron. Soc. Pac. Conf. Ser. (in press).
10. L. I. Matveenko, F. D. Diamond, and D. A. Graham, Astron. Zh. **77**, 669 (2000) [Astron. Rep. **44**, 592 (2000)].
11. E. E. Lekht and R. L. Sorochenko, Astron. Zh. **78**, 137 (2001) [Astron. Rep. **45**, 113 (2001)].
12. H. W. Yorke and E. Krügel, Astron. Astrophys. **54**, 183 (1977).
13. A. V. Tutukov and B. M. Shustov, Nauchn. Inf. Astron. Soveta Akad. Nauk SSSR **41**, 125 (1978).
14. E. E. Lekht, Astron. Zh. **72**, 31 (1995) [Astron. Rep. **39**, 27 (1995)].

Translated by G. Rudnitskiĭ

Astronomy Reports, Vol. 47, No. 4, 2003, pp. 333–342. Translated from Astronomicheskiĭ Zhurnal, Vol. 80, No. 4, 2003, pp. 364–373.

Meridional Drift of Large-Scale Solar Magnetic Fields

V. N. Obridko and B. D. Shelting

Institute of Terrestrial Magnetism, Ionosphere and Radio Wave Propagation, Troitsk, 142190 Russia

Received August 5, 2002; in final form, October 10, 2002

Abstract—It is shown that the meridional drift of large-scale fields starts in the equatorial zone and continues over 15–16 yrs (16–17 according to another estimate), i.e., during three fourths of the 22-year cycle. There is an abrupt retardation of the drift at latitudes of 30°–50°, and a stagnation region where the drift rate does not exceed several meters per second arises. The drift becomes rapid again at higher latitudes. The stagnation region coincides with the area in which the radial gradient of the rotational velocity is close to zero in the convective zone. This drift is compared with helio-seismological data on the rotation in the convective zone. A model taking into account some elements of dynamo theory is proposed.

1. INTRODUCTION

The phenomenon of meridional drift, or more precisely the displacement of zones of solar activity in latitude, was revealed virtually simultaneously with the discovery of solar cyclicity. While we recognize Schwabe's report of 1843 as the first indication of a possible 10-year periodicity, we can find the first statement about the drift of a zone of spots in Carrington's classical treatise of 1863. For a long time, it was considered to be obvious that both phenomena exhibit a single periodicity. We now know that, though the spots indeed appear at a fixed latitude with a period of 11 yrs (or closer to 10 yrs in the twentieth century), the lifetime for the spots of each cycle is significantly longer. The first spots of a new cycle appear at latitudes of 40° and higher several years before the solar minimum, while the last spots are sometimes observed after the solar minimum at latitudes of about 5°–10°. Thus, the idea of an extended solar cycle was introduced [1].

The next step, namely, the analysis of cyclic variations of the large-scale and background fields, was started only in the 1960s. There is no doubt that the periodicity of the large-scale fields at each latitude is close to the periodicity of local fields and sunspots. However, the latitude dependence is less clear. Some papers [2–18] indicate that the meridional drift is directed from the equator toward the poles; the series of papers by Makarov *et al.* [6–11] should be particularly emphasized. These authors studied many of the peculiar properties of the polar drift, including the dependence of the drift on cycle power, the displacement of the neutral line that separates the mid-latitude and high-latitude parts, and the variation of the polar cap area; however, other papers [19–21] contest this. Some papers of the former group admit a possible additional drift from middle latitudes toward the equator, along with the meridional drift from the middle latitudes toward the poles. The inconsistency of these findings is first and foremost connected with the difficulties of eliminating the effects of stronger local fields in the total signal. In addition, the solar rotation, whose velocity exceeds that of the meridional drift of the large-scale fields by two orders of magnitude, contributes greatly to Doppler measurements.

The comparatively short interval for which data on the magnetic fields of the entire solar disk are available represents another difficulty. Therefore, the very thorough works [22–24] analyze data for only 10 yrs, while [13, 25] consider data for 22 yrs.

Here, we study the meridional drift of the large-scale fields over a long time interval, paying particular attention to the identification of the large-scale fields. For our analysis, we use both magnetic-field data detected using various magnetographs over 40 yrs and unified into a single data set and magnetic-field data recovered from Hα filament observations obtained over 85 yrs.

Since we are analyzing cyclic properties of the large-scale magnetic field, lower limits on the spatial size of the field are imposed by the observational technique used. In our analysis, the magnetograph data limit the spatial size of the field in three ways.

(1) The spatial resolution of the Stanford magnetograph is $3'$ ($\approx 0.2R_0$). Though other magnetographs provide higher resolution, the data were later averaged.

(2) The observations of magnetic fields at various latitudes were averaged over an entire Carrington revolution before the construction of the latitude–time diagrams.

1063-7729/03/4704-0333$24.00

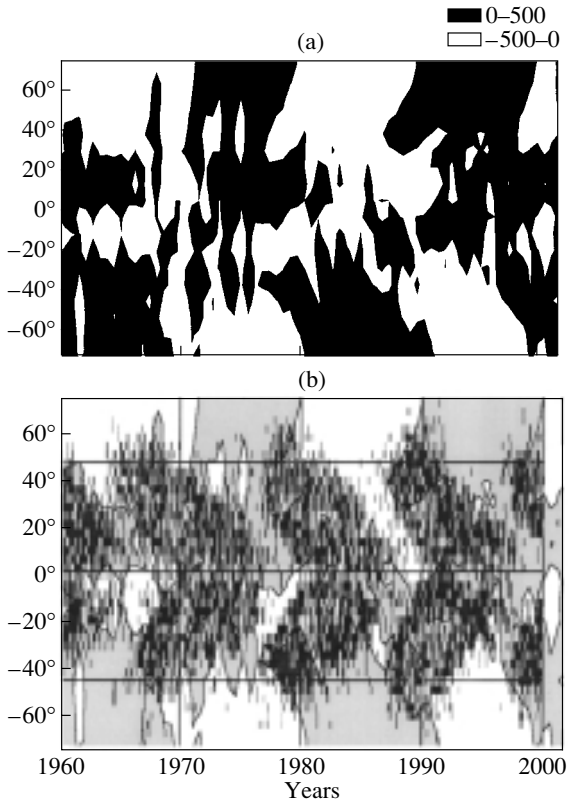

Fig. 1. (a) Latitude–time diagram for the radial magnetic field directly detected by magnetographs. (b) The same diagram combined with the Maunder butterflies.

(3) The number of harmonic coefficients used when calculating the magnetic-field components from the longitudinal field using Legendre polynomials was limited. We took into account only the first ten harmonics, which corresponds to sizes no smaller than $0.2R_0$. This provides an additional limitation on the spatial size of the field.

For the Hα data, the second and third constraints apply in the same way. In addition, the technique used to recover the field from spectral heliograms reconstructs large-scale fields far from active regions. Since the field strengths are not used in the analysis, the contribution of strong local fields to the reconstructed fields is considerably diminished. Therefore, the reconstructed fields are the most convenient for studies of the meridional drift [26, 27].

In Section 2, we shall compare data on the localization of spots and on the drift of the large-scale magnetic field obtained from direct magnetograph measurements over 40 yrs, as well as with magnetic data reconstructed over 85 yrs. These data are subject to additional filtration in Section 3. A subsidiary analysis to ascertain the phase dependence and drift rate is presented in Section 4. Section 5 presents a discussion of the results.

2. COMPARING THE DRIFTS OF LOCAL AND LARGE-SCALE FIELDS

The first set of data obtained by magnetographs covers 40 yrs (1960–2002) and includes the Mount Wilson magnetic measurements over 1960–1978, Kitt Peak data over 1975–1984, and Stanford measurements from 1976 until the present time. All data were graciously made available by researchers of these observatories. We have unified these data into a single (WSO) system [28]. Using these data, we have constructed latitude–time diagrams for the *longitudinal* magnetic fields averaged over a Carrington revolution.

Guided by the widespread hypothesis that the large-scale field in the photosphere is radial, we can calculate the radial field and construct the corresponding diagram. The difference between the two diagrams is insignificant, except for a small strengthening of B_r in comparison with the longitudinal field in near-polar regions. Therefore, we present only the B_r diagram (Fig. 1a).

We can immediately see the fine structure of the field: a number of "tongues" and "bays," and, first and foremost, the seeming absence of a clear direction for the meridional drift, especially at low latitudes. The obvious reason is the absence of the third constraint above limiting the size of the fields from below. We observe the total field rather than the sum of its largest-scale components ($l \leq 9$). The contribution of intense, small-scale, local fields is strong. This is first manifest at low latitudes, where we find a superposition of two meridional drifts: from the equator toward the pole for the large-scale fields and from the middle latitudes toward the equator for the local fields.

Figure 1b combines in a single latitude–time diagram the magnetograph data on the large-scale magnetic fields and the Maunder butterflies for sunspots. We can see that the local fields visibly *disrupt* the continuous drift of the large-scale fields from the equator toward the pole.

The Hα data on the large-scale fields covers 85 yrs (1915–2000). These data are partially taken from the atlas of P. McIntosh (1964–1974) and publications in Solar Geophysical Data (1975–1985), while the remaining are published or presented to us directly by Makarov (1915–1964 and 2000). As is discussed above, when working with the Hα data, we used an original technique to derive the magnetic-field strength from the synoptic maps, which specify only the sign of the magnetic field. To ensure the values were reasonable, we compared directly measured magnetic-field strengths with those calculated from the Hα observations for overlapping time intervals [28].

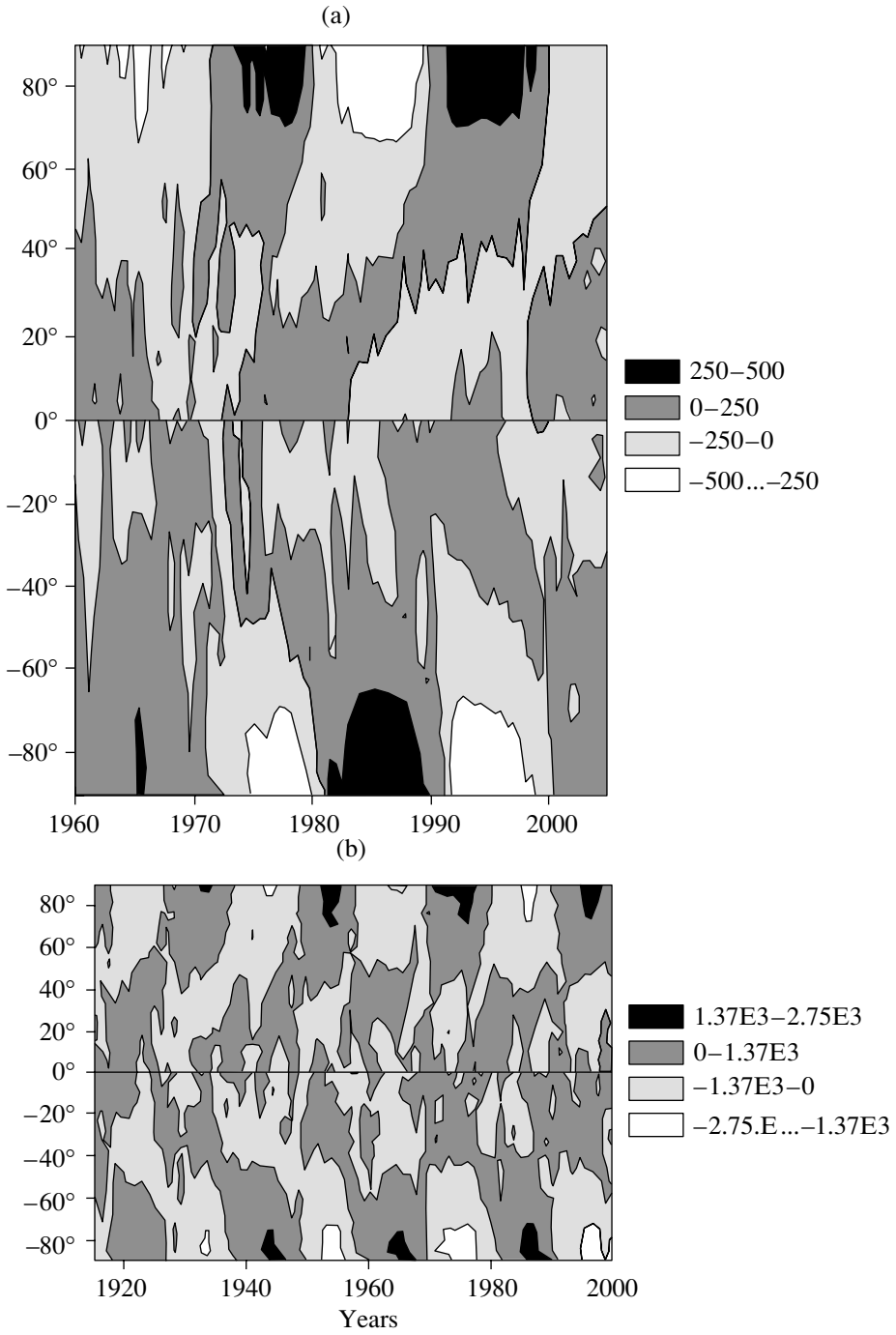

Fig. 2. Latitude–time diagram for the radial magnetic field calculated in the potential approximation from the (a) magnetograph and (b) Hα data.

A *direct* study of the polarity of the large-scale fields recovered from Hα data (i.e., without computing the radial field via polynomials) was carried out in [16]. As expected, the meridional drift toward the pole became much clearer in comparison with the magnetograph data. The drift toward the equator became almost invisible, being manifest only in small "tongues" of the secondary polarity near the equator. Nevertheless, more careful filtering is obviously necessary.

3. CALCULATIONS OF CYCLIC VARIATIONS OF RADIAL FIELDS IN THE PHOTOSPHERE

The calculations of each component of the magnetic field in the photosphere from the detected longi-

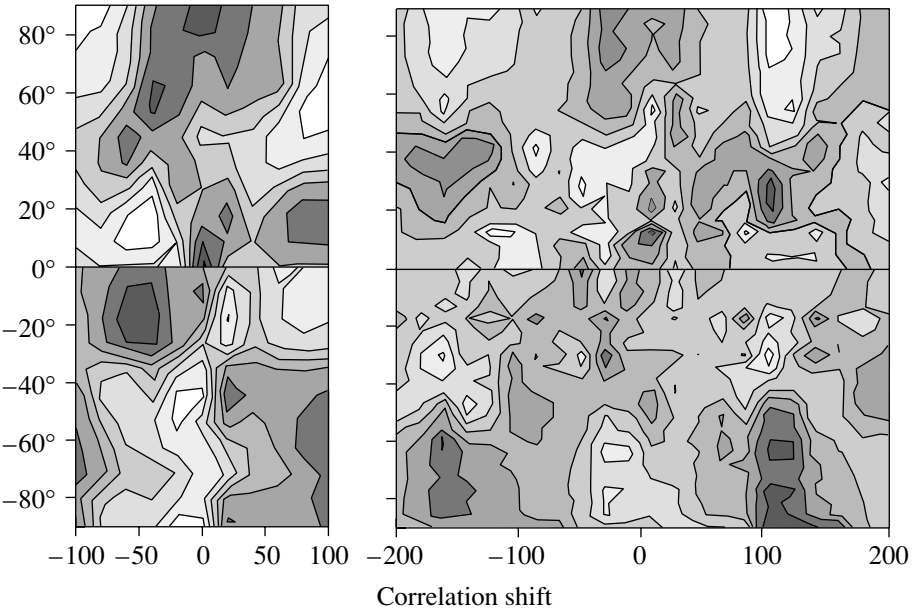

Fig. 3. Correlation between the large-scale magnetic fields obtained for various latitudes from the magnetograph (left) and Hα (right) data.

tudinal field are carried out in a potential approximation. The harmonic coefficients are obtained by two different techniques: the method of orthogonal Legendre polynomials [29] and the least squares method [26]. The radius of the source surface is assumed to be $2.5R_0$. A "classical" approximation was used; i.e., radial structure for the field was not assumed *a priori*. Since we were mainly interested in the behavior of the radial component B_r of the magnetic field, we first calculated the daily radial field values for latitudes from 0° to ±90° in steps of 1/15 in the sine of the latitude for the whole time interval. The results were then averaged over a Carrington revolution. We subsequently combined all data into a single file and constructed the latitude–time diagrams. Let us examine these in detail (Figs. 2a, 2b).

Figure 2a presents the latitude–time diagram for the radial magnetic field B_r calculated from the direct measurements of the large-scale longitudinal magnetic field. Figure 2b shows the latitude–time diagram for the B_r calculated from the Hα measurements of the large-scale longitudinal magnetic field. Let us analyze these two plots jointly. The dark gray regions that shade into black near the poles correspond to N polarity of the magnetic field (>0), while the light gray regions that shade into white near the poles correspond to S polarity (<0).

The motion of regions of large-scale magnetic field of each polarity from the equator toward the poles is clearly visible (compare with Fig. 1a). This drift of the large-scale fields differs fundamentally from the drift of the local fields, in particular from the motion of the Maunder butterflies from middle latitudes toward the equator. The drift rate of the large-scale fields depends on the latitude. From the equator to latitudes of 20°–25°, the drift is fairly rapid, and the magnetic field passes through this interval in two to three years. At latitudes of 25°–50°, the drift rate sharply decreases (it does not exceed 1 m/s), and the magnetic field passes through this 25° interval in 15 yrs. Further, the drift rate rapidly increases near the pole, and the magnetic field passes through the remaining 40°–50° in about one year. Thus, the total time for the transport of the large-scale fields is approximately 17–18 yrs; i.e., there is an extended cycle. It is interesting that the centers of the regions of the large-scale fields of each polarity are always situated near maxima of the local field at the equator and minima of the local field at the poles. Each regular region of large-scale field of a certain polarity arises at the equator when there is a reversal of the polarity of the two preceding fields at the poles (the last field, with the same polarity as the current equatorial field, and the next field, with the opposite polarity). The width of the region of each polarity in time is 11 yrs. During this time interval, three regions of large-scale field of alternating polarity corresponding to three different cycles lie one above the other at latitudes from the equator to the poles. Recall that the extended cycle of the local fields lasts 12–13 yrs, and there is a partial overlapping of two neighboring cycles at the latitudes of the wings of the Maunder butterflies. Note also that the maximum strength of the local fields is observed in a narrow latitude interval near 20°, whereas the

maximum strength for large-scale fields is observed near the poles.

Comparing these large-scale field diagrams with the Maunder butterflies, we arrive at the following conclusions.

(1) There is a clear, mutually opposite motion of the large-scale and local fields: the large-scale fields move from the equator toward high latitudes, while the local fields move from the high latitudes toward the equator. In each activity cycle, the local fields arise before the polarity reversal of the large-scale fields (by two to three years) and disappear near the equator simultaneously with the next polarity reversal of the large-scale fields, covering a time interval of 12–13 yrs. The narrow intersection of these two regions occurs at latitude 20°.

(2) The inclination of the butterflies to the time axis is virtually constant (a linear approximation is good) during their entire motion from the middle latitudes toward the equator. This inclination is about 5° per year. A butterfly moves through its whole path over 10–11 yrs, from the minimum of each cycle to the minimum of the following cycle. The central area of the butterfly (where there is the greatest number of spots) corresponds to the maximum of the local cycle and coincides in latitude (20°) with the intersection of the diagrams of the local and large-scale fields. The behavior of the large-scale fields differs from that of the local fields. First, the drift rate is not constant during the whole time interval, as was indicated above. Second, the large-scale fields move through their path from the equator to the middle latitudes, on average, over a longer time of about 17 yrs, i.e., from the maximum of the local cycle nearly to the minimum of the cycle following the next (the time is short by only one to two years).

These conclusions agree with the results presented in Fig. 3, which shows the correlations between the large-scale magnetic fields at various latitudes. The cross-correlation of the equatorial radial field with the radial field at other latitudes is calculated. We can see that the correlation region extends from the equator to the poles, and its total length exceeds 200 Carrington revolutions, or 15 yrs. Similar findings are presented in [18].

4. GENERAL SCHEME FOR THE MERIDIONAL CIRCULATION OF THE LARGE-SCALE MAGNETIC FIELDS

To ascertain the drift characteristics obtained from the magnetograph data, we approximate the field distribution in the latitude–time diagram (see the northern hemisphere in Fig. 2a) using the function

$$B_r/\sigma(\vartheta) = \sum_{\omega} A_\omega(\vartheta)\exp(i\omega(t+\varphi(\vartheta))), \qquad (1)$$

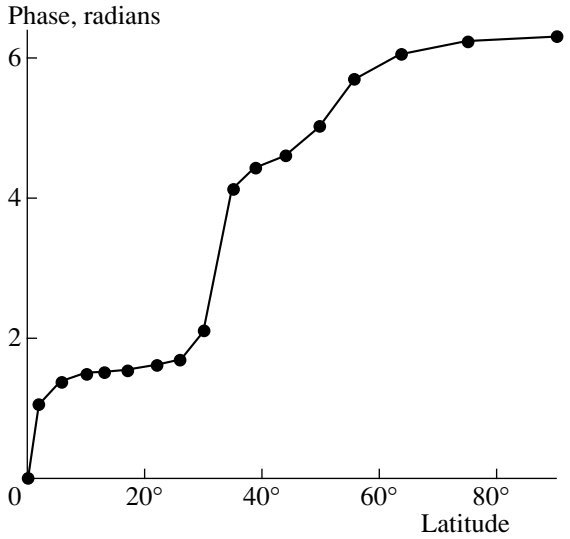

Fig. 4. Phase of the meridional drift model as a function of latitude.

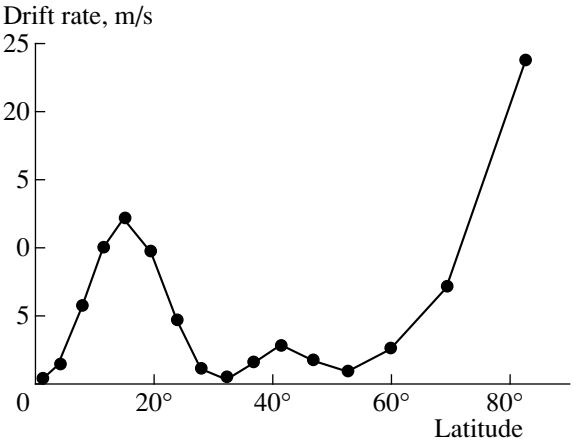

Fig. 5. The model rate for the meridional drift of the large-scale magnetic fields.

$$\sum_{\omega} A_\omega^2 = 1. \qquad (2)$$

We use this form of the Fourier transformation in order to analyze specifically the meridional drift and to separate it from the latitudinal variations of the strength of large-scale fields. Therefore, we first calculate the average $\langle B_r\rangle$ and variance $\sigma(\theta)$ over the entire time interval (1960–2002) for the each latitude. The average $\langle B_r\rangle$ turns out to be close to zero (as was expected), and all the $B_r(\theta,t)$ are then normalized to the corresponding $\sigma(\theta)$. Further, the amplitude $A_\omega(\theta)$, frequency ω, and phase $\varphi(\theta)$ are found for each latitude via a Fourier series expansion with fractional harmonics. As was mentioned above, the frequency ω corresponding to the maximum (about 20 yrs) is vir-

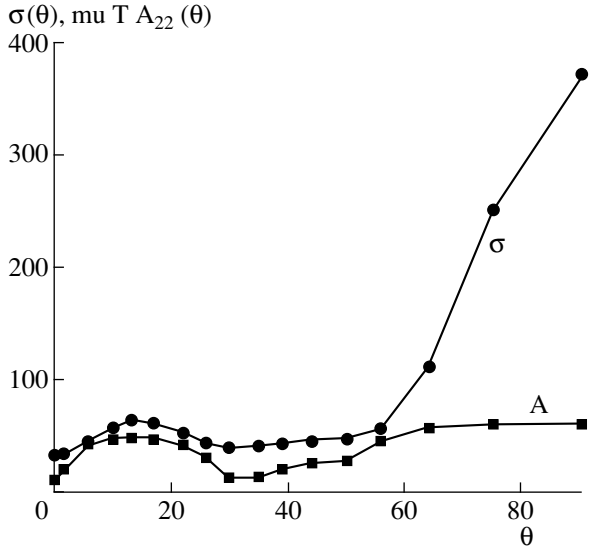

Fig. 6. The variance and amplitude of the 22-year cycle as functions of latitude in the model for the meridional drift.

tually independent of latitude and equal to 8.706 rad/s (i.e., the period is 20.87 yrs). We shall call this the "22-year cycle" and denote the related parameters by the subscript 22. The phase corresponding to this period is a rather complicated function of θ, accurate to within an arbitrary initial value.

Figure 4 presents the function $\varphi(\theta)$, which can be easily recalculated to give the rate of the meridional drift, shown in Fig. 5. Figure 5 indicates that there are two regions of rapid drift. The drift rate grows from almost zero near the equator and reaches its maximum of 13 m/s at a latitude of 20°. Approximately the same rate was obtained in [17, 31, 32]. At higher latitudes from 33° to 53°, the rate is extremely small, 1–3 m/s. Further, the rate rapidly increases to 25 m/s near the pole.

The functions $\sigma(\theta)$ and $A_{22}(\theta)$ (Fig. 6) also indicate these two zones. The function $\sigma(\theta)$ is the r.m.s magnetic field calculated for a given latitude over the long time interval of two magnetic cycles. We can see that the r.m.s. strength of the large-scale field in the polar zone exceeds that of the equatorial maximum at latitudes 16°–18° by a factor of five or more. The function $A_{22}(\theta)$ describes the contribution of the 22-year cycle at each latitude. Here, these two maxima are also seen, but the difference between them is much smaller. The value of $A_{22}(\theta)$ at high latitudes exceeds that at latitude 20° by only 25%.

The quantitative results of the foregoing analysis are presented in the Table.

Figure 7 shows a scheme for the cyclic variation of the meridional drift obtained by the formula

$$B_r = A_{22}(\vartheta)\exp(i\omega_{22}(t+\varphi_{22}(\vartheta))).$$

This means that we use here two additional types of filtering besides the three previous types presented in the Introduction. First, we add frequency filtering to eliminate every cycle except the 22-year cycle. Second, we remove the strong dependence of the large-scale fields on latitude, expressed in Eq. (1) by the denominator $\sigma(\theta)$.

Quantitative characteristics of the drift of the large-scale magnetic fields

Latitude	$A(\theta)$	$A^2(\theta)$	$\sigma(\theta)$	Phase
90°	0.6226	0.3877	374.8899	6.31828
75°	0.6227	0.3878	251.5153	6.2448
64°	0.5932	0.3518	113.0285	6.06852
56°	0.4574	0.2092	57.6674	5.71597
50°	0.2950	0.0871	47.2941	5.01434
44°	0.2659	0.0707	46.7928	4.62862
39°	0.2240	0.0502	44.6023	4.42442
35°	0.1384	0.0191	41.5526	4.14342
30°	0.1331	0.0177	40.0913	2.11691
26°	0.3148	0.0991	44.7899	1.72671
22°	0.4302	0.1851	53.7202	1.62887
17°	0.4881	0.2383	63.0929	1.56958
13°	0.4976	0.2476	63.6749	1.53136
10°	0.4865	0.2366	58.8488	1.49697
6°	0.4236	0.1795	47.0516	1.41616
2°	0.2190	0.0480	36.1304	0.02248
0°	0.1108	0.0123	34.9017	0.000

5. DISCUSSION

The drift of the large-scale fields from the equatorial zone toward the pole takes 15–16 yrs (or 16–17 yrs according to another estimate), i.e., three fourths of the 22-year cycle. The reverse motion, which is not directly observed, takes 5–6 yrs. The drift on the surface during these 5–6 yrs is virtually equal to zero. It then abruptly grows, and its rate exceeds 10 m/s. There is an abrupt retardation of the drift at latitudes 30°–50°, and a stagnation region where the rate does not exceed several meters per second arises. The drift again becomes rapid at higher latitudes. The stagnation region coincides with the region where the radial gradient of the rotational velocity in the convective zone is close to zero (there is a change of sign in $\partial\omega/\partial r$). At the same time, the stagnation

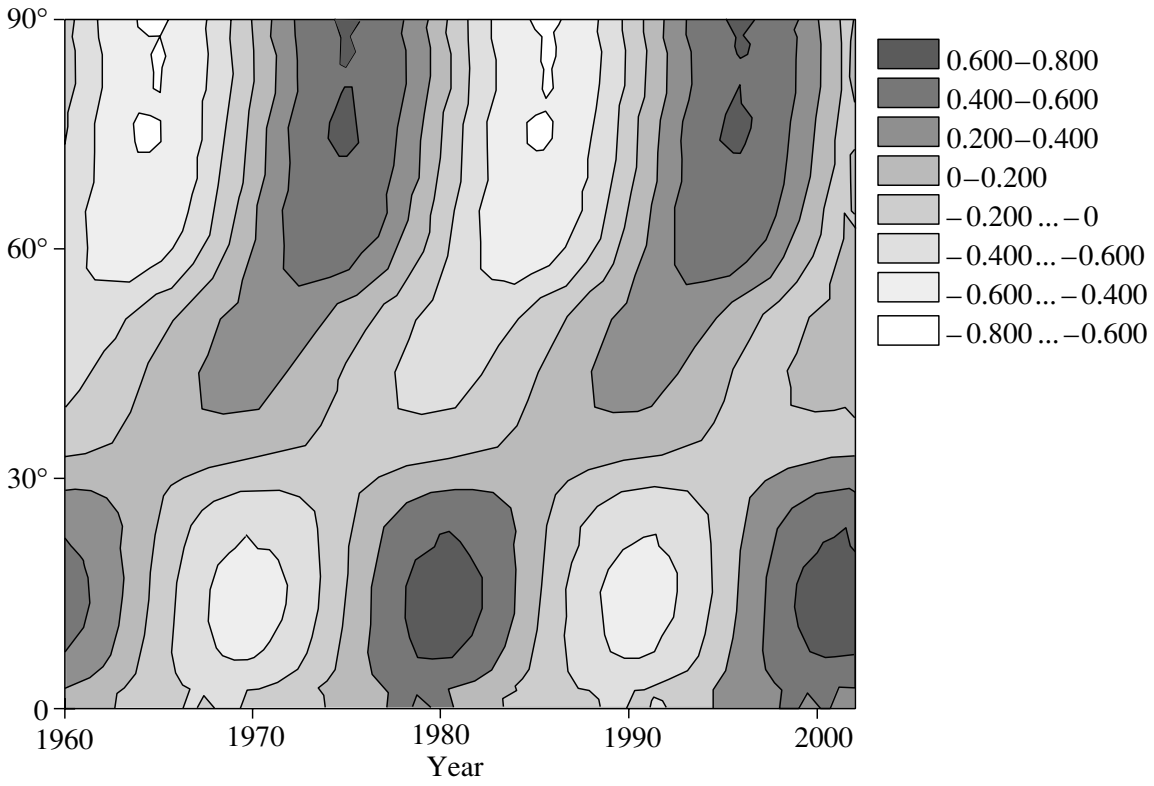

Fig. 7. Scheme for the cyclic variation of the meridional drift.

region is extended in latitude, and its high-latitude and low-latitude boundaries appear as neutral curves in the latitude–time diagrams. The variation of these boundaries and its secular cycle were studied in [11, 33].

The average rate of the polar drift is ~ 2 m/s.

Let us consider the agreement between these findings and classical dynamo models. In most models (see, for example, [34] using the model of the convective zone [35]), the meridional drift naturally arises in the generation process due to the negative dynamo number at the base of the convective zone. This drift is directed toward the equator and explains the Maunder butterflies for the local fields. These models neglect drift motions in higher layers of the convective zone [36]. The meridional drift of the large-scale fields toward the pole is frequently explained as a consequence of the diffusion of tail polarities of the local fields due to differential rotation (see [14, 15] and references therein). However, in this case, it is difficult to understand why the equatorial fields follow the evolution of the polar fields with a time lag of 5–6 yrs (see [33] and references therein). There are also other direct objections to this scheme with the diffusion transport of some portion of the local fields toward the pole. It is unclear how the large-scale, deep, poloidal magnetic field can originate from surface elements in the form of sunspots [37, 38]. Finally, it remains unclear why the large-scale fields in the polar zone significantly (by a factor of five or more) exceed the equatorial large-scale fields in the case of simple transport of the tails of active regions toward the pole. A flux of material directed toward the pole is postulated in [22, 23], where it is shown that the calculated drift can agree with observations for appropriately chosen parameters. However, the time interval used for the comparison with observations is short, and the polar drift covers only 10 yrs.

One qualitative scheme for the generation of large-scale fields in the solar cycle is the following. We will describe it in terms of the concentrated fields (CF) and diffusive fields (DF) introduced in [22], which we consider to be more convenient from the physical point of view than the terms toroidal and poloidal fields that are usually used in dynamo theory.

We shall use the structure of motions in the convective zone described in [35]. Figures 8a and 8b show the important $d\Omega/dr$ and $d\Omega/d\theta$ diagrams. The strongest radial gradient takes place within a narrow layer of thickness $0.05R_0$ [39] situated directly beneath the base of the convective zone at latitudes lower than 36° ($\sin\theta < 0.6$). This is the tachoclinic region where the $\alpha - \omega$ dynamo operates [40]. Here, the ω dynamo creates strong concentrated fields. Since $\alpha < 0$ in this region [34], this region of CF

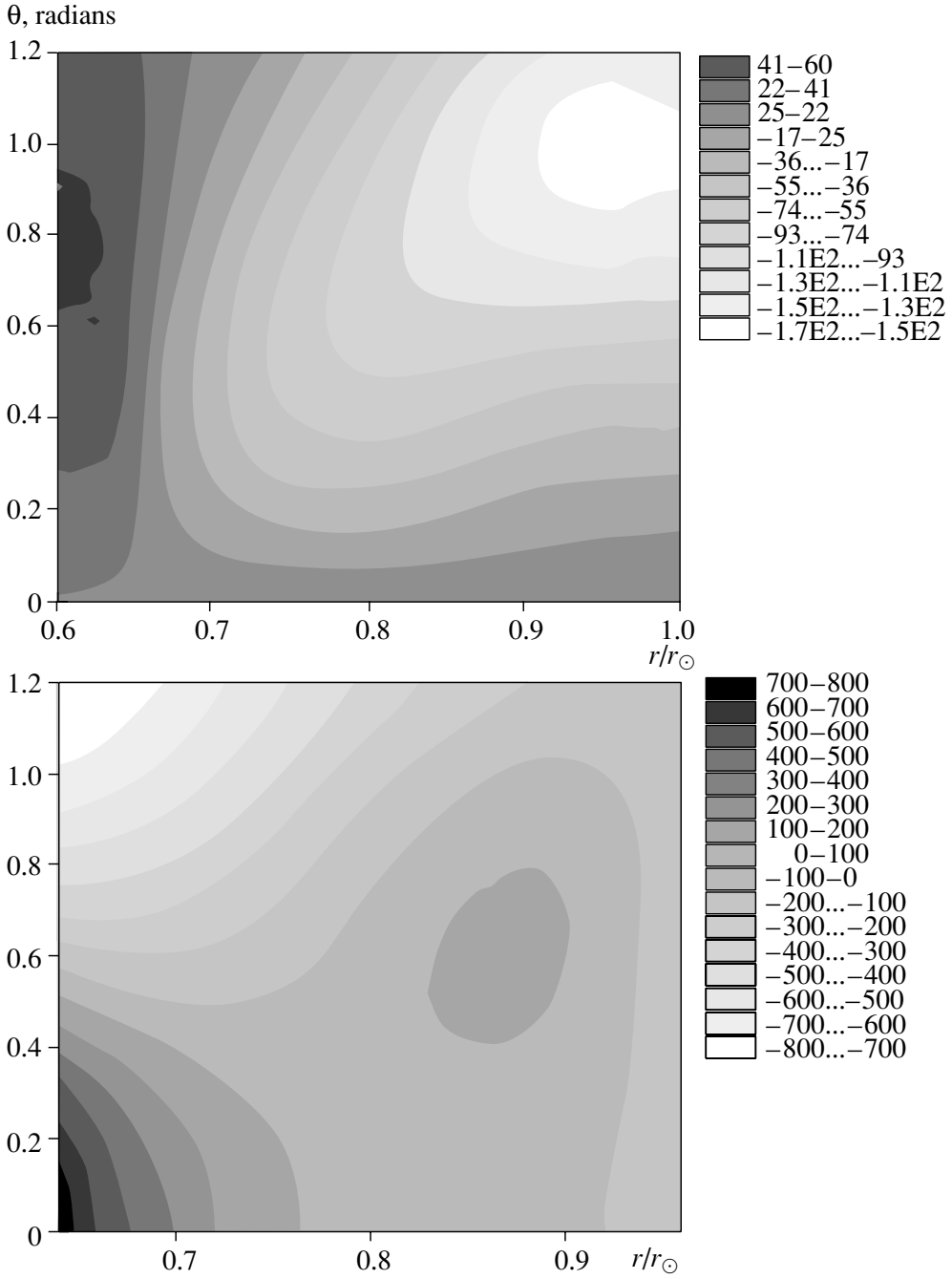

Fig. 8. $d\Omega/dr$ (top) and $d\Omega/d\theta$ (bottom) diagrams.

drifts from the middle latitudes toward the equator, while the fields rapidly (over several days) rise to the surface radially due to the buoyancy force. These fields are tubes of CF, with their meridional drift during their ascent being insignificant. For a meridional drift rate of 10 m/s, the tube drift toward the pole over 15 days does not exceed 10^4 km, remaining less than the size of the tube itself. As a result, we observe on the surface Maunder butterflies directed toward the equator, reflecting the drift of the "spot creating" zone in the tachoclinic region. However, the spot tubes are not directly connected to the tachoclinic region and are immersed below the solar surface no deeper than 6 000–12 000 km [37, 38]. The sunspots thus remain surface phenomena.

The α (or α^2) dynamo operates simultaneously [41, 42]. It is more efficient in higher layers, where the parameter α changes sign for $R \geq 0.72R_0$ [34]. The evolution of diffuse fields is independent of the CFs [22], since the equation for weak, large-scale DFs

branches off. The ω dynamo wave becomes the lower boundary condition for the α dynamo. Thus, the DFs arise in a wider region of the convective zone, rather than in the narrow tachoclinic region. There are no sharp boundaries for these fields, and the magnetic-pressure gradients are weak. Therefore, these fields move along with the medium. They rise slowly (they have low buoyancy) and are strongly dragged by the meridional drift in the convective zone. These fields can be additionally strengthened in the polar region due to the strong negative gradient $d\Omega/d\theta$ (Fig. 8b). The rates of the meridional drift obtained in [36] from helio-seismological data agree well with our results. Though the DFs arise above the CFs, they must be considered as being deeper when interpreting the observations. Therefore, we usually treat the large-scale and global magnetic fields as deep phenomena (see the discussion in [18]).

Stix [43] has calculated a similar pattern for the drift of the large-scale fields toward the pole using an $\alpha\Omega$ dynamo model.

The nature of the stagnation region in the latitude-time diagram is unclear. In [10], it was interpreted as resulting from the complex interaction of two magnetic-field source with different signs (polar and sunspot ones). It turned out that the balance between these fields can provide the absence of a polar drift during a long period.

It is extremely difficult to reveal the reverse drift in both our data and the helio-seismological data. The analysis of the cross-correlation of the large-scale field strengths in [18] does not indicate any direct drift but shows that the equatorial structure is similar to the polar structure with a time lag of 5–6 yrs. This implies a rate for the reverse drift of $\sim$5–6 m/s. On the other hand, this correlation is also consistent with the suggestion that the inverse branch also spans 15–16 years. Arguments for this suggestion were advanced in [44], where Tlatov proposed a model that is generally similar to our model but has an inverse branch longer than 11 years. The inverse drift velocity must then be 2 m/s. The author of [36] also failed to demonstrate the presence of a reverse drift directly using helio-seismological data but, from the continuity equation, estimated the reverse rate to be $\sim$3 m/s and the level in the convective zone where the meridional flow toward the pole is changed to the reverse flow to be $\sim 0.80R_0$.

In our discussion, we have used a model for the convective zone constructed especially for the rising branch of the 23rd cycle. If this model is changed, some of our results will require refinement.

Note that since both the large-scale diffuse field and the local concentrated fields are produced by a single generation process, one might expect the meridional field drift velocity to depend on the power of the 11-year cycle. This result was previously obtained in [11].

All our calculations have used a "classical" model in which the source surface is $2.5R_0$ from the Sun's center, and the field at the surface of the photosphere is potential. The calculations in an alternative model in which the photospheric field is taken to be radial and the source surface is at $3.25R_0$ give no significantly new results. The diagram obtained is virtually the same as that in Fig. 2a.

6. ACKNOWLEDGMENTS

The authors are grateful to E. V. Ivanov, K. M. Kuzanyan, and D. D. Sokolov for helpful discussions, to V. I. Makarov and A. G. Tlatov for providing us with unpublished data, and to the Wilcox Solar Observatory staff for the data received via INTERNET. This work was supported by the Russian Foundation for Basic Research (project nos. 00-15-96661 and 02-02-16199) and by INTAS (project 2000-840).

REFERENCES

1. K. Harvey, in *The Solar Cycle*, Ed. by K. L. Harvey, Astron. Soc. Pac. Conf. Ser. **27**, 335 (1992).
2. V. Bumba and R. Howard, Astrophys. J. **141**, 1502 (1965).
3. T. L. Duvall, Jr., Sol. Phys. **63**, 3 (1979).
4. R. Howard and B. J. LaBonte, Sol. Phys. **74**, 131 (1981).
5. B. J. LaBonte and R. F. Howard, Sol. Phys. **80**, 361 (1982).
6. V. I. Makarov and K. R. Sivaraman, in *Solar Photosphere: Structure, Convection, and Magnetic Fields*, Ed. by J. O. Stenflo (IAU, 1990), p. 281.
7. V. I. Makarov, Sol. Phys. **93**, 393 (1984).
8. V. I. Makarov and K. R. Sivaraman, Sol. Phys. **119**, 35 (1989).
9. V. I. Makarov and K. P. Sivaraman, Sol. Phys. **123**, 367 (1989).
10. V. I. Makarov and A. G. Tlatov, Izv. Ross. Akad. Nauk, Ser. Fiz. **62**, 1853 (1998).
11. R. K. Ulrich, J. E. Boyden, L. Webster, *et al.*, Sol. Phys. **117**, 291 (1988).
12. Y.-M. Wang, J. Lean, and N. R. Sheeley, Geophys. Res. Lett. **27**, 505 (2000).
13. Y.-M. Wang, A. G. Nash, and N. R. Sheeley, Astrophys. J. **347**, 529 (1989).
14. Y.-M. Wang, A. G. Nash, and N. R. Sheeley, Science **245**, 712 (1989).
15. V. N. Obridko and G. Gaziev, in *The Solar Cycle*, Ed. by K. L. Harvey, Astron. Soc. Pac. Conf. Ser. **27**, 410 (1992).
16. R. W. Komm, R. F. Howard, and J. W. Harvey, Sol. Phys. **147**, 207 (1993).
17. E. V. Ivanov and V. N. Obridko, Sol. Phys. **206**, 1 (2002).

18. M. Perez Garde, M. Vazquez, H. Schwan, and H. Wohl, Astron. Astrophys. **93**, 67 (1981).
19. B. N. Anderson, Sol. Phys. **94**, 49 (1984).
20. G. Lustig and H. Wohl, Astron. Astrophys. **229**, 224 (1990).
21. M. Dikpati and A. R. Choudhuri, Astron. Astrophys. **291**, 975 (1994).
22. M. Dikpati and A. R. Choudhuri, Sol. Phys. **161**, 9 (1995).
23. A. R. Choudhuri and M. Dikpati, Sol. Phys. **184**, 61 (1999).
24. Y.-M. Wang, N. R. Sheeley, Jr., and J. Lean, Geophys. Res. Lett. **27**, 621 (2000).
25. V. N. Obridko and B. D. Shelting, Sol. Phys. **201**, 1 (2001).
26. B. D. Shelting and V. N. Obridko, Astron. Astrophys. Trans. **20** (3), 491 (2001).
27. V. N. Obridko and B. D. Shelting, Sol. Phys. **184**, 187 (1999).
28. J. T. Hoeksema and P. H. Sherrer, *Solar Magnetic Field—1976 through 1985* (WCDA, Boulder, 1996).
29. K. G. Ivanov and A. P. Kharshiladze, Geomagn. Aeron. **34**, 22 (1994).
30. R. K. Ulrich, in *IAU Colloq. 137: Inside the Stars* (1993), A93-53126 23-90, p. 25.
31. H. B. Snodgrass, Sol. Phys. **94,** 13 (1984).
32. V. I. Makarov, A. G. Tlatov, D. K. Callebaut, *et al.*, Sol. Phys. **198,** 409 (2001).
33. V. I. Makarov, A. G. Tlatov, and K. R. Sivaraman, Sol. Phys. **202**, 11 (2001).
34. G. Belvedere, K. M. Kuzanyan, and D. D. Sokoloff, Mon. Not. R. Astron. Soc. **315**, 778 (2000).
35. J. Shou *et al.*, Astrophys. J. **505**, 390 (1998) .
36. P. M. Giles, Dissertation (Stanford University, 1999).
37. V. N. Obridko, *Sun Spots and Activity Complexes* [in Russian] (Nauka, Moscow, 1985).
38. J. Zhao, A. G. Kosovichev, and T. L. Duvall, Jr., Astrophys. J. **557**, 384 (2001).
39. A. G. Kosovichev, Astrophys. J. **469**, L61 (1996).
40. E. A. Spiegel and J. P. Zahn, Astron. Astrophys. **265**, 106 (1992).
41. H. K. Moffat, in *Magnetic Field Generation in Electrically Conducting Fluids* (Cambridge Univ., Cambridge, 1978).
42. F. Krause and K.-H. Radler, in *Mean Field Magnetogydrodynamics and Dynamo Theory* (Pergamon, Oxford, 1980).
43. M. Stix, Astron. Astrophys. Trans. **20** (3), 417 (2001).
44. A. G. Tlatov, Astron. Zh. **74**, 448 (1997) [Astron. Rep. **41**, 394 (1997)].

Translated by V. Badin

Astronomy Reports, Vol. 47, No. 4, 2003, pp. 343–353. Translated from Astronomicheskiĭ Zhurnal, Vol. 80, No. 4, 2003, pp. 374–384.

A Charge-consistent Model for the Acceleration of Iron in the Solar Corona: Nonisothermal Injection

M. F. Stovpyuk and V. M. Ostryakov

St. Petersburg State Polytechnical University, St. Petersburg, Russia

Received June 15, 2002; in final form, October 10, 2002

Abstract—A charge-consistent numerical model for the joint (regular and stochastic) acceleration of iron by a spherical shock wave propagating in the solar corona is proposed. Large-scale irregularities of the plasma density and the nonisothermal injection of ions are taken into account. For the case of iron, the energy dependence of the mean charge $\bar{q}_{\mathrm{Fe}}(E)$ is determined by the relationships between the characteristic acceleration time, the charge-variation time for the accelerated ions, and the time for their trapping in regions of high plasma density. Due to the global inhomogeneity of the medium, these relationships depend on the shock speed. Our calculations indicate that photoionization by soft X-rays from flare regions can substantially change the charge states of heavy ions only in the most powerful solar events (both impulsive and gradual). © *2003 MAIK "Nauka/Interperiodica"*.

1. INTRODUCTION

Considerable experimental data on the charge states of solar cosmic rays have been accumulated in the last two decades. A number of studies have found that the mean charge of heavy elements accelerated by the Sun increases with increasing energy [1–7]. This effect can be explained only by charge-consistent acceleration models, which were first introduced in [8]. Their most important feature is that they take into account the mutual influence of the acceleration of a multiply charged ion and changes in its charge state [9–12]. The efficiency with which an ion is accelerated depends on its charge (due to the diffusion coefficients in the coordinate and momentum spaces). At the same time, the charge itself can change in the acceleration process, due to inelastic collisions with electrons and protons of the background plasma, as well as radiation from the plasma in the active region. Therefore, the observed increase in the mean charge can be interpreted as extra stripping of the ions during their acceleration, since the collisional ionization cross sections in the energy range under consideration ($\sim$1 MeV/nucleon) are rather large. Along with providing an interpretation for the observational data on the mean charges, charge-consistent models can serve as an indirect diagnostic tool for the plasma in the acceleration region. More precisely, they enable us to determine the plasma temperature T and number density N—the values providing agreement between the numerical computations and experimental data [9, 11, 13–15].

In our previous studies based on the charge-consistent approach, we considered (in a planar geometry) the regular acceleration of multielectron elements (C, O, Ne, Mg, Si, and Fe) by a parallel shock [14]. The background plasma was assumed to be uniform and to have constant density and temperature during the entire acceleration process. In addition, the spatial (and, consequently, energy) diffusion coefficients were assumed to be coordinate-independent. The present work is free of these simplifications, and we take into account both the spherical geometry of the shock front and variations in the parameters of the background plasma and accelerating turbulence during its propagation. Moreover, along with the regular gain in energy (first-order Fermi acceleration), we have included in the model stochastic acceleration (second-order Fermi acceleration), adiabatic energy losses, and the nonzero thickness of the shock front. As in our previous works [13, 14], the main processes responsible for variations in the ion charge are assumed to be collisional ionization by the background thermal protons and electrons (including subsequent autoionization) and radiative and dielectronic recombination. The corresponding cross sections were taken from various sources: [16] for collisional ionization by protons and [17, 18] for ionization by electrons, autoionization, and both types of recombination. Along with these processes, we also analyzed the contribution of photoionization to the formation of the mean iron charge. Thus, our aim is to study differences in the energy dependence $\bar{q}_{\mathrm{Fe}}(E)$ and charge distributions of Fe produced by

1063-7729/03/4704-0343$24.00

the above refinements of the model, compared to the results of simpler models.

2. ACCELERATION OF MULTIPLY-CHARGED IONS BY A MOVING SPHERICAL SHOCK FRONT

To demonstrate the main differences from the uniform case, we shall analyze Fe, since this element is quite abundant in solar cosmic rays and possesses a wide range of possible charge states of its ions. Consequently, Fe provides a convenient example to illustrate features in the energy and charge spectra specific to the approach used. An energetic ion moving through plasma can both gain and lose electrons, so that its charge q can either decrease ($q \to q-1$) or increase ($q \to q+1$). (We neglect here the loss or gain of several electrons during a single interaction, since this process is considerably less probable.) Then, the characteristic ionization and recombination rates can be written

$$S_q(V_{\rm ion}) = \sum N \int \sigma_{qq+1}(V) F(V, V_{\rm ion}) V\, dV, \quad (1)$$

$$\alpha_q(V_{\rm ion}) = \sum N \int \sigma_{qq-1}(V) F(V, V_{\rm ion}) V\, dV. \quad (2)$$

Here, V is the relative velocity of the interacting particles, $F(V, V_{\rm ion})$ is the distribution function of the electrons and protons of the ambient plasma in the rest frame of the ion moving with velocity $V_{\rm ion}$ [16, 17], $\sigma_{qq\pm1}(V)$ are the cross sections for the atomic reactions resulting in the transitions from the charge state q to $q \pm 1$, and N is the density of the background plasma, which possesses an equal number of protons and electrons, so that $N_e \approx N_p \equiv N$. The total ionization (1) or recombination (2) rates are summed over all the atomic processes listed in the Introduction.

It is known that an isotropic distribution of energetic particles forms much more rapidly than the spatial diffusion or acceleration of the particles (see, for example, [19, 20]). Accordingly, we shall neglect the anisotropic stage of the acceleration. Let f_{qi} be the isotropic distribution functions for the ions with charge q; the variables E (energy) and r (heliocentric distance) will be omitted later for the sake of conciseness. The interval of r must be separated into two parts: in front of the shock ($r > R(t)$) and behind it ($r < R(t)$), which will be denoted by the subscripts 1 and 2. The position of the shock front at each time is determined by the formula $R(t) \equiv R = R_0 + \int_0^t V_s(t')\, dt'$, where R_0 is the shock's initial position and $V_s(t) \equiv V_s(R)$ is its velocity in the corona. Replacing the function f_{qi} with f_{q+1i} and f_{q-1i} corresponds to the loss or gain of an electron due to some atomic process. Finally, we must solve a system of differential equations for the acceleration of ions with various charges, taking into consideration all substantial transitions between the neighboring charge states. In the spherically symmetric case, this system takes the form (see also [10, 11, 13])

$$\begin{aligned} &\frac{1}{r^2}\frac{\partial}{\partial r}\left(r^2 \chi_{qi} \frac{\partial f_{qi}}{\partial r}\right) - w_i(r)\frac{\partial f_{qi}}{\partial r} \\ &+ \frac{1}{r^2}\frac{\partial}{\partial r}(r^2 w_i(r))\left(\frac{2E}{3}\frac{\partial f_{qi}}{\partial E} - \frac{f_{qi}}{3}\right) \\ &+ \frac{\partial}{\partial E}\left(\frac{dE}{dt} f_{qi}\right) + \frac{\partial^2}{\partial E^2}(\varphi_i f_{qi}) - \frac{\partial}{\partial E}(\psi_i f_{qi}) \\ &+ (f_{q-1i} S_{q-1i} - f_{qi}(S_{qi} + \alpha_{qi}) \\ &+ f_{q+1i}\alpha_{q+1i}) = \frac{\partial f_{qi}}{\partial t}, \end{aligned} \quad (3)$$

where the charge subscript varies from $q_{\min} = +1$ to $q_{\max} = +Z$ and Z is the nuclear charge. We can see that this equation includes the stochastic acceleration of ions along with their regular acceleration at the shock front [21, 22], as well as the adiabatic energy losses of the particles in the expanding solar-wind flow when it is formed in the corona [23, 24].

We can write for the velocity of the plasma flow in the rest frame of the shock front

$$u(r) = -\frac{u_1 + u_2}{2} - \frac{u_1 - u_2}{2}\,\mathrm{th}\left(\frac{r - R}{\delta}\right), \quad (4)$$

where $u_1(r) = V_s(R) - w_1(r)$, $u_2 = u_1/\sigma$, σ is the compression factor, and δ is the thickness of the shock front. Formula (4) represents a simple description of the broadening of the shock front due to the influence of energetic protons (see, for example, [19, 20]). Since we consider the acceleration of iron, whose number density is small compared to the density of protons in the plasma, the front width δ can be taken to be an external parameter of the model. The minus sign in (4) shows that the plasma flows into the shock front in the direction of decreasing r. In the case of (3), which is written in heliocentric coordinates, the corresponding flow velocity is given by

$$w_i(r) = \begin{cases} W(r), & i = 1 \\ V_S(R)(\sigma - 1)/\sigma + W(r)/\sigma, & i = 2, \end{cases} \quad (5)$$

where $W(r)$ is the solar-wind velocity (see below).

Since the radius R of the shock increases with time, spatial irregularities of the ambient corona are equivalent to temporal irregularities of the inflowing plasma. The required dependence $V_s(t)$ (or $V_s(R)$) seems not to be a universal function, although dimensional arguments suggest it has the form $V_s(R) \sim$

$NR^2)^{1/4}$ [25]. On the other hand, the required relation can be extracted from the results of numerical modeling of the propagation of coronal shocks presented in [26, 27]. However, the analytic model formulas for $V_s(t)$ (see below) will be more convenient for our use. Further, we shall use the following dependence for the number density $N \equiv N(r)$ [28]:

$$\log(N(r)/1\ \mathrm{cm}^{-3}) = 9.6 - \exp(0.19(\log(r/R_\odot - 1) + 2.3)^2), \quad (6)$$

where $R_\odot = 6.96 \times 10^{10}$ cm is the solar radius. This formula was derived in [28] from *Skylab* measurements of the white-light luminosity of the solar corona. The solar-wind velocity $W(r)$ can be described by the expression [24]

$$W(r) = 1.836 \times 10^8/(N(r)(r/R_\odot)^2),\ \mathrm{km/s}, \quad (7)$$

where the number density $N(r)$ is measured in cm^{-3}.

The spatial diffusion coefficients along the magnetic field that appear in (3) were chosen so that their dependence on r is [19, 24]

$$\chi_q \equiv \chi_q(r, E) = \chi_{qi}(E)\frac{r}{R_0}, \quad (8)$$

where the factor

$$\chi_{qi}(E) = \chi_{0i}\left(\frac{q}{A}\right)^{S-2} E^{(3-S)/2} \quad (S < 2) \quad (9)$$

is a function of the energy, charge, and atomic weight A of the accelerated ion, as well as the spectral index S of the scattering (Alfven) turbulence [19, 29], and the χ_{0i} are constants that are different in regions 1 and 2. We assumed in our model that $\chi_{02} = 0.1\chi_{01}$, since the level of turbulence in region 2 is considerably higher than in region 1.

The functions φ_i and ψ_i in (3) can be expressed in terms of the diffusion coefficient in momentum space D_{qi}:

$$\varphi_i = D_{qi}\left(\frac{dE}{dp}\right)^2, \quad \psi_i = \frac{1}{p^2}\frac{dE}{dp}\frac{\partial}{\partial E}\left(p^2 D_{qi}\frac{dE}{dp}\right), \quad (10)$$

where we have for Alfven turbulence [19]

$$D_{qi} \approx \frac{V_a^2 p^2}{\chi_{qi}}, \quad (11)$$

and V_a is the Alfven velocity.

Finally, the term containing dE/dt in (3) describes the Coulomb losses due to collisions of the particles with electrons and protons of the background plasma [30].

Note that our considering only the radial coordinate r in Eqs. (3) implies that the center of our spherical coordinate system coincides with the center of the Sun, so that the shock front represents a concentric surface. This simplification is quite reasonable, at least for some shocks observed in the solar corona [27, 31]. In fact, the spherical shock front is simply a segment of a sphere. However, the corresponding boundary effects seem to be sufficiently small, since the number of particles accelerated at the boundaries of the segment is only a small fraction of the total number. This total number of accelerated particles was not determined by the Monte Carlo method used in our work (see below).

Before moving on to the next section, let us discuss the injected charge distributions. In [10], we adopted equilibrium or thermal charge distributions for the element under consideration corresponding to a fixed temperature in the acceleration region [10]. However, the acceleration of particles in the Sun is a process that is extended in time and covers a considerable spatial region, up to several $R_\odot$. Can we believe that this process is characterized by a single value of the plasma temperature T? The answer seems to be negative. For example, there are experimental data pointing toward evolution of the plasma temperatures in solar-flare regions over times of tens to hundreds of seconds [32]. If the acceleration of heavy particles occurs on these same time scales, then the injected charge distribution for even a single element should correspond to a range of temperatures (i.e., the injection is not isothermal). In addition, the analysis of the prolonged flare of August 25, 1998 [33], and observations of the mean charges of various elements from a set of impulsive events [34] also suggest nonisothermal injection during the acceleration. Of course, in principle, we have already included nonisothermal behavior in our consideration of the charge distributions of even a single element. Unfortunately, allowing temperature variations in the coefficients S_q and α_q at each temporal step (see below) would result in excessive computation times. Therefore, for the sake of simplicity, we have assumed in our model that some fraction of the particles are accelerated in plasma with temperature T_1, some other fraction is accelerated in plasma with temperature T_2, and so on. The resulting charge distribution for the accelerated element is derived by summing these charge distributions, assigning them appropriate weights. This procedure can easily explain the dispersions of the charge distributions of the particles (if they are not too far from Gaussian) in the case of constant mean charges, which was very difficult under the assumption of isothermal injection [11]. This temperature variability, in turn, is equivalent to a mixture of particles accelerated in various sources with various temperatures—in the solar wind, dense or rarefied plasmas, impulsive or prolonged solar events, and so on—since the irregularities of the corona itself are less

important at the heliocentric distances under consideration.

3. NUMERICAL MODEL

We found a numerical solution for the problem formulated in the preceding section using the Monte Carlo method [35–38], which is often applied when considering the acceleration of particles by shocks [21, 39–41]. Let a particle with initial energy E_{inj} and charge q_0 be injected into the shock front at time t_0. Equations (3) enable us to find the coordinate of the particle in each step k of its discrete motion, separated by an interval Δt from the preceding step $(k-1)$:

$$r_k = r_{k-1} + \left(w_i(r_{k-1}) \right. \tag{12}$$
$$\left. - \frac{2\chi_{qi}(r_{k-1})}{r_{k-1}} - \left(\frac{\partial \chi_{qi}(r)}{\partial r} \right)_{r=r_{k-1}} \right) \Delta t + \eta,$$

where η is a random Gaussian variable with zero mean and dispersion $(2\chi_{qi}\Delta t)^{1/2}$ (see, for example, [38]). The change in the energy during the particle's acceleration can be obtained in a similar way:

$$E_k = E_{k-1}\left[1 - \frac{2}{3}\nu_i \Delta t\right] - \frac{dE}{dt}\Delta t + \psi_i(E_{k-1})\Delta t + \varepsilon, \tag{13}$$

where

$$\nu_i \equiv \left(\frac{1}{r^2}\frac{\partial (r^2 w_i(r))}{\partial r} \right)_{r=r_{k-1}} \tag{13a}$$

is the rate of adiabatic losses (in s^{-1}), dE/dt is the Coulomb loss rate (in erg/s), and the two last terms describe the stochastic energy gain of the ion. The quantity $\psi_i(E_{k-1})$ represents the "convection" in energy space, while ε (another Gaussian variable with zero mean and dispersion $(2\varphi_i \Delta t)^{1/2}$)) describes the energy "diffusion" in this space. The growth in the coordinate and energy (12) and (13) are written in heliocentric coordinates, for which the velocity of the shock front is $V_s(t)$.

As is known, a few successive crossings of the shock front by the particle result in a regular increase in its energy [35, 36, 40]. Therefore, we can write the following relation in the rest frame of the shock front:

$$E_k^{reg} = E_{k-1}^{reg}\left[1 + \frac{2}{3}\gamma \Delta t\right], \tag{14}$$

where $\gamma \equiv -(2u(r_{k-1})/r_{k-1} + (\partial u/\partial r)_{r=r_{k-1}}) > 0$. This formula can be obtained by rewriting the system (3), replacing the velocity $w_i(r)$ with $-u(r)$ from (4) (which corresponds to a transformation to the reference frame moving with the shock front) and making the transformation from the derivatives $\partial f_{qi}/\partial t$ and $\partial f_{qi}/\partial E$ to the finite increments Δf_{qi}, Δt, and ΔE. Finally, the total increase in energy in heliocentric coordinates can be obtained by summing the energies (13) and (14), the latter of which must be transformed to the corresponding coordinate frame.

To include the charge transitions at each step k in our numerical scheme, we calculated the ionization and recombination probabilities using the formulas $P_{\text{ion}} = P_1 P_{\text{char}}/(P_1 + P_2)$ and $P_{\text{rec}} = P_2 P_{\text{char}}/(P_1 + P_2)$, where $P_1 = 1 - \exp(-\Delta t S_q)$, $P_2 = 1 - \exp(-\Delta t \alpha_q)$, and $P_{\text{char}} = 1 - \exp(-\Delta t(S_q + \alpha_q))$, and S_q and α_q are determined by (1) and (2). We can see that the sum of the ionization and recombination probabilities is equal to the total probability that the charge changes, namely, $P_{\text{ion}} + P_{\text{rec}} = P_{\text{char}}$. In turn, the probability that the charge remains constant during the time Δt is $P_{const} = 1 - P_{\text{ion}} - P_{\text{rec}}$. Therefore, the interval [0,1] can be separated into three parts, which are proportional to P_{ion}, P_{rec}, and P_{const}. If the random variable simulating a charge turns out to be in the first (or second) interval, then the charge increases (or decreases) by 1; if this variable is in the third interval, this corresponds to no change in the charge, in accordance with the probabilistic character of the reactions.

Next, let us discuss the method used to count the particles leaving the acceleration region. We will use the following two methods here.

Method I. The ions leave region 2 if they are sufficiently far from the shock front (more precisely, this distance was chosen to be $L_b \sim 10^9$ cm) and are located in a magnetic trap behind the front [19, 26]. In this case, we shall assume that the ion charge and energy no longer change. Later, these traps can be opened in interplanetary space, resulting in the release of the particles and the possibility of detecting them using various devices. This method of counting the particles is equivalent to a simple "leaky-box" model with the characteristic escape time $T_{qi} \sim L_b^2/\chi_{qi}$.

Method II. The energy and charge distributions of the ions are detected as soon as the shock reaches a distance of a few solar radii (in our calculations, $4R_\odot$). The distributions are derived by averaging over some volume occupied by the particles near the shock front. This method of counting the particles will obviously result in higher charge states of the ions (compared to the first method), since they are located in regions of dense plasma for a longer time.

Calculations using both methods will be presented below.

4. SPATIAL IRREGULARITY OF THE ACCELERATION REGION AND NONISOTHERMAL INJECTION OF THE PARTICLES

Let us use the numerical scheme described in the previous section to study the influence of various parameters (first and foremost, the number density and temperature) on the energy and charge spectra of the accelerated ions. In our earlier studies [10, 11, 13–15], the only criterion used to take into account charge variations during the acceleration process was the product of the characteristic time for the particles to gain energy T_a and the ionization and recombination rates S_q and α_q, which are proportional to N. Therefore, the parameter T_aN completely determined the dependence of the mean charges of various elements on their energy, where T_a should be interpreted as the time for the particles to gain energy, independent of the mechanism for this energy gain. In our case, the characteristic times for the regular (T_r) and stochastic (T_s) acceleration can be estimated using the formulas [20]

$$T_r = \frac{3}{u_1 - u_2}\left(\frac{\chi_{q1}}{u_1} + \frac{\chi_{q2}}{u_2}\right), \qquad (15)$$

$$T_s = p^2\left(\frac{1}{D_{q1}} + \frac{1}{D_{q2}}\right).$$

If both these processes are taken into account, the total acceleration time should be written

$$T_a = \frac{T_r T_s}{T_r + T_s}. \qquad (16)$$

Therefore, the value of T_aN enables us to conclude whether the particles' charges change during the acceleration. At first sight, the greater this quantity, the sharper the increase in the mean charge of a heavy element with its energy, as shown in the previous modeling. Note that all these results were obtained using stationary models, in which the particles could be ionized only during the acceleration [10, 11] (see also [13]). On the other hand, if, along with the acceleration time T_a, there is another parameter in the problem—the time for trapping in a region of high density—then our initial criterion must be refined. Let us consider two cases.

(1) Let the characteristic time to accelerate an ion to the energy E at a specified r be greater than or comparable to the characteristic time for variations in the ion's charge (for the same E and r):

$$T_a \geq 1/S_q, \quad 1/\alpha_q, \qquad (17a)$$

so that the accelerated ion can lose or gain one or several electrons during the time interval T_a. Since the coefficients S_q and α_q are directly proportional to N (which varies as the shock propagates), condition (17a) is satisfied only if there is a certain relation between the time for trapping the particles near the shock ($T_{\rm trap}$) and the time for acceleration of the ions:

$$T_{\rm trap} \geq T_a. \qquad (17b)$$

In particular, if $T_{\rm trap} \approx T_a$, then our initial criterion is applicable: the greater T_aN, the sharper the increase of the mean charge with energy. If the times $T_{\rm trap}$ and T_a are not approximately equal, the increase in the curves $\bar{q}_{\rm Fe}(E)$ with the largest value of $T_{\rm trap}$ will be

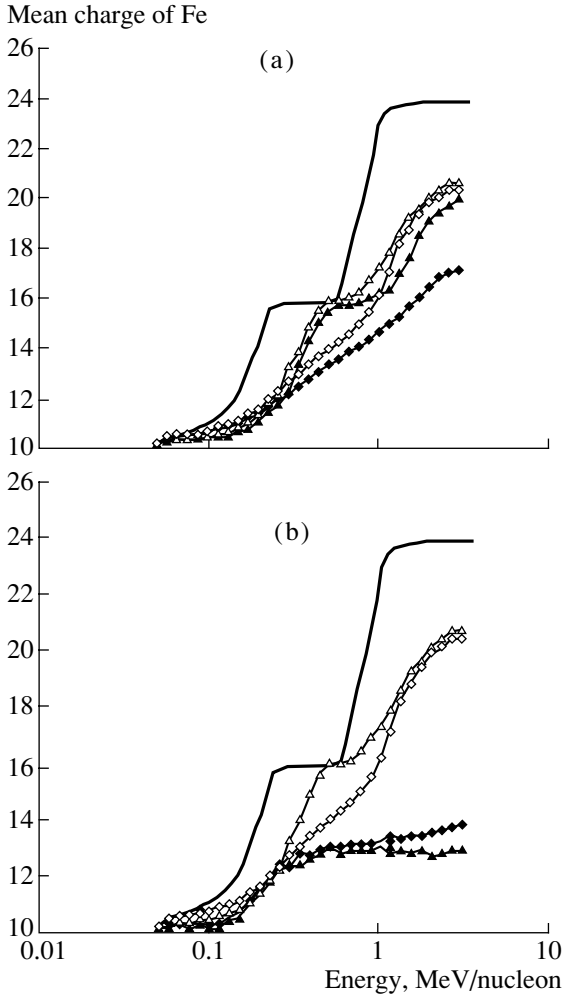

Fig. 1. Mean charges of iron ions accelerated by a moving shock front in the solar corona with $T = 10^6$ K, $S = 1.5$, $\sigma = 3$, $\delta = 5$ km, and $V_a = 3$ km/s. The triangles correspond to $\chi_{01} = 5 \times 10^{15}$ cm^2/s, and the diamonds to $\chi_{01} = 10^{15}$ cm^2/s. The solid curve describes the equilibrium charge of Fe at the specified temperature. Panel (a) presents the results obtained using method II to count the particles. The filled and hollow symbols correspond to $V_{so} = 3000$ km/s and $V_{so} = 2000$ km/s, respectively. Panel (b) presents the results obtained for $V_{so} = 2000$ km/s, using method I (filled) and method II (hollow) to count the particles.

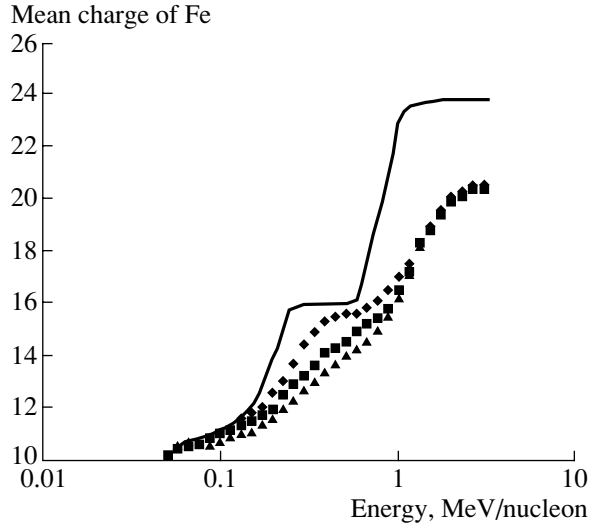

Fig. 2. Same as Fig. 1 for the case when there is a considerable contribution from stochastic acceleration. For all the curves, $T = 10^6$ K, $S = 1.5$, $\sigma = 3$, $\delta = 5$ km, $\chi_{01} = 10^{15}$ cm^2/s, $V_{so} = 2000$ km/s, and method II was used to count the particles. The diamonds correspond to $V_a = 88$ km/s, the squares to $V_a = 44$ km/s, and the triangles to $V_a = 18$ km/s.

sharper (i.e., the particles continue to be ionized after the rapid acceleration).

(2) Let the characteristic time to accelerate an ion to some energy be considerably less than the characteristic time for the ion's charge to vary at that same energy:

$$T_a \ll 1/S_q \text{ and } 1/\alpha_q. \qquad (18a)$$

In the stationary model discussed above, this condition implies that charge transitions can be ignored. However, if

$$T_{\rm trap} \geq 1/S_q \text{ and } 1/\alpha_q, \qquad (18b)$$

the charge transitions can substantially change the form of the initial distribution. In the limiting case $T_a \ll 1/S_q$, $1/\alpha_q$ and $T_{\rm trap} \gg 1/S_q$, $1/\alpha_q$, we obtain the curve for the equilibrium charge at the given temperature for the ambient plasma [14, 16].

Let us now consider the acceleration of particles by a shock propagating in the solar corona. In this case, the density of the background plasma depends on the time (or the position of the shock front). In other words, the values of S_q and α_q are appreciably affected by the velocity of propagation of the shock. We shall use for $V_s(t)$ the model dependence [24]

$$V_s = V_{so}(t/t_1)^{-1.5}, \qquad (19)$$

where $V_{so} = 3000$ km/s and $t_1 = 1$ h (this time does not have a physical interpretation and is merely a parameter of the problem). The corresponding radius of the shock front will be

$$R = R_0 + 2t_1 V_{so}(1 - (t/t_1)^{-1.5}). \qquad (20)$$

As in [24], our computation begins at $R = R_0 = 1.6R_\odot$ and ends (as is noted above) at $4R_\odot$, where the plasma density is $N \approx 2 \times 10^5$ cm^{-3}, in accordance with (6). As a result, for acceleration times of the order of several tens or hundreds of seconds, charge transitions occur only in the initial stage of the shock's propagation. Since the ambient density continues to drop at later times, the charge distributions of the accelerated ions (and the times corresponding to these distributions) do not change appreciably even after the several days of propagation to the distance of the Earth's orbit.

The mean-charge curves for various spatial diffusion coefficients and shock velocities are presented in Fig. 1a. These were obtained by continuing the numerical computation until the shock reached the distance $4R_\odot$. When the shock propagates slowly, most of the particles acquired fairly high charge states, since they were located in regions with high plasma densities for considerable times. Likewise, when the shock propagated rapidly, charge transitions became inefficient at some stage of the acceleration (for example, at the energy $\sim$0.3 MeV/nucleon in the case under consideration). This means that the particles reached heliocentric distances where $T_{\rm trap}$ and T_a became much less than $1/S_q$ and $1/\alpha_q$. The charge states remain "frozen" during the further propagation of the shock and the ejection of the particles into interplanetary space (corresponding to the plateau in the $\bar{q}_{\rm Fe}(E)$ dependence), as in the formation of charge in solar-wind ions. Identifying this plateau in real experiments when studying an isolated solar event could provide evidence about the mechanism for the particles' ejection into interplanetary space.

In addition, when deriving the dependences $\bar{q}_{\rm Fe}(E)$, it is important to discriminate between methods I and II for counting the particles. The charges will change for a much longer time in the second case, resulting in a sharper increase in $\bar{q}_{\rm Fe}(E)$. Several curves corresponding to methods I and II for various acceleration times are shown in Fig. 1b. It is difficult to determine which scenario actually takes place, since the observed increase in the mean ion charge could result from either a prolonged stay in a region of low density or a short stay in a region of high density.

Only the regular acceleration of ions by a shock front (first-order Fermi acceleration) was considered in our earlier works [10, 11, 14, 15], although the plasma in region 2 is turbulent even far from the shock front. Consequently, the contribution of stochastic acceleration (second-order Fermi acceleration) should be important. Near the shock front,

this contribution is determined by the ratio $T_r/T_s \approx (V_a/u_1)^2$ [20], which is small for typical values of V_a and u_1. However, we must take into account the fact that stochastic acceleration does not occur only near the shock front, but in a considerably greater volume. Therefore, this process can affect the dependence $\bar{q}_{Fe}(E)$ even when the ratio T_r/T_s is small. The greater the Alfven velocity, the more efficient the stochastic gain in energy. This results in a sharper increase in $\bar{q}_{\rm Fe}(E)$ compared to the case of the regular acceleration alone. Indeed, the greater the total acceleration rate, the higher the ionization of the particles (for equal times spent in the region of high plasma density). For the sake of illustration, Fig. 2 shows the calculated dependences $\bar{q}_{\rm Fe}(E)$ for several values of V_a.

The solar event of November 6, 1997, is interesting in many ways and has been studied using several sets of experimental data (see, for example, [6, 7]). Along with a well-defined maximum, the charge distributions of the accelerated Fe for this flare display an appreciable tail corresponding to high charge states. No one has been successful in describing this tail assuming a single temperature for the ambient plasma and a single acceleration mechanism [11]. As was noted in Section 2, we have attempted to describe the charge spectra of the energetic Fe ions for this event as a sum of charge spectra with several values of T. To explain the main maximum (i.e., the mean charge), we chose several temperatures near 10^6 K. We had to consider higher temperatures, up to 10^7 K, to describe the high-charge tail. On the other hand, temperatures beginning from 5×10^5 K were sufficient to describe the region $q < \bar{q}_{\rm Fe}(E)$. We selected a discrete set of injection temperatures T_j based on the following physical reasons. First, these temperatures should describe the observed dispersion of the charge distributions of the accelerated particles. Second, the intervals between the temperatures T should lead to a more or less uniform charge distribution for this event. The results of our calculations are presented in Fig. 3, where four successive charge spectra are described by the plasma temperatures $T_1 = 10^6$ K, $T_2 = 2 \times 10^6$ K, $T_3 = 5 \times 10^6$ K, and $T_4 = 10^7$ K, and the weights of the corresponding charge distributions W_i are given in the figure caption.

Finally, we note that taking into account adiabatic losses and the finite thickness of the shock does not lead to appreciable changes in $\bar{q}_{\rm Fe}(E)$ (within the accuracy of our numerical method). The reason is that the adiabatic-loss rate ν_i turns out to be considerably less than the rate of the gain in energy T_a^{-1} for distances less than $4R_\odot$ and particle energies $\sim$1 MeV/nucleon. For example, the value of ν_i calculated using formulas (5)–(7) and (13a) is 1.5×10^{-5} s^{-1} for $r = 1.6R_\odot$ and $\nu_i = 1.4 \times 10^{-4}$ s^{-1} for $r = 4R_\odot$. According to the experimental data [42], this time is even greater, about 210 ± 10 h. These estimates accordingly indicate that adiabatic losses are negligible in our model. At the same time, they can considerably affect the energy spectra of the particles in interplanetary space [19, 24]. However, this should not change the charge distributions, since the plasma density decreases considerably with increasing heliocentric distance, so that charge transitions will be almost absent. Therefore, the ion charge distributions detected near the Earth should not differ appreciably from the charge spectra near the Sun.

To estimate the effect of the broadening of the shock front on $\bar{q}_{\rm Fe}(E)$, we varied δ near the value $\delta_0 = c/\omega_{Bp}$ (for example, $\delta_0 \sim 30$ km corresponds to a magnetic field of $B = 1$ G). The resulting scatter of values $\delta = 0.5$–60 km (with other parameters fixed) yielded mean-charge curves that differed by no more than 5%, which is considerably less than the errors in the available measurements. Further, the Coulomb losses of the particles are also negligible due to the low plasma density ($N \approx 2 \times 10^7$ cm^{-3} for $r \sim 1.6R_\odot$) [9, 43, 44]. Such losses can easily be taken into consideration in Monte Carlo simulations simply by decreasing the increment (13) for each time step. If this is done, the total Fe energy spectrum becomes steeper by 5% or less, while $\bar{q}_{\rm Fe}(E)$ varies by no more than 1%.

5. THE EFFECT OF PHOTOIONIZATION

Let us now consider the influence of photoionization on the formation of the charge distributions and their moments. This is an important problem, because it remains unknown if photoionization is important when considering the acceleration of heavy ions in the solar corona. For example, Mullan and Waldron [45] suggested in 1986 that X-ray bremsstrahlung from a solar flare could appreciably ionize energetic ions. However, this process was neglected in other works of that same period [17, 46], as well as in later papers [10–16].

More exact approximation formulas for the photoionization cross sections than those used in [45] are now available. These formulas describe nearly all elements that are significant from the experimental point of view, together with their ions. We shall use the results of [47], where the corresponding cross sections are presented in the convenient form

$$\sigma_{nl}^{ph}(\nu) = \sigma_0 F(h\nu/E_0)\ \text{Mb}, \qquad (21)$$

where

$$F(y) = \left[(y-1)^2 + y_w^2\right] y^{-Q} \left(1 + \sqrt{y/y_a}\right)^{-P},$$

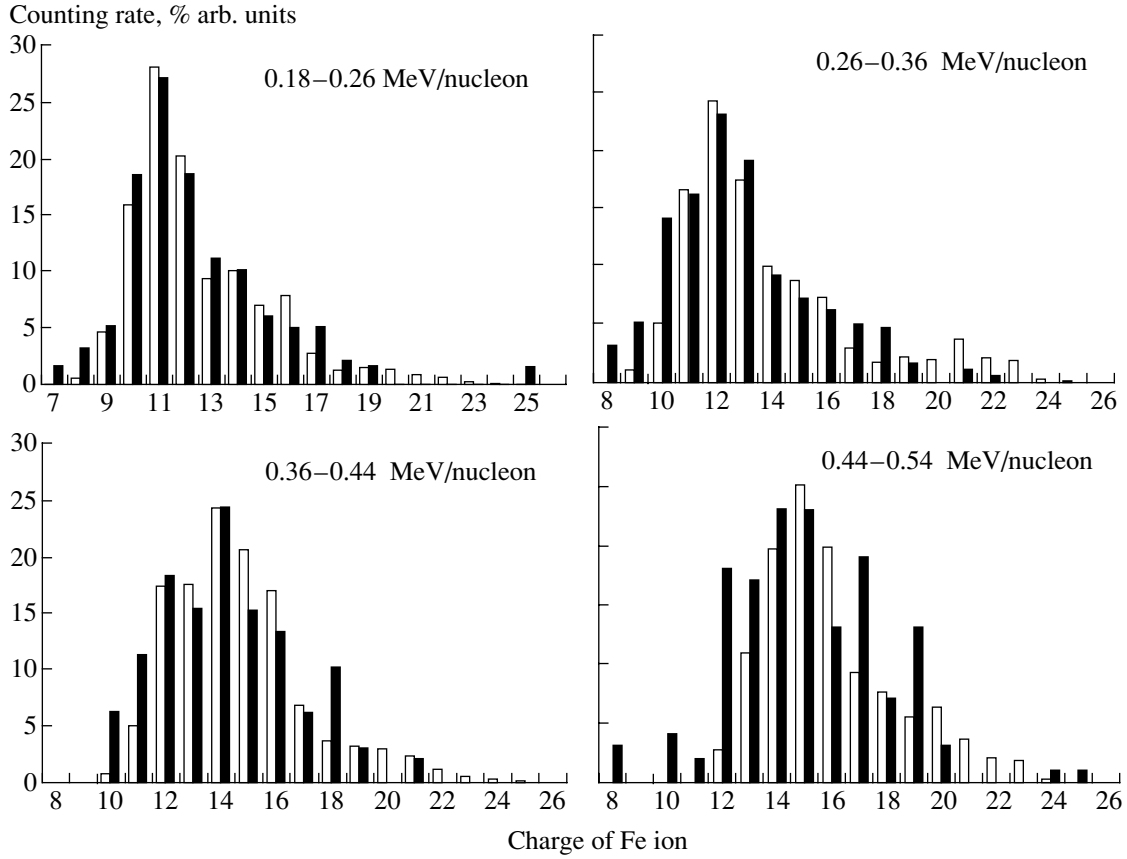

Fig. 3. Charge distributions of Fe for the event of November 6, 1997. The black columns represent the observational results [7] and the white columns the calculations for $S = 1.5$, $\sigma = 3$, $\delta = 5$ km, $\chi_{01} = 5 \times 10^{15}$ cm^2/s, and $V_{so} = 2000$ km/s. The contribution from the spectrum computed for $T_1 = 10^6$ K was taken with the weight $W_1 = 0.66$–0.75, for $T_2 = 2 \times 10^6$ K with $W_2 = 0.14$–0.26, for $T_3 = 5 \times 10^6$ K with $W_3 = 0.04$–0.09, and for $T_4 = 10^7$ K with $W_4 = 0.03$–0.09 (the values of W vary slightly from one energy interval to another).

$$y = h\nu/E_0. \tag{22}$$

Here, n and l are the main and orbital quantum numbers, respectively; σ_0, E_0, Q, y_a, y_w, and P are parameters of the fit; and $Q = 5.5 + l - 0.5P$.

For data on X-ray fluxes, we used monitoring observations obtained by the GOES-6 and GOES-7 satellites, which are published regularly in *Solar Geophysical Data* (for example, on the site `http://ftp.ngdc.noaa.gov/STP/GOES/`). These data show that the typical X-ray flux from a gradual solar event is $J_\oplus \sim 0.1$ erg cm^{-2} s^{-1} (for events of class X1 with photon energies $h\nu = 1.5$–12 keV). Next, if the characteristic spatial size of such events is taken to be $L_G \sim 10^{10}$ cm, a simple recalculation yields the X-ray flux from the active region $J \sim 2.3 \times 10^5$ erg cm^{-2} s^{-1}. We shall use two dependences for the differential distribution J_ν in the energy interval $h\nu_0 < h < h\nu_{\max}$: the power-law dependence $J_\nu \propto (\nu/\nu_0)^{-\gamma+1}$, where γ varies from three to seven, and the dependence $J_\nu \propto e^{-E/T}/E^{1.4}$, where E $= h\nu$ is the photon energy and T is the temperature of the region [48]. The photoionization rate can then be written as

$$S^{\rm ph} = \sum_{nl} \int\limits_{\nu_{\rm th}}^{\infty} \frac{\mathrm{J}_\nu}{h\nu} \sigma_{nl}^{\rm ph}(\nu) d\nu, \tag{23}$$

where the summation is carried out over all subshells nl characterized by the threshold energy $h\nu_{\rm th}$. For example, in the case of a power-law spectrum with index $\gamma = 3$ for the Fe^{+8} ion, we obtain $S^{\rm ph} \approx 2 \times 10^{-3}$ s^{-1}, while this quantity proves to be two orders of magnitude less for Fe^{+15}, $S^{\rm ph} \approx 3 \times 10^{-5}$ s^{-1}. For comparison, the total collisional ionization rates (due to interactions with electrons and protons) for these same ions (Fe^{+8} and Fe^{+15}) with an injection energy of $E_{inj} = 50$ keV/nucleon and a plasma density of $N \sim 10^8$ cm^{-3} are 3×10^{-2} s^{-1} and 1.4×10^{-3} s^{-1}, respectively. The values of $J_\oplus$ and L_G obviously vary from flare to flare. In particular, flares of classes X1–X10 with the most powerful soft X-ray fluxes

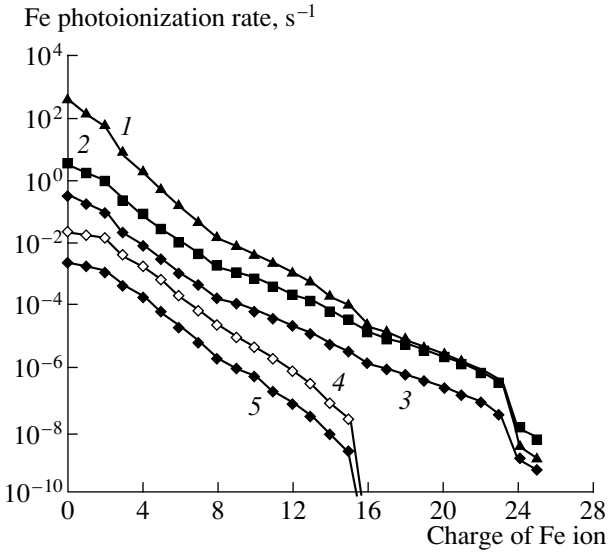

Fig. 4. Fe photoionization rates. The power-law index for the spectrum and the flux near the Earth for curves *1*–*3* were: (*1*) $\gamma = 4$ and $J_\oplus = 10^{-1}$ erg cm^{-2} s^{-1}, (*2*) $\gamma = 3$ and $J_\oplus = 10^{-1}$ erg cm^{-2} s^{-1}, and (*3*) $\gamma = 3$ and $J_\oplus = 10^{-2}$ erg cm^{-2} s^{-1}. The spectra for curves *4* and *5* were taken to be exponential, with the temperature of the active region being $T = 10^6$ K and the fluxes being $J_\oplus = 10^{-1}$ erg cm^{-2} s^{-1} and $J_\oplus = 10^{-2}$ erg cm^{-2} s^{-1}, respectively.

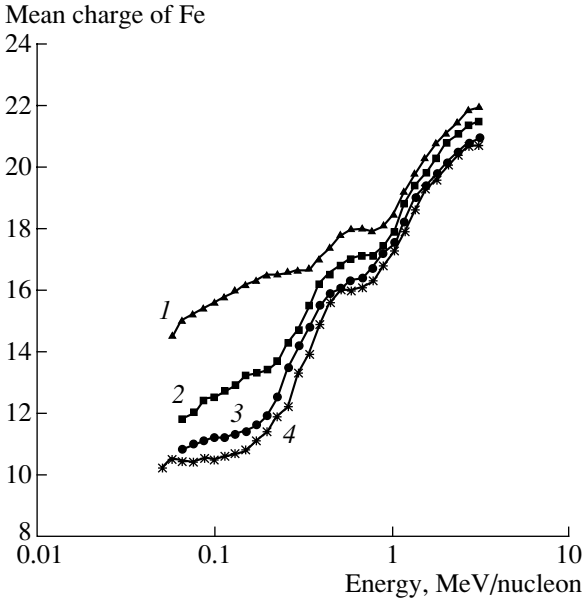

Fig. 5. Mean charges of iron ions accelerated by a shock front propagating in the solar corona, calculated taking into account photoionization. For all the curves, $T = 10^6$ K, $S = 1.5$, $\sigma = 3$, $\delta = 5$ km, $V_a = 5$ km/s, $\chi_{01} = 5 \times 10^{15}$ cm^2/s, $V_{so} = 2000$ km/s, $L_G = 10^{10}$ cm, $\gamma = 3$, and method II was used to count the particles. In addition, $J_\oplus = 1$ erg cm^{-2} s^{-1} for curve *1*, $J_\oplus = 10^{-1}$ erg cm^{-2} s^{-1} for curve *2*, $J_\oplus = 10^{-2}$ erg cm^{-2} s^{-1} for curve *3*, and $J_\oplus = 0$ erg cm^{-2} s^{-1} for curve *4*.

(10^{-1} erg cm^{-2} s^{-1} $< J_\oplus <$ 1 erg cm^{-2} s^{-1}) are observed quite rarely. For example, fluxes of $J_\oplus > 5 \times 10^{-1}$ erg cm^{-2} s^{-1} (events of class X5 and above) were detected only nine times during 1996 to 2001 (the powerful event of November 6, 1997, being among them), with five of these events occurring in 2001.

The ionization rates $S^{\rm ph}$ calculated for the exponential and power-law spectra J_ν (see above) and various fluxes in the flare region are presented in Fig. 4. Using these dependences, we can calculate a set of curves $\bar{q}_{\rm Fe}(E)$ including the effects of photoionization. We can see in Fig. 5 that, apart from the most powerful X-ray events of classes X1–X10, the contribution of photoionization can usually be neglected.

It is likely that photoionization is likewise not important for compact impulsive events, whose characteristic spatial scales are 10^8 cm or less. Their observed X-ray fluxes are weaker, and they are usually events of class M with fluxes 10^{-2} erg cm^{-2} s^{-1} $< J_\oplus < 10^{-1}$ erg cm^{-2} s^{-1}. As a result, the photoionization rates should be a factor of 10^3–10^4 greater. However, the collisional ionization rates will also increase in the denser plasma of such flares. Therefore, the relative contribution of photoionization should remain small. Note that the above estimates were based on the assumption that photoionization can occur during the entire particle-acceleration process, with the X-ray flux maintaining its maximum level. However, if the acceleration and escape of heavy particles are more rapid than the heating of the background plasma (in particular, the heating of its electrons, which give rise to the subsequent bremsstrahlung), photoionization will not affect the charge states of energetic ions at all.

6. CONCLUSIONS

The aim here was to further develop charge-consistent models for heavy-ion acceleration (we have considered iron in solar cosmic rays as an example). The main differences from preceding models were taking into account the spherical geometry of the shock front and the nonuniform temperature of the injected plasma, as well as the contribution of photoionization and large-scale density irregularities associated with the propagation of the shock front in the solar corona. In addition, we showed that the broadening of the shock front and adiabatic losses in the expanding solar-wind flow do not appreciably affect the shape of the charge spectra or, consequently, the dependences $\bar{q}_{\rm Fe}(E)$. Unfortunately, the available

observational data are not sufficiently accurate to demonstrate the advantages of models with irregular plasma densities for explaining the real data. However, there is no doubt that such models should be used when considering prolonged acceleration and particle-trapping times.

Let us briefly summarize our main results.

The energy behavior of the mean charges of Fe ions accelerated in the solar corona depends on the ratios of the speed of the shock front, the acceleration rate, and the rates of atomic processes.

We were able to model the charge distributions of the Fe ions produced by the solar event of November 6, 1997, characterized by very wide charge distributions, using a model with a nonisothermal injection of particles from the acceleration region.

Our numerical computations showed that the contribution of photoionization to the $\bar{q}_{\mathrm{Fe}}(E)$ dependence can be neglected for most gradual and impulsive solar events (except for the most powerful class X10 flares).

We have also studied the sensitivity of the results given by the charge-consistent models to the specified means by which particles escape from the acceleration region.

ACKNOWLEDGMENTS

This work was supported by the Russian Foundation for Basic Research (project nos. 00-02-17031 and 02-02-06922) (MAS).

REFERENCES

1. A. M. Luhn, B. Klecker, D. Hovestadt, *et al.*, Adv. Space Res. **4**, 161 (1984).
2. A. M. Luhn, D. Hovestadt, B. Klecker, *et al.*, *Proceedings of 19th International Cosmic Ray Conference* (NASA Goddard Space Flight Center, 1985), Vol. 4, p. 241.
3. G. M. Mason, J. E. Mazur, M. D. Looper, and R. A. Mewaldt, Astrophys. J. **452**, 901 (1995).
4. A. J. Tylka, P. R. Boberg, J. H. Adams, *et al.*, Astrophys. J. **444**, L109 (1995).
5. M. Oetliker, B. Klecker, D. Hovestadt, *et al.*, Astrophys. J. **477**, 495 (1997).
6. J. E. Mazur, G. M. Mason, M. D. Looper, *et al.*, Geophys. Res. Lett. **26**, 173 (1999).
7. E. Möbius, M. Popecki, B. Klecker, *et al.*, Geophys. Res. Lett. **26**, 145 (1999).
8. I. G. Kurganov and V. M. Ostryakov, Pis'ma Astron. Zh. **17**, 177 (1991) [Sov. Astron. Lett. **17**, 77 (1991)].
9. Yu. Yu. Kartavykh, V. M. Ostryakov, I. Yu. Stepanov, and M. Yoshimori, Kosm. Issled. **36**, 465 (1998).
10. V. M. Ostryakov and M. F. Stovpyuk, Pis'ma Astron. Zh. **25**, 935 (1999) [Astron. Lett. **25**, 819 (1999)].
11. V. M. Ostryakov and M. F. Stovpyuk, Sol. Phys. **189**, 357 (1999).
12. A. F. Barghouty and R. A. Mewaldt, Astrophys. J. **520**, L127 (1999).
13. V. M. Ostryakov, Yu. Yu. Kartavykh, D. Ruffolo, *et al.*, J. Geophys. Res. **105** (A12), 27315 (2000).
14. M. F. Stovpyuk and V. M. Ostryakov, Sol. Phys. **198**, 163 (2001).
15. M. F. Stovpyuk and V. M. Ostryakov, Adv. Space Res. **26**, 503 (2001).
16. L. Kocharov, G. A. Kovaltsov, J. Torsti, and V. M. Ostryakov, Astron. Astrophys. **357**, 716 (2000).
17. A. M. Luhn and D. Hovestadt, Astrophys. J. **317**, 852 (1987).
18. M. Arnaud and J. Raymond, Astrophys. J. **398**, 394 (1992).
19. I. N. Toptygin, *Cosmic Rays in Interplanetary Magnetic Fields* (Nauka, Moscow, 1983; Reidel, Dordrecht, 1985).
20. E. G. Berezhko, V. K. Elshin, G. F. Krymskiĭ, and S. N. Petukhov, *The Generation of Cosmic Rays by Shock Waves* [in Russian] (Nauka, Novosibirsk, 1988).
21. M. Ostrowski and R. Schlickeiser, Astron. Astrophys. **268**, 818 (1993).
22. I. N. Toptygin, Pis'ma Astron. Zh. **25**, 930 (1999) [Astron. Lett. **25**, 814 (1999)].
23. M. A. Lee and J. M. Ryan, Astrophys. J. **303**, 829 (1986).
24. E. G. Berezhko, S. N. Petukhov, and S. N. Taneev, Izv. Akad. Nauk, Ser. Fiz. **65**, 339 (2001).
25. S. A. Kaplan, Astron. Zh. **44**, 384 (1967) [Sov. Astron. **11**, 302 (1967)].
26. S. T. Wu, Space Sci. Rev. **32**, 115 (1982).
27. A. Maxwell and M. Dryer, Space Sci. Rev. **32**, 11 (1982).
28. E. C. Sittler and M. Guhathakurta, Astrophys. J. **523**, 812 (1999).
29. K. Hasselmann and G. Wibberenz, Z. Geophys. **34**, 353 (1968).
30. A. A. Korchak, Sol. Phys. **66**, 149 (1980).
31. S. Pinter, Space Sci. Rev. **32**, 145 (1982).
32. G. E. Kocharov, V. P. Lazutkov, G. A. Matveev, *et al.*, Astron. Zh. **76**, 547 (1999) [Astron. Rep. **43**, 475 (1999)].
33. A. J. Tylka, J. Geophys. Res. **106** (A11), 25333 (2001).
34. Yu. Yu. Kartavykh, V. M. Ostryakov, D. Ruffolo, *et al.*, in *Proc. 27th International Cosmic Ray Conference* (Hamburg, 2001), Vol. 8, p. 3091.
35. A. Achterberg and W. M. Krulls, Astron. Astrophys. **265**, L13 (1992).
36. J. G. Kirk and P. Schneider, Astrophys. J. **322**, 256 (1987).
37. C. W. Gardiner, *Handbook of Stochastic Methods for Physics, Chemistry, and the Natural Sciences* (Springer-Verlag, Berlin, 1985; Mir, Moscow, 1986).
38. H. Gould and J. Tobochnik, *An Introduction to Computer Simulation Methods. Application to Physical Systems* (Addison-Wesley, USA Reading, 1988; Mir, Moscow, 1990).
39. M. G. Baring, D. C. Ellison, and F. C. Jones, Astrophys. J., Suppl. Ser. **90**, 547 (1994).

40. D. C. Ellison and D. Eichler, Astrophys. J. **286**, 691 (1984).
41. F. C. Jones and D. C. Ellison, Astrophys. Space Sci. **58**, 259 (1991).
42. S. S. Murray, E. S. Stone, and R. E. Vogt, Phys. Rev. Lett. **26**, 663 (1971).
43. M. F. Stovpyuk and V. M. Ostryakov, Astron. Zh. **77**, 944 (2000) [Astron. Rep. **44**, 833 (2000)].
44. L. Kocharov, G. A. Kovaltsov, and J. Torsti, Astrophys. J. **556**, 919 (2001).
45. D. J. Mullan and W. L. Waldron, Astrophys. J. **308**, L21 (1986).
46. A. A. Kharchenko and V. M. Ostryakov, in *Proc. 20th International Cosmic Ray Conference* (Moscow, 1987), Vol. 3, p. 248.
47. D. A. Verner and D. G. Yakovlev, Astron. Astrophys., Suppl. Ser. **109**, 125 (1995).
48. C. J. Crannell, K. J. Frost, C. Mätzler, *et al.*, Astrophys. J. **223**, 620 (1978).

Translated by Yu. Dumin